Chem Soc Rev

REVIEW ARTICLE

View Article Online
View Journal | View Issue

Cite this: *Chem. Soc. Rev.*, 2021, **50**, 2388

Carbon materials for ion-intercalation involved rechargeable battery technologies

Gang Wang, Minghao Yu * and Xinliang Feng *

The ever-increasing energy demand motivates the pursuit of inexpensive, safe, scalable, and high-performance rechargeable batteries. Carbon materials have been intensively investigated as electrode materials for various batteries on account of their resource abundance, low cost, nontoxicity, and diverse electrochemistry. Taking use of the reversible donor-type cation intercalation/de-intercalation (including Li^+, Na^+, and K^+) at low redox potentials, carbon materials can serve as ideal anodes for 'Rocking-Chair' alkali metal-ion batteries. Meanwhile, acceptor-type intercalation of anions into graphitic carbon materials has also been revealed to be a facile, reversible process at high redox potentials. Based on anion-intercalation graphitic carbon materials, a number of dual-ion battery and Al-ion battery technologies are experiencing booming development. In this review, we summarize the significant advances of carbon materials in terms of the porous structure, chemical composition, and interlayer spacing control. Fundamental mechanisms of carbon materials as the cation host and anion host are further revisited by elaborating the electrochemistry, intercalant effect, and intercalation form. Subsequently, the recent progress in the development of novel carbon nanostructures and carbon-derived energy storage devices is presented with particular emphasis on correlating the structures with electrochemical properties as well as assessing the device configuration, electrochemical reaction, and performance metric. Finally, perspectives on the remaining challenges are provided, which will accelerate the development of new carbon material concepts and carbon-derived battery technologies towards commercial implementation.

Received 2nd March 2020

DOI: 10.1039/d0cs00187b

rsc.li/chem-soc-rev

Department of Chemistry and Food Chemistry & Center for Advancing Electronics Dresden (cfaed), Technische Universität Dresden, 01062 Dresden, Germany.
E-mail: minghao.yu@tu-dresden.de, xinliang.feng@tu-dresden.de

Gang Wang

Gang Wang received his PhD degree in Physical Chemistry from the University of Chinese Academy of Sciences and Institute of Coal Chemistry, CAS in 2016. Then as a postdoctoral researcher, he joined Prof. Klaus Müllen's group at Max Planck Institute for Polymer Research and Prof. Xinliang Feng's group at Technische Universität Dresden. Currently, he mainly focuses on electrochemical energy storage research in novel carbon materials, carbon hybrids and carbon-rich frameworks, and constructing high-efficiency energy storage devices (Li/Na-ion batteries, anion batteries) with particular function/property.

Minghao Yu

Minghao Yu received his PhD degree in Material Physics and Chemistry from Sun Yat-sen University in June 2017. In November 2017, he joined Prof. Xinliang Feng's group as a postdoctoral research associate at Technische Universität Dresden (TU Dresden) with the support of Humboldt Research Fellowship. In March 2019, he became a research group leader of the Chair for Molecular Functional Materials at TU Dresden. His research interests focus on the development of advanced functional materials for applications of energy storage (supercapacitors and metal-ion batteries) and conversion (electrocatalysis and metal–air batteries).

1. Introduction

Under the global scenario of depletion of non-renewable fossil fuels and growing environmental concerns, the electricity market is now undergoing a unique transformation by the rise of power generation from variable renewable sources, such as wind, solar, and tide.[1–3] This transformation puts electricity at the forefront of the clean-energy exploitation, helping to cut air pollution and CO_2 emission. It also imposes a strong requirement of reliable energy storage technologies to smooth out the intermittency of renewable energy production.[4–6] Among various energy storage technologies, rechargeable battery energy storage provides an intelligent way to manage power supply by storing electricity in the form of chemical energy with high efficiency.[7–9] Li-ion batteries (LIBs), which represent the fast-growing rechargeable battery technology, store charge by employing Li^+ as the charge carrier.[10] Li^+ moves from the anode to the cathode through the electrolyte when LIBs are charged, while Li^+ moves in the opposite direction when LIBs are discharged. In the past few decades, LIBs have attained great success in powering portable electronic devices, electric vehicles, and smart grids.[11] Excitingly, the 2019 Nobel Prize in Chemistry was awarded to John B Goodenough, M. Stanley Whittingham and Akira Yoshino, who dramatically contributed to the development of this revolutionary energy technology. Nevertheless, the widespread implementation of LIBs is still of great concern, which is severely hindered by their unsatisfactory durability (less than 1000 cycles), high cost ($900–1300 per kW h), and insufficient safety.[12,13] With the hope of solving the intrinsic bottlenecks of LIBs, extensive efforts have been devoted to developing new battery chemistries relying on different charge carrier ions (such as Na^+, K^+, Mg^{2+}, Zn^{2+}, Al^{3+} and anions), also known as post-LIBs.[9,14] A significant portion of post-LIBs makes use of inherently safe, low-cost, and naturally abundant raw materials. For a broad market penetration, further improvement in electrochemical performance (including energy density, power density, and cycling stability) and cost is essential for advanced battery technologies.

Xinliang Feng

Xinliang Feng has been full professor and the head of the Chair of Molecular Functional Materials at Technische Universität Dresden since 2014. His current scientific interests include organic synthesis, supramolecular chemistry of π-conjugated systems, bottom-up synthesis and top-down fabrication of graphene and graphene nanoribbons, 2D polymers and supramolecular polymers, as well as 2D carbon-rich conjugated polymers for (opto)electronic applications and materials for energy storage and conversion.

Carbon is one of the most abundant elements in nature, which is the basis of the whole organic chemistry.[15,16] In this regard, carbon materials can be easily and cheaply produced by straightforward conversion reactions. Taking advantage of the favorable features like superb chemical stability, good conductivity, large specific surface area, and unique porosity, carbon materials have a long history of use as electrodes in a wide spectrum of battery technologies.[17] In 1991, Sony Corporation, for the first time, technically realized the prototype LIBs, in which graphite was used as the Li^+-intercalation anode. Extensive explorations have been conducted to provide a profound understanding and optimization of graphite intercalation compounds. To date, graphite is still in use as a commercial anode for LIBs. Meanwhile, numerous carbon nanomaterials were discovered in the past three decades, including one-dimensional (1D) carbon nanotubes (CNTs) and two-dimensional (2D) graphene.[17] These new types of carbon allotropes possess significant differences not only in morphology and dimensionality, but also in local electronic structures. Thus, the Li^+-storage ability of these carbon nanomaterials has also attracted extensive research interest. Recent studies have also uncovered a substantially enhanced Li-storage capacity for disordered carbon materials with partially graphitic domains. These partially graphitic carbon materials are featured by a large fraction of highly disordered graphene domains, as well as a pronounced mixture of sp^2–sp^3 carbon. To boost the Li^+ storage kinetics, more and more efforts have been devoted to constructing porous carbon materials with adjustable pore size and large specific surface area, which enables a facile electrolyte infiltration and a large electrode/electrolyte interface. On the other hand, with the lessons learned from Li^+ intercalation of carbon materials, the rapid emergence of post-LIBs has motivated the exploration of carbon materials as host anodes for post-LIBs under cation-intercalation chemistries (*e.g.* Na^+ and K^+). However, due to the distinct physical and chemical features of charge carriers and the electrolyte, the Na^+ and K^+ intercalation behavior of carbon materials has been demonstrated to be substantially different from the Li^+ intercalation process. Compared to other high-capacity anode materials working under alloy reaction (Si, P, and Al)[18–22] or conversion reaction (MeO_x, MeS_x, and $MeSe_x$)[23–26] mechanisms, cation-intercalation carbon materials are inferior in specific capacity. However, the low working potential and minimized structural variation of carbon anodes during cation storage endow batteries with high working voltage and long cycling life.

Apart from cation-intercalation chemistry, the anion-intercalation chemistry of graphite in a concentrated acid electrolyte was first reported by Rüdorff and Hofmann in 1938.[27] Shortly after, systematic research has been carried out to explore the various anion-intercalation chemistries (including BF_4^-, PF_6^-, ClO_4^-, AsF_6^-, SbF_6^-, $AlCl_4^-$, bis(trifluoromethanesulfonyl)imide ($TFSI^-$)) of carbon materials in nonaqueous electrolytes.[28,29] The unique anion-intercalation chemistry of carbon materials with high intercalation potential opens up new application opportunities for carbon materials as favorable cathodes for dual-ion batteries (DIBs) and aluminum-ion batteries (AIBs). As the name implies, DIBs rely on both anions and cations in electrolytes to store charge. Anions and cations are incorporated into anodes and

cathodes respectively during charging, whereas anions and cations are released from the electrodes into the electrolyte when DIBs are discharged. In 1989, McCullough *et al.*[30] patented the first DIB device with a cation-intercalation carbon anode and an anion-intercalation carbon cathode. To date, a number of DIB systems have been developed, most of which comprise an anion-intercalation carbon cathode together with varying cation-intercalation anodes and different charge-carrier ions. Although different p-type organic molecules/polymers[31–35] can also be used to store anions by reversible redox reactions, the high cost and the intrinsic insulating/semiconducting nature of organic materials make it rather challenging for practical application. Moreover, the dissolution of organic compounds in aprotic electrolytes is also a long-standing concern.

Thus, carbon materials have emerged as an important category of material candidates for ion-intercalation energy storage technologies. A blooming research activity has been conducted in the last few years, aiming to rationally fabricate favorable carbon structures, fundamentally understand the origin of their unique ion-intercalation chemistry, as well as employ them to develop new battery technologies (Fig. 1). In fact, many reviews have more or less discussed the important role of carbon materials in different battery systems.[28,29,36–43] However, a comprehensive review on the advanced ion-intercalation chemistry of carbon materials and its application in different energy storage technologies is still lacking. Herein, we first revisit the structure and properties of ion-intercalative carbon materials with an emphasis on chemical and structural principles to design advanced ion-intercalative carbon materials. A pedagogical description of the underlying mechanism is then provided systematically with respect to both cation-intercalation chemistry and anion-intercalation chemistry of carbon electrodes. Afterwards, the recent progress in energy storage technologies based on ion-intercalative carbon electrodes is summarized by categorizing them into cation-based 'rocking chair' batteries and emerging anion-involved DIBs. Lastly, the remaining challenges and main

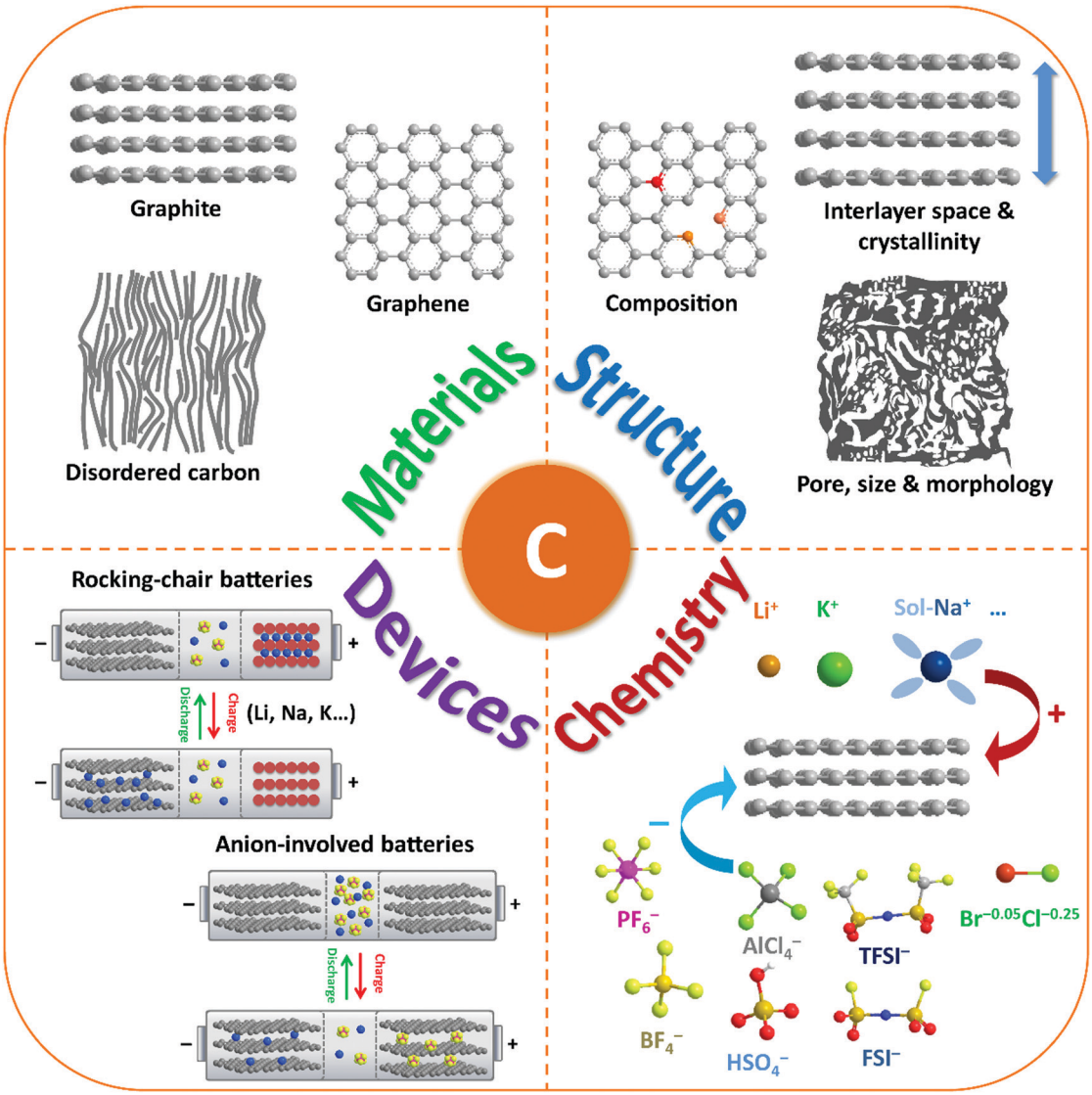

Fig. 1 Schematic illustration of the review content including carbon-based materials, structures, ion-intercalation chemistry, and battery devices.

development directions for ion-intercalation carbon structures and energy storage devices based on them are addressed.

2. Structures and properties of ion-intercalative carbon materials

2.1 Properties of ion-intercalative carbon materials

Ion-intercalative carbon materials generally come in two different forms, namely ordered carbon and disordered carbon. Owing to the different topological structures, different carbon materials exhibit apparently distinct electrochemical behavior for ion intercalation. In this section, we evaluate the structural properties and synthesis routes of different types of carbon materials.

2.1.1 Ordered carbon. Ordered carbon represents carbon materials with long-range order and high crystallinity. According to the different structures, ion-intercalative ordered carbon materials include three-dimensional (3D) graphite, 2D graphene, and 1D CNTs.

Graphite is the 'oldest', and still one of the most common anode materials for LIBs, which delivers a high theoretical capacity of 372 mA h g^{-1}. Meanwhile, it has also been revealed to be a favorable host material for K^+ and various anions. Graphite has a perfect 3D crystalline and layered structure constituted of sp^2-hybridized carbon.[44] The sp^2-hybridized carbon layer stacks along the *c*-axis with stacking order of either hexagonal AB stacking or rhombohedral ABC stacking (Fig. 2a). The delocalized π-bonds enable high in-plane electronic conductivity in graphite, which is favorable for rapidly bringing the electronic carriers to contact the intercalated ions. Meanwhile, the strong orbital overlap in the first octet makes the sp^2 carbon bonds robust in strength. Graphite is also featured by weak van der Waals bonding in the vertical direction of planes, which renders an interlayer spacing of 3.35 Å. This spacing can accommodate guest intercalated ions. Natural graphite is a native element mineral, which can be exploited in metamorphic and igneous rocks. In addition, artificial graphite can be synthesized by graphitizing non-graphitic precursors (*e.g.* petroleum, coal) in a non-oxygen environment at high temperature above 2000 °C.[45]

Graphene and its related carbon materials refer to 2D carbon materials with isolated single or few sp^2 carbon layer stacks (Fig. 2b). Graphene can be considered as one- or few-atom thick layer of graphite or an indefinitely extended aromatic molecule. Since the first isolation of graphene from graphite in 2004 by Novoselov *et al.*,[46] graphene has rapidly caught attention from the view of both academic research and industrial application due to its distinguished properties. Graphene displays ultrastrong mechanical properties with a tensile strength of 125 GPa and a Young's modulus of up to 1100 GPa.[47] The electrical conductivity and charge mobility of graphene are measured to be 1×10^8 S m^{-1} and 2×10^5 cm^2 V^{-1} s^{-1}.[48] Particularly, the high specific surface area of graphene (up to 2630 m^2 g^{-1}) is favorable for energy storage applications.[49]

The synthesis routes toward graphene can be categorized into bottom-up synthesis and top-down exfoliation from graphite. Generally, the bottom-up synthesis of graphene can be realized by epitaxial growth with structure-defined precursors or chemical vapor deposition (CVD), which allows obtaining graphene with high purity and quality.[50–52] However, these methods require expensive precursors and complex processing, significantly

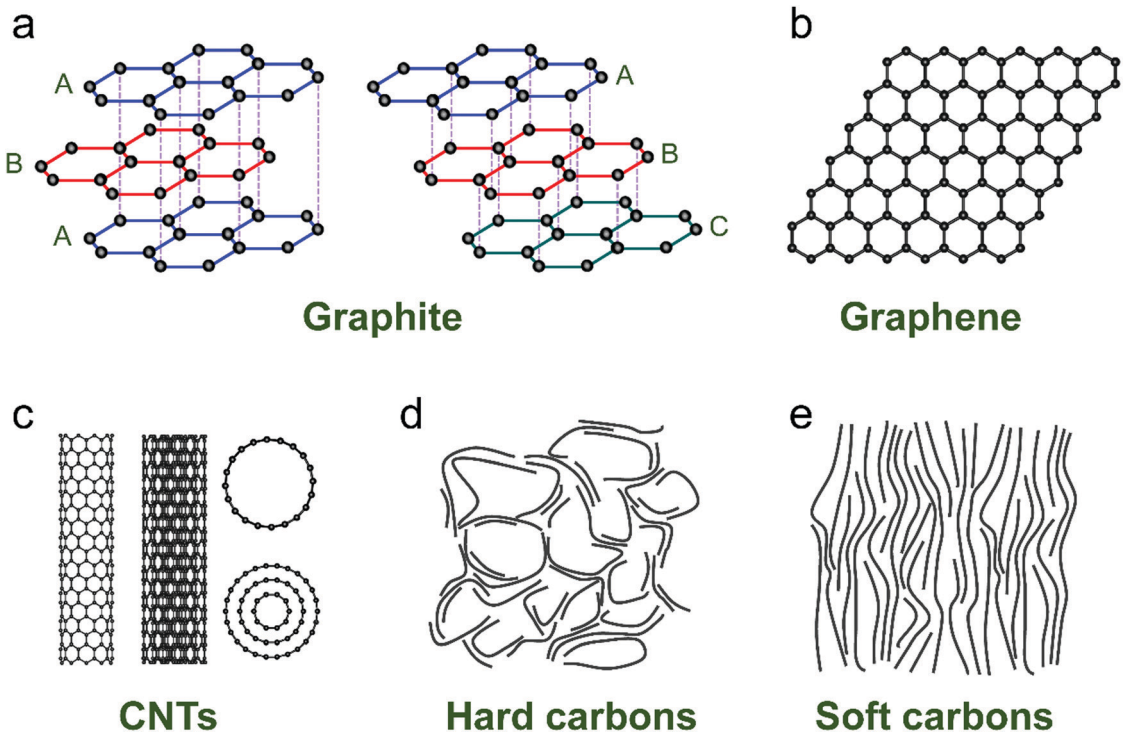

Fig. 2 Typical structures of (a) graphite, (b) graphene, (c) carbon nanotubes, (d) hard carbon, and (e) soft carbon.

hindering the low-cost and massive production of graphene. For example, in CVD methods, catalytic metal substrates (*e.g.* Ni, Cu) are exposed to hydrocarbon gases (*e.g.* CH_4, C_2H_4, CO) at a high temperature (>500 °C). Hydrocarbon gases are decomposed, diffused and deposited on metal surfaces, followed by nucleation and growth of graphene. By contrast, the top-down exfoliation strategy can produce graphene in much larger amounts under facile synthetic conditions. The most general top-down approach is modified Hummers' method, which was first proposed in 1958.[53] In such a method, graphite flakes are chemically oxidized into graphite oxide (GO) in a strong oxidation environment. The decorated oxygen-containing functional groups would expand the layer distance of graphite and weaken the bonding strength between layers. With the assistance of sonication, GO can be easily delaminated. The graphene material (generally called reduced graphene oxide (rGO)) is obtained by a further reduction step, in either a thermal, chemical, or electrochemical way.[54] While this method provides great potential for large-scale production, the produced graphene materials are generally rich in defects and functional groups. Apart from modified Hummers' method, several other liquid-phase exfoliation approaches have also been developed, which rely on external driving forces (*e.g.* ultrasonication,[55] shearing,[56] and electric field[57]). Of note is that the ion-storage properties of graphene materials vary largely along with lateral dimensions, layer number and defects. These characteristics can be well controlled by adopting different synthesis approaches.

CNTs are representative 1D carbon structures, which were discovered in 1991.[58] They can be viewed as carbon cylinders with a diameter of 1–20 nm, obtained by scrolling single or multilayered graphene.[59] CNTs have typical tubular structures with a large length-to-diameter ratio. For example, Zhang *et al.*[60] reported a kind of ultralong CNT with length up to 55 cm by employing a floating CVD method. According to the layer number of the wall (Fig. 2c), CNTs are categorized into single-walled CNTs (SWCNTs) and multi-walled CNTs (MWCNTs). Based on the different wrapping angles, SWCNTs show either metallic or semi-conducting features. Eqn (1) describes the vector (c_h) of SWCNTs, where a_1 and a_2 are unit vectors of the graphene layer, and n and m are integers. In general, SWCNTs show a metallic feature when $(n - m)$ is a multiple of 3; otherwise, SWCNTs are semiconductive.[61] Unlikely, MWCNTs are composed of coaxial tubules with a constant spacing of 0.34 nm between each two walls, and they generally behave like non-gap metals. Both metallic SWCNTs and MWCNTs present a large specific surface area (up to 1300 $m^2\ g^{-1}$), ultrahigh conductivity (up to 5000 S cm^{-1}) and charge carrier mobility (more than 100 000 $cm^2\ V^{-1}\ s^{-1}$),[62–64] which make them attractive candidates for battery applications.

$$c_h = na_1 + ma_2 \quad (1)$$

Iijima, for the first time, discovered MWCNTs during the synthesis of fullerene by arc discharge deposition.[58] Later on, Smalley *et al.*,[65] in 1995, developed a new laser ablation method to produce SWCNTs by treating the graphitic carbon with laser ablation. Afterwards, the CVD method was employed to synthesize CNTs by using gaseous carbon sources with metal catalysts at high temperatures of 500–1200 °C, which soon attracted intense attraction from the community.[66–68] Systematic research has been conducted to control the length, diameter, and wall number of CNTs by adjusting the carbon precursors, catalysts, and other CVD parameters. The synthetic details have been well documented in previous review papers.[15,69,70]

2.1.2 Disordered carbon. Different from ordered carbon, disordered carbon materials do not have long-range periodic structure in plane or along stacking direction. They are featured by randomly aligned sp^2 graphitic microdomains partially crosslinked by sp^3 hybridized carbon atoms in amorphous carbon areas. According to the graphitization possibility, disordered carbon materials are typically classified into hard carbon (Fig. 2d) and soft carbon (Fig. 2e). Hard carbon cannot be graphitized, because the strong cross linking of pyrolytic carbon would immobilize carbon layers even at a high temperature up to 3000 °C. By contrast, the cross linking between soft carbon layers is week, making the carbon layers mobile upon thermal treatment. At a temperature of 1500–3000 °C, soft carbon can be transformed into graphite. Disordered carbon shows pseudo-graphitic features with a turbostratic structure, which can be evidenced by the two broad X-ray diffraction (XRD) peaks around 25° and 43°, corresponding to the (002) and (101) planes of graphite.[71] Typically, disordered carbon is described by the degree of crystallinity, also named graphitization. Raman spectroscopy is a clear indicator to show the graphitic structure of carbon materials. Two characteristic Raman peaks around 1350 cm^{-1} (D band) and 1580 cm^{-1} (G band) are associated with defect-induced mode and in-plane stretching vibration of sp^2-hybridized carbon, respectively.[72] The intensity ratio of these two peaks (I_D/I_G) is generally used to describe the disorder degree of carbon materials.

Disordered carbon materials are generally prepared by thermal decomposition of different organic precursors in an inert atmosphere (N_2, Ar, and even vacuum) at a high temperature (less than 1500 °C). Depending on the nature of precursors and synthetic conditions, the microstructure and properties of disordered carbon materials have significant difference. Hard carbon materials are generally the pyrolysis product of biomass with insufficient aromatic structures (*e.g.* sugar, charcoal, cellulose, coconut shells, phenol-formaldehyde resins, and polyvinylidene chloride), whilst soft carbon materials are obtained from pyrolytic aromatic compounds (*e.g.* pitch, benzene, petroleum coke, polyvinyl acetate, and polyvinyl chloride). During the pyrolysis, the main mass loss of the organic precursor is typically observed in the temperature range of 250–500 °C, which is assigned to the successive release of H and heteroatoms (like O, N, S, *etc.*) as volatile products (hydrocarbons, H_2O, NO_2, CO, CO_2, SO_2, *etc.*). When the temperature exceeds 700 °C, the precursor is generally considered as carbonized; however, still a small amount of hydrogen and heteroatoms remain, which would be completely removed when the temperature reaches more than 1000 °C. In addition, the synthetic parameters, like heating rate, final temperature, pyrolysis time, and protective gas,[73–76] also play an important role in determining the structure and properties of the derived carbon materials.

2.2 Nanoporous structure construction

Recently, nanoporous carbon materials have attracted significant interest from the energy storage community, as they can provide efficient channels for ion transport, considerable available ion-storage sites, as well as remarkable buffers for alleviating the volume change during ion intercalation/deintercalation (Fig. 3a).[77,78] According to the definition of International Union of Pure and Applied Chemistry (IUPAC),[79] pores are categorized into micropores (<2 nm), mesopores (2–50 nm) and macropores (>50 nm). It is well established that mesopores and macropores can serve as the channels for mass transport; meanwhile micropores play a key role in determining the specific surface area, as well as in permitting a high access of charge-carrier ions to the carbon surface. In the last few years, tremendous research has been conducted on the methodology exploration to precisely control the pore size, shape, and dispersibility in carbon materials.

Generally, nanopores can be introduced into carbon materials through two approaches: template-assisted synthesis and post activation. In the case of template-assisted synthesis, templates are classified as hard templates and soft templates. The hard-template method includes the steps of filling the interspace of the hard template with carbon sources, carbonization, and template removal.[80,81] This method provides a ready way to tailor the porosity of carbon materials, in which the pore size and pore shape can roughly inherit the nanostructure of the utilized templates. A large number of hard templates have been investigated, including silica, anodic aluminum oxide, other inorganic oxides, soluble salts, polystyrene, molecular sieves, and bio-ceramics. Based on the different properties of hard templates, they can be removed by either physical processing (*e.g.* sublimation, dissolution) or chemical processing (*e.g.* corrosion). In contrast, soft templates refer to templates like vesicles, micelles, gas bubbles, and emulsion droplets, which originate from the additives like self-assembled polymers and surfactants.[82] Soft templates are easily removed during the carbonization of carbon sources, which avoids the additional template removal process. In comparison with the hard-template method, the soft-template method offers a more convenient and cost-effective way to produce porous carbon materials on a large scale. To construct hierarchical pores, researchers also synthesized nanoporous carbon materials, by combining multiple templates or both hard template and soft template.[83]

In addition, nanopores can be also introduced into carbon materials by a chemical activation process. Activating agents (such as NaOH, KOH, H_3PO_4) can penetrate into the inner structure of carbon.[84,85] During the carbonization, activating reagents would react with the surrounding carbon atoms, forming continuous and uniform pores. These strong corrosive agents allow a wide coverage of carbon precursors and a high yield of pores, but also suffer from high cost, safety and environmental issues. Apart from strong basic or acid activating agents, some facile agents have also been employed such as gaseous H_2O and CO_2.[86] Partial carbon in the outer shell of carbon materials would be gasified, forming pores. It should be noted that although these activating agents allow large-scale and eco-friendly activation of carbon materials, the efficiency to produce pores is relatively low compared with the method using strong acid/basic agents.

2.3 Interlayer spacing engineering

Interlayer spacing of carbon materials is an important parameter that affects the ion-intercalation behavior and thus the electrochemical performance of carbon electrodes (Fig. 3b). To decrease the interlayer spacing of carbon materials, high temperature treatment is the most frequently adopted strategy. During the graphitization heat treatment at 2000–3000 °C, carbon atoms rearrange to relieve the internal stresses along with the formation of a three-dimensional graphite structure or relatively ordered microcrystallites.[87,88] The interlayer spacing of carbon materials gradually decreases together with the removal of defects/functional groups. Normally, the graphitization process takes even several days to obtain heteroatom-free carbon materials. In the presence of catalysts (Fe, Cr, Co, Ni, *etc.*), the graphitization temperature can be largely decreased (500–1800 °C) and the treatment duration can also be shortened, although the metallic catalysts are likely encapsulated by the graphitic carbon.[89–91] The interlayer spacing of carbon aerogel after catalytic graphitization can reach 0.336 nm, very close to 0.335 nm of pure graphite.

In addition, increasing the interlayer spacing of layered materials is attractive to facilitate ion diffusion and intercalation under electrochemical conditions. Due to the inert feature of graphite, a two-step oxidation–reduction process was applied,[92,93] where graphite was first oxidized to graphite oxide and further reduced at 150–600 °C. Owing to the strong covalent bond

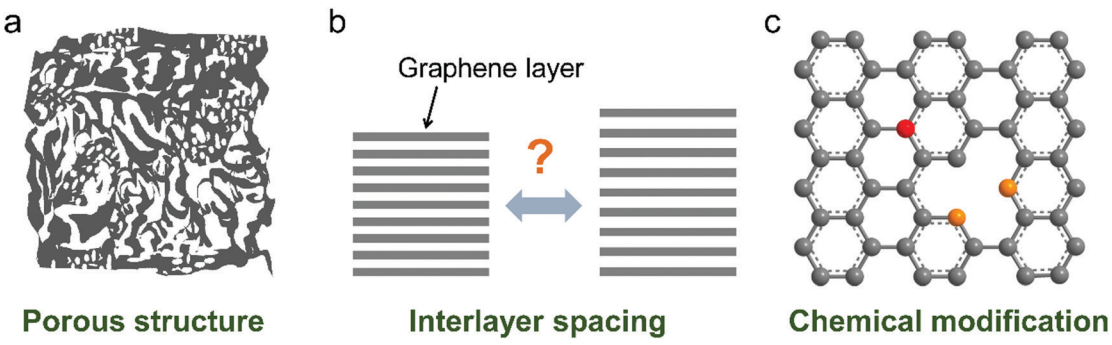

Fig. 3 Common strategies to modify carbon materials, including (a) pore construction, (b) interlayer spacing engineering, and (c) chemical modification.

between oxygen and graphite, there are oxygen functional group residuals on graphite even after reduction, leading to the large interlayer spacing of graphite (0.34 nm or 0.37–0.43 nm) while maintaining the long-range-ordered layered structure. Another way to enhance the layer distance of graphite is pre-intercalation.[94–96] Atomic or molecular layers of chemical species can intercalate into graphite sheets. A stage-I $FeCl_3$–graphite intercalation compound (GIC) has been synthesized by reacting $FeCl_3$ with graphite. The interlayer spacing of graphite was increased to 0.938–0.960 nm. Further, the combination of chloroaluminate anion intercalation, thermal expansion and electrochemical hydrogen evolution on graphite foil led to the formation of three-dimensional graphene foam consisting of thin-layer graphene sheets and well-defined vertical channels.[97] Such approaches avoid the introduction of large amounts of functional groups or oxidation-induced defects into graphene sheets.

2.4 Chemical modification of carbon materials

The chemical composition and surface properties of carbon materials have a significant impact on their electrochemical behavior including solid electrolyte interphase (SEI) formation, electrochemical stability and ion intercalation process. There are several ways to modify the composition of carbon materials such as heteroatom doping (Fig. 3c), surface functionalization and heterogeneous species intercalation.

Introducing F into graphite leads to fluorinated graphite, which has been commercialized in primary LIBs. Deeply oxidizing graphite produces GO,[53] the main source of rGO. Unlike C–F and C–O(=O) dangling bonds[98] in fluorinated graphite and GO, boron (B) can be incorporated into the graphite lattice, which brings about enhanced graphitization and modified electronic properties.[99] B-Doped graphite can be prepared *via* mixing a pitch coke and boron oxide powders followed by baking at 1000 °C and graphitization at 2800 °C. The fabricated product with 3.8 wt% B doping exhibited an interlayer spacing of 0.335 nm and a large crystallite size over 100 nm.[100] The high graphitization of B-doped graphite was attributed to the catalytic effect of B substitution.

Fluorination and oxidation can also be controlled just on the outer surface of graphite under mild reaction conditions.[101] To passivate the reactive surface of graphite, particularly the edge planes, mild oxidation of graphite by air generates carbonyl, carboxyl and hydroxyl groups. After lithiation, this dense layer of oxides becomes part of the SEI and inhibits electrolyte decomposition.[102,103] In addition, hydrogenation of partially oxidized graphite can be used to fabricate hydrogenated graphite.[104] To enhance the electrochemical stability of graphite, surface coating is effective to suppress the potential exfoliation of graphite. Polydimethylsiloxane,[105] nitrophenyl layer,[106] AlF_3,[107] and oxide[108,109] coatings have been investigated for raw graphite, which endow graphite electrodes with high electrochemical stability and low irreversible capacity. Benefiting from high conductivity, stable intercalation-deposition or intercalation-alloying reactions and high compatibility with nowadays LIB infrastructure, these graphite-based hybrids offer a practical insight into developing high-energy electrodes.

In contrast to chemically inert graphite, graphene with atomic-level thickness can be well modulated with respect to chemical composition. Graphene can reversibly react with atomic hydrogen, which transforms the highly conductive zero-overlap semimetal into an insulator.[110] The formed graphane shows crystallinity and retains the hexagonal lattice. In-plane B substitutional doping into graphene was accomplished *via* chemical vapor deposition.[111] Other heteroatom-doped (N, P, O, S, F, Cl, Br, and I) graphene can be fabricated by both *in situ* synthesis methods and post treatment (chemical vapor deposition, ball milling, bottom-up synthesis, thermal annealing, wet chemical method, plasma, photochemical method, and arc discharge).[112] Similarly, heteroatoms can be doped in soft-carbon and hard carbon during the thermal synthesis.[113–116] The heteroatoms in the graphitic planes can act as reactive adsorption sites for alkaline cations and expand the interlayer spacing, thus enhancing the capacity.

Moreover, the electrode design also influences the ion transport across the electrode and the ion intercalation kinetics, especially for practical thick electrodes with high mass loadings.[117,118] Claire Villevieille *et al.*[119] demonstrated thick graphite electrodes with a vertically aligned architecture, which was enabled by superparamagnetic Fe_3O_4 nanoparticles adsorbed on graphite flakes. The platelet orientation can be magnetically controlled in a simple, inexpensive, and effective way. The vertically aligned graphite flakes decrease the tortuosity of the ion path throughout the electrode by a factor of four. Thus, the capacity of graphite at high rates was largely enhanced by providing a shorter pathway for Li^+ diffusion. Such a strategy can be potentially extended to other electrode materials for high-rate devices.

3. Electrochemistry and fundamentals

Ion intercalation/deintercalation is the most classic charge storage mechanism in rechargeable battery technologies. The process involves a simple and reversible solid-state redox reaction of the host materials. In the charge storage/release process, mobile guest ions in the electrolyte are reversibly inserted/extracted into/from the interlayer space or large channels of the host materials. The ions keep their ionic properties during intercalation, so that their diffusion within host materials is forced by the electrostatic interaction between ions and host materials. Meanwhile, the intercalation process would lead the host materials to undergo certain volume expansion. As an ideal model, graphite intercalation compounds (GICs) provide the basic understanding of the charge-storage mechanism of carbon for battery technologies. The studies on ionic GICs can be traced back to as early as 1841.[120] Graphite with a large π-electronic network can delocalize and stabilize with either an excess of electrons in the antibonding π*-band or electron holes in its bonding π-band, enabling graphite with redox amphotericity and leading to donor-type or acceptor-type GICs. The great success of GICs in batteries further spurred research to understand the battery electrochemistry of other carbon

nanostructures (graphene, CNTs, disordered carbon). Therefore, this part mainly concentrates on the fundamental electrochemistry associated with the ion-intercalation behavior of carbon materials.

3.1 Cation intercalation

Group IA alkali elements (Li, Na, K) are attractive as intercalants into graphite, because they can easily lose the outermost electrons and form ionic bonds with non-metallic carbon. The formation of donor-type GICs can be expressed as reaction (2), where alkali elements donate an electron to the delocalized π-electron carbon networks. However, the intercalation behavior of Li^+, Na^+, and K^+ into the carbon interlayer shows quite a different electrochemical behavior, which relies on the different chemical and physical properties of Li, Na, K and their cations (Table 1). Along with the increase of the atomic number (from Li to K), alkali elements show increasing relative atomic mass and Shannon's ionic radii, as well as decreasing Pauling electronegativity. In early studies, potassium ion batteries (KIBs) did not attract much attention, because K^+ possesses larger relative atomic mass and ionic radii than Li^+ and Na^+. Nevertheless, it was gradually revealed that the smaller ionic radii of alkali elements resulted in stronger coulombic interaction with the solid host, which causes a larger energy barrier for the mobility of ions within host materials. Moreover, Stokes' radii and the desolvation energy in propylene carbonate (PC) follow the order $Li^+ > Na^+ > K^+$,[121] implying the possibility of Na^+ and K^+ as suitable charge carriers for batteries. In addition, since the natural abundance of Na and K greatly exceeds that of Li (2.3 mass% for Na in the earth's crust *vs.* 1.5 mass% for K and 0.0017 mass% for Li), much lower material cost is expected for the future sodium-ion battery (NIB) and KIB technologies than LIB technology. All these factors together stimulate the intense efforts simultaneously devoted to the research on LIBs, NIBs and KIBs.

$$C_n + M^+ + e^- \rightleftharpoons C_n{}^- M^+ \quad (2)$$

3.1.1 Li^+-Intercalation chemistry. Except H^+, Li^+ is the smallest cation with high energy density and fast kinetics. This fact induces the primary interest to develop rechargeable batteries by using Li^+-intercalation chemistry. Graphite is one of the earliest studied anode materials and still in use as a commercial anode for LIBs. By far, the Li^+-intercalation mechanism of graphite has been well elucidated as illustrated in Fig. 4. In the full intercalation situation, the intercalated Li^+ is immobilized by two neighbored graphene planes, and each Li^+ takes the lowest-energy place above the center of an individual hexagonal carbon ring (Fig. 4a and b), forming the LiC_6 compounds with a theoretical capacity of 372 mA h g^{-1}.[122] Along the *c*-direction of graphite, Li^+ takes the direct adjacent place between the graphene layers in a Li–C_6–Li–C_6 sequence. The Li^+-intercalation potential for graphite is generally below 0.5 V *vs.* Li^+/Li.

The phase transformation of graphite during Li^+-intercalation proceeds *via* a known 'staging' mechanism for GICs,[126] as shown in Fig. 4c. Li^+ tends to fully intercalate into distant graphene layers before occupying the near/neighboring graphene layer, expressing a signature stage structure. The order of the stage is defined by the number of graphene layers between two adjacent Li layers. Different potential steps in the discharge/charge profile and sharp redox peaks disclose the sequential formation of stage-III, stage-II, and stage-I during Li intercalation. Previous studies established two models to simulate the graphite strain, namely Rüdorff model and Daumas–Hérold model (Fig. 4d).[127,128] Compared with the sequential filling of ions in alternating graphene interlayer spaces (Rüdorff model, Fig. 4c), the Daumas–Hérold model provides a more reasonable interpretation of strain formation, as graphene layers deform around the intercalated ions. To index the stage number (n) of GICs, two characteristic ($00n + 1$) and ($00n + 2$) plane peaks appearing in the XRD patterns of GICs will be analyzed (Fig. 4b and c). Based on eqn (3) and (4), n can be calculated from eqn (5).[129,130] The $n + 1$ and d_{00n+1} represent the index of ($00n + 1$) planes oriented in the stacking direction and the observed value of the spacing between adjacent planes, respectively. The key structural parameters of GICs like the periodically repeating distance (I_c), the intercalant gallery height (d_i), the gallery expansion (Δd) and the percent expansion (Δc) can be achieved by eqn (6) and (7). With the assistance of XRD and Raman spectroscopy, four stages were observed for the Li^+ intercalation process into graphite. Both XRD[123] and high-resolution transmission electron microscopy (TEM) image[131] revealed the interplanar distance to change from 3.35 Å for pristine graphite to 3.70 Å for stage-I (LiC_6), implying a Δc of 110% (Table 2).

$$d_{00n+1} = I_c/(n + 1) = \lambda/(2 \sin \theta_{00n+1}) \quad (3)$$

$$d_{00n+2} = I_c/(n + 2) = \lambda/(2 \sin \theta_{00n+2}) \quad (4)$$

$$n = [1/(\sin \theta_{00n+2}/\sin \theta_{00n+1} - 1)] - 1 \quad (5)$$

$$I_c = d_i + (n - 1) \times 3.35 = \Delta d + n \times 3.35 = (n + 1) \times d_{00n+1} \quad (6)$$

$$\Delta c = [I_c/(n \times 3.35) - 1] \times 100\% \quad (7)$$

The limited capacity, poor Li^+ diffusion kinetics as well as low rate capability have restricted the application of graphite anodes for Li-ion batteries, which stimulates a strong motivation to develop nanostructured carbon materials for hosting Li^+.

Table 1 Chemical and physical properties of Li, Na, K and their cations for rechargeable batteries. SHE refers to standard hydrogen electrode

Element	Li	Na	K
Atomic number	3	11	19
Electronic configuration	$[He]2s^1$	$[Ne]3s^1$	$[Ar]4s^1$
Relative atomic mass	6.94	23.00	39.10
Pauling electronegativity	0.98	0.93	0.82
Shannon's ionic radii/Å	0.76	1.02	1.38
Stokes' ionic radii in PC/Å	4.8	4.6	3.6
Desolvation energy in PC/kJ mol^{-1}	215.8	158.2	119.2
E° (V) *vs.* SHE	−3.04	−2.71	−2.93
E° (V) *vs.* Li^+/Li	0	0.33	0.11
Crust abundance/mass %	0.0017	2.3	1.5
Crust abundance/molar %	0.005	2.1	0.78
Cost of industrial grade metal/$ ton^{-1}	100k	3k	13k

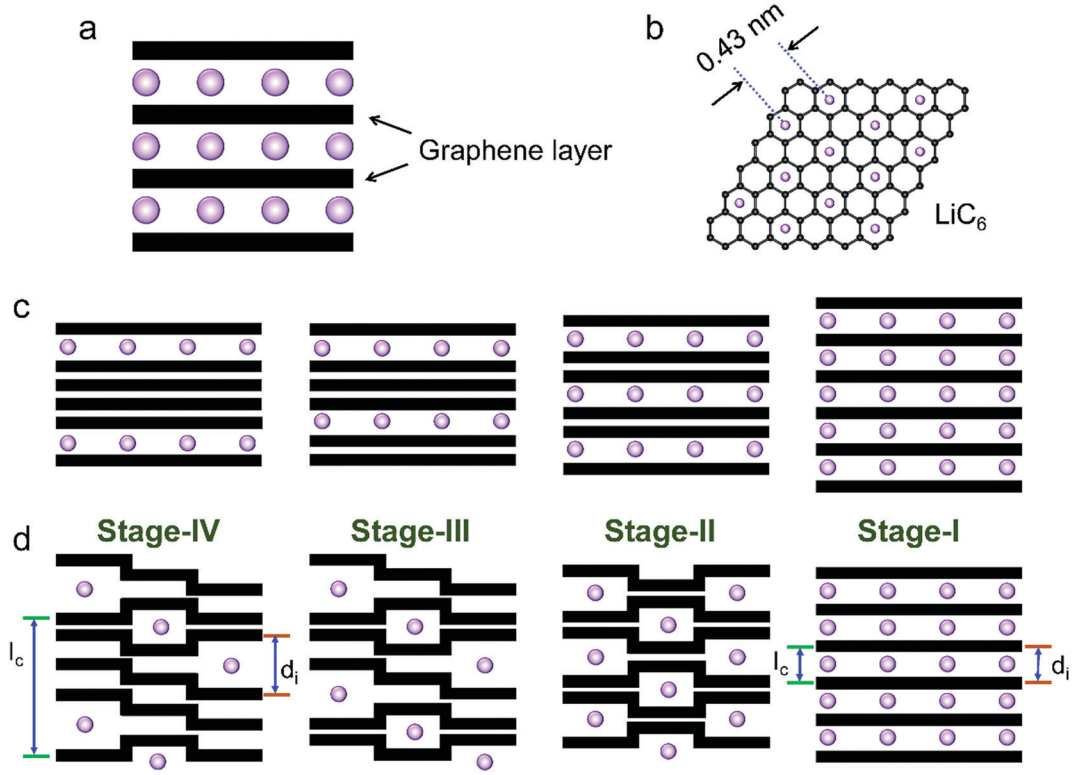

Fig. 4 Schematic illustration of (a) Li-intercalated graphite and (b) the formed LiC_6 structure. Two models of the stage formation process during Li^+ intercalation into graphite: (c) Rüdorff model and (d) Daumas–Hérold model.

Among various carbon-based LIB anodes, graphene is highly promising and has been extensively investigated, which can provide a large gravimetric capacity (>1000 mA h g^{-1}). However, the Li-storage mechanism is still under drastic debate with respect to both experimental and theoretical understanding.[133] One view is that single-layer graphene stores Li^+ by an adsorption approach, which is completely distinct from the staging intercalation mechanism of graphite. Dahn *et al.*[134] assumed that both sides of single-layer graphene can store one lithium ion, forming Li_2C_6 stoichiometry with a theoretical specific capacity of 744 mA h g^{-1}. Sato *et al.*[135] suggested that Li ions can be trapped within the benzene ring with a covalent bond between neighboring Li atoms, yielding LiC_2 stoichiometry with a theoretical specific capacity of 1116 mA h g^{-1}. On the other hand, some research studies claimed that since Li atoms only intercalate into the graphene interlayer or the space between graphene and substrate, adsorption of Li on the pristine single graphene layer is not possible. Recently, Ji *et al.*[50] synthesized a high-quality free-standing bilayer graphene foam by a high-temperature-switched CVD route (Fig. 5a). Evidenced by the cyclic voltammetry (CV) curve (Fig. 5b) and the simulation results, they concluded that the Li-storage behavior in bilayer graphene is similar to that in graphite, experiencing different intercalation stages. They also established a planar Li-storage model, as shown in Fig. 5c. Controversially, Kühne *et al.*[132] took use of *in situ* low-voltage TEM to study the intercalation of lithium into bilayer graphene (Fig. 5d). They found the superdense accommodation of Li^+ within bilayer spaces, implying that the Li-storage capacity in bilayer graphene is far beyond that of LiC_6 (Fig. 5e). Further in-depth investigation of the Li^+-storage mechanism of bilayer graphene is still needed. To provide an understanding of the Li-ion diffusion pathway, Lee's group[51] used a CVD method to grow single-layer graphene with a perfect basal plane and few-layer graphene with a rich edge plane. By comparing the capacity of these two kinds of graphene, they concluded that defects accelerated the Li-ion diffusion perpendicular to the basal plane, while the diffusion parallel to the plane was hindered by Li-ion aggregation on the defect sites (Fig. 5f). Density functional theory (DFT) demonstrated the possible Li ion diffusion through the basal plane by using carbon divacancies or higher order defects as transport channels.

Table 2 Summary of donor-type GICs reported for rechargeable batteries

Cations	N	d_i (Å)	Δc (%)	Electrolyte	Ref.
Li^+	1	3.7	10	1 M $LiClO_4$ in EC/DME	123
Na^+-DEGDME	1	11.62	247	1 M $NaPF_6$ in DEGDME	124
K^+	1	5.35	60	0.8 M KPF_6 in EC/DEC	125

Li-ion storage in CNTs has also been explored in the past few years. It is believed that Li-ion intercalation can occur on the outside of the walls, in the inner core, as well as in the space between multilayers through the topological defects on the side walls or the open ends.[136–140] Generally, the gravimetric capacity of CNTs heavily relies on their structures and morphology (ranging from 300 to 1500 mA h g^{-1}). The capacity difference among different CNTs can be assigned to many structural

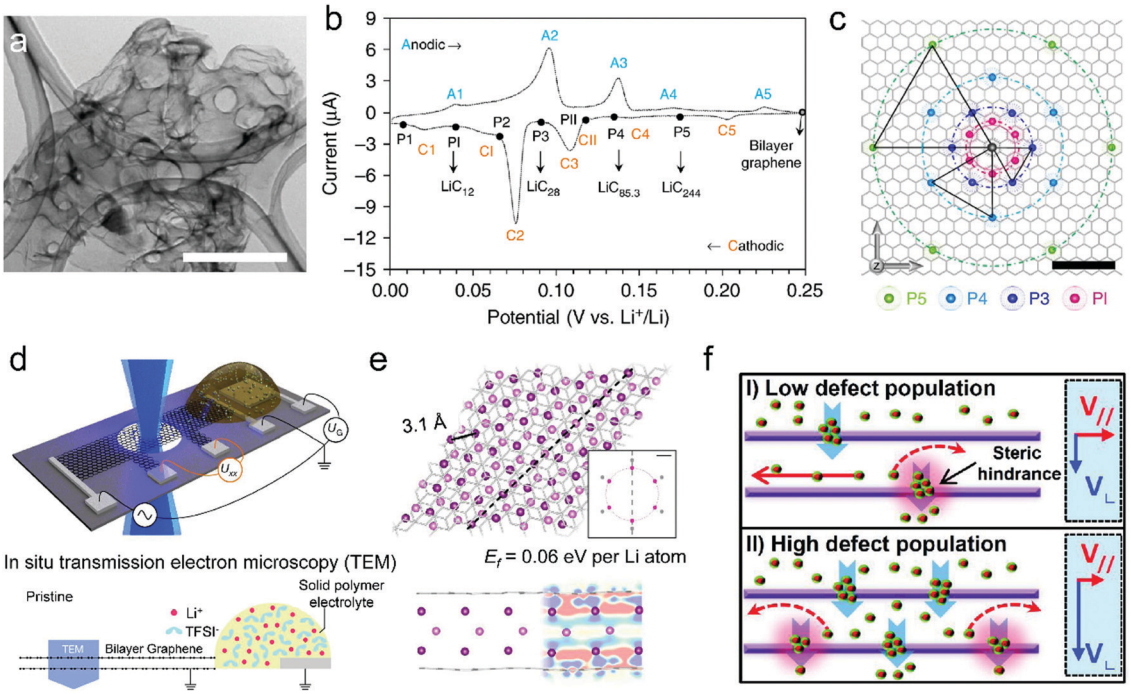

Fig. 5 (a) Transmission electron microscopy (TEM) image of the free-standing bi-layer graphene film (scale bar, 1 μm). (b) CV curve of the bi-layer-graphene film and the corresponding LiC_x phase. (c) The proposed in-plane distribution of Li in the lithiated bi-layer graphene. Reproduced from ref. 50 with permission from Springer Nature. (d) Schematic of the device for *in situ* TEM measurements. (e) Fully optimized tri-layer Li between AB-stacked graphene sheets obtained from DFT calculations. Reproduced from ref. 132 with permission from Springer Nature. (f) Schematics of the proposed Li diffusion mechanism through defects on the basal plane with different defect population. Reproduced from ref. 51 with permission from American Chemical Society.

factors, such as chirality, diameter, length, defects, and functional heteroatoms/groups.

Another important category of carbon materials for Li-ion storage is disordered carbon with a large proportion of sp^2 carbon. The Li-ion storage behavior of disordered carbon is featured by multiple mechanisms, including intercalation, adsorption, cavity/pore filling, surface/interface storage, and heteroatom/functional group contribution.[122,135,141–143] With contributions from different mechanisms, the gravimetric capacity of disordered carbon substantially exceeds that of graphite (LiC_6). Although disordered carbon materials show advantageous capacity, their application is severely restricted by two issues, massive irreversibility of the first lithiation process (or low first-cycle coulombic efficiency (CE)) and apparent hysteresis between charge and discharge curves. The irreversible capacity is mainly assigned to the formation of a surface passivation layer on carbon materials due to electrolyte reduction, which is also named SEI.[144] In fact, the SEI serves as a prerequisite of cell stability for electrolyte/electrode contact with unstable thermodynamics. Such a passivation layer was found in most of the LIB anodes. For graphite, the irreversible capacity only accounts for 10–20% of the first lithiation capacity.[122] It was revealed that SEI formation is heavily dependent on the specific surface area.[133] Thus, disordered carbon shows much higher irreversible initial capacity, as it generally possesses larger specific surface area than the highly compacted graphite.

3.1.2 Na^+-Intercalation chemistry. Replacing resource-limited Li^+ with earth-abundant Na^+ is a sensible idea to design new types of batteries, since the physicochemical properties between Li^+ and Na^+ are similar. However, the development of NIBs is not a simple element substitution. The slightly bigger size of Na^+ compared to that of Li^+ causes a largely distinct guest–host interaction for Na^+ intercalation, which further results in pronouncedly different ion diffusion behavior, redox properties and interfacial compatibility. One of the classic cases is that graphite, the 'star material' for hosting Li^+, has a very limited capability to accommodate Na^+ (corresponding to NaC_{186} at room temperature).[147] The mismatch between the graphite interlayer distance and large Na^+ size is generally considered as the reason for the limited intercalation of Na^+ into graphite. However, this fact cannot fully explain the difficulty of intercalating Na^+ into graphite, as the even larger K^+ can easily intercalate into graphite. DFT calculations found that Na^+ intercalated graphite compounds (NaC_6 and NaC_8) are thermodynamically unstable, as the C–C bonds are apparently stretched (Fig. 6a).[145] On the other hand, the high Na^+/Na potential (340 mV higher than Li^+/Li) is believed to be another significant reason for the limited Na^+ intercalation into graphite. It means that the ion-intercalation reaction of graphite would not happen below 340 mV *vs.* Li^+/Li in a Na^+-containing electrolyte, as Na plating prefers to occur (Fig. 6b).[147] In addition, Liu *et al.*[146] performed theoretical studies on the formation energy of different cation-intercalated graphite compounds (Fig. 6c). Their investigations

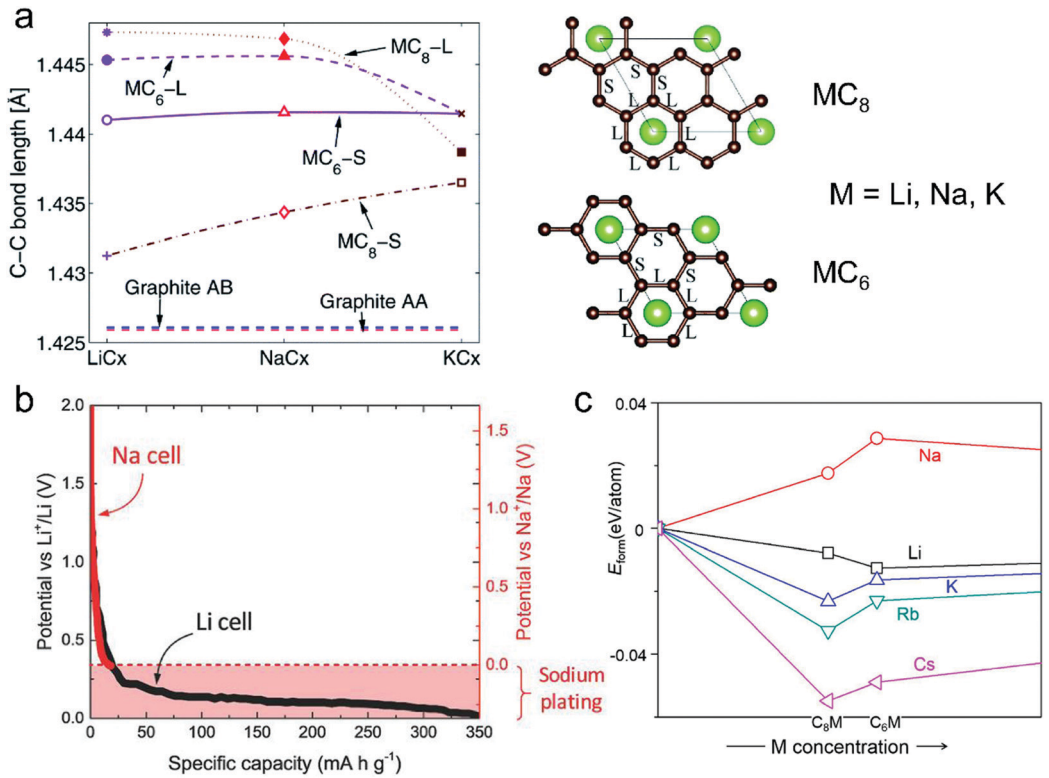

Fig. 6 (a) In-plane C–C long (L) and short (S) bonds in MC_x intercalation compounds and graphite AB and artificial graphite AA. Configurations of long (L) and short (S) bonds for MC_6 and MC_8 are illustrated in the right figures. Reproduced from ref. 145 with permission from The Royal Society of Chemistry. (b) Second discharge curve of graphite in Li (black line) and Na cells (red line) with $LiPF_6$ in EC/DEC and $NaPF_6$ in EC/DEC, respectively. Reproduced from ref. 40 with permission from Wiley-VCH. (c) Calculated formation energies of alkali metal (M)–graphite compounds. Reproduced from ref. 146 with permission from United States National Academy of Sciences.

reveal that the formation energy of Na-intercalated graphite (NaC_8 and NaC_6) is above zero, explaining the difficult intercalation of Na^+ into graphite.

There are two strategies to promote the intercalation of Na^+ into graphite. The first one is to increase the graphite layer distance.[93,149] It was simulated in theory, when the graphite layer distance increases from the initial 0.335 to 0.37 nm, the Na^+ intercalation into graphite occurs with a low energy barrier.[150] Chou and co-authors[151] found that rGO with an interlayer distance of 0.37 nm could deliver a high capacity of 174.3 mA h g^{-1} as the anode of NIBs. Wen *et al.*[93] reported that the partially reduced GO with an interlayer distance of 0.43 nm exhibited a high Na^+-storage capacity of 284 mA h g^{-1} at 20 mA g^{-1}. This remarkable capacity was assigned to the increased intercalation space for accommodating Na^+. The other strategy is to enable the co-intercalation of Na^+ and solvent in diglyme or ether-based electrolytes.[124,152–155] Recently, Kang *et al.*[156] revealed that the co-intercalation of Na^+ and solvent could avoid the direct interaction between Na^+ and graphite layer, greatly reducing the corresponding repulsive interaction. To enable such co-intercalation, a high solvation energy of Na^+ is required for solvents, which is capable of forming stable Na–solvent complexes. However, the Na^+-storage performance of graphite enabled by the co-intercalation strategy suffers from some critical issues, such as low specific capacity (100 mA h g^{-1} in a diglyme-based electrolyte, 150 mA h g^{-1} in an ether-based electrolyte), large volume expansion (350%, as shown in Table 2), and high consumption of solvent.

Different from pristine graphite, disordered carbon materials, especially hard carbon, have been recognized as favorable SIB anode materials. The charge–discharge curve of disordered carbon during Na^+ intercalation/de-intercalation behaves like Fig. 7, showing a sloping region with potential above 0.1 V and a low potential plateau.[71] In brief, four kinds of Na^+-storage forms were proposed in the previous literature,[40] including (1) capacitive Na-ion adsorption on the accessible surface, (2) pseudocapacitive Na-ion storage associated with the carbon defects, heteroatoms, and functional groups, (3) Na^+-intercalation into the graphitic layers and (4) Na clustering within the micropores. However, it remains challenging to establish a clear relationship between the voltage curve of hard carbon and specific Na^+-storage mechanisms. For example, Stevens and Dahn[157] proposed the 'house-of-cards' model, which assigned the high voltage sloping region to Na^+ insertion into the turbostratic graphite microdomains and the low voltage plateau region to Na^+ adsorption within the microporosity (Fig. 7a). However, other recent studies[148] demonstrated that the Na^+-storage mechanism in the high voltage sloping region is associated with Na^+ adsorption on the defective sites of carbon and filling of micro-/nano-pores, while the mechanism in the plateau region is the insertion of Na^+

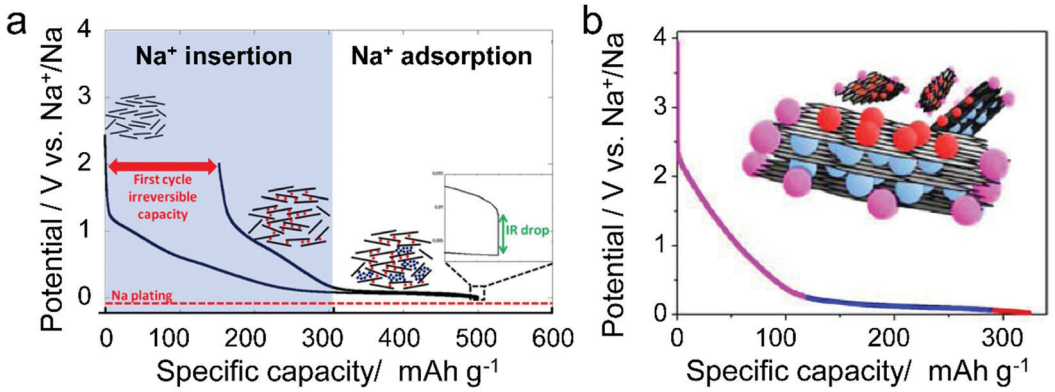

Fig. 7 Typical voltage profile of hard carbon for Na-storage with two kinds of proposed mechanism. (a) Two-phase mechanism including intercalation and pore filling. Reproduced from ref. 71 with permission from The Electrochemical Society. (b) Three-step Na-storage mechanism. Reproduced from ref. 148 with permission from American Chemical Society.

into the carbon lattice and adsorption of Na^+ at the pore surface (Fig. 7b). The ongoing debate on the Na-ion storage mechanism of hard carbon calls for further *in situ* electrochemical studies on hard carbon materials for Na^+ storage with the assistance of multiple characterization techniques. In addition, heteroatom doping can also promote the Na^+-storage capability of disordered carbon, as it can provide additional Na^+-adsorption sites, and improve the surface wettability and electronic conductivity.[158,159] Of note is that the issues for Li^+-storage in disordered carbon also exist in the case of Na^+ storage, which is the low CE during the first cycle associated with the formation of SEI film.

3.1.3 K^+-Intercalation chemistry. The K^+-storage behavior of graphite is similar to its Li^+-storage behavior, showing the apparent staging mechanism. In the final K^+-intercalated graphite, K^+ occupies the space between each neighboring graphite layer. In 2015, Ji's group[125] reported the possibility of graphite as the anode for KIBs in an electrolyte of 0.8 M KPF_6 in EC/diethyl carbonate (DEC) mixed solvent. The synthetic graphite showed high initial discharge and charge capacities of 475 mA h g^{-1} and 274 mA h g^{-1} at 7 mA g^{-1}, respectively, indicating the formation of KC_8 (Fig. 8a and b). The voltage profile (Fig. 8a) and *in situ* XRD (Fig. 8b) measurements disclosed the three-stage K^+-intercalation into graphite, namely KC_{36} (stage-III) at 0.3–0.2 V *vs.* K^+/K, KC_{24} (stage-II) at 0.2–0.1 V *vs.* K^+/K, and KC_8 (stage-I) at 0.01 V *vs.* K^+/K. According to the eqn (6) and (7), I_c and Δc of KC_8 are 5.35 Å and 161%, respectively (Table 2). During the de-intercalation of K^+, stage-I was observed to disappear until 0.3 V *vs.* K^+/K. Afterwards, stage-III (KC_{36}) was identified between 0.3 and 0.5 V *vs.* K^+/K. This work provided pragmatic opportunities for developing K^+ based energy storage technologies. Soon after, Hu's group[160] also reported the K^+ intercalation/de-intercalation behavior of graphite in an electrolyte of 0.5 M KPF_6 in EC/DEC. By simulating the potential K-intercalated graphite compounds *via* DFT calculations (Fig. 8c and d), they demonstrated a more stable staging mechanism from KC_{24} (stage-III) to KC_{12} (stage-II) and finally to KC_8 (stage-I). KC_8, rather than KC_6, was confirmed as the most stable potassiation product for graphite, as K stripping/plating would occur along with the decrease of potential. Also, they found that the staging sequence from KC_{24} (stage-II) to KC_8 (stage-I) is impossible, because the potential should be increased when KC_{24} (stage-II) transforms to KC_8 (stage-I). Moreover, KC_{24} (stage-III) is more stable than KC_{24} (stage-II). Due to the controversial conclusion from these two studies, more in-depth analysis about the staging process of K^+ intercalation into graphite is still needed.

Besides the graphite material, graphene and disordered carbon also show pronounced K^+-storage capability. Compared with the voltage profile of graphite with an obvious voltage platform, graphene and disordered carbon generally exhibit more sloping voltage curves, which is particularly obvious in the high voltage region. The corresponding K^+-storage mechanisms are close to the mechanisms of similar materials for Li^+ and Na^+ storage, including insertion into graphitized (micro)domains, adsorption on functional groups/heteroatoms, capacitive contribution from surface/nanovoids (all voltage ranges), *etc.*[41,42] Insertion into graphitized (micro)domains occurs at potentials below 0.5 V *vs.* K^+/K, which is similar to K^+ staging intercalation into graphite. In general, the interlayer spacing of graphene materials with defects/functional groups and the graphitized microdomains of disordered carbon are much larger than that of graphite. This fact leads to a high kinetics of K^+ diffusion within graphene and disordered carbon. In addition, it was demonstrated that K^+-adsorption onto heteroatoms (*e.g.* N, B, S) and functional groups also contributed to a huge capacity of carbon anodes. With the assistance of *ex situ* Raman measurements, Share *et al.*[161] found that these adsorption processes mainly took place in the potential window of 0.4–0.8 V *vs.* K^+/K, and did not affect the staging insertion of K^+ into graphitized domains. Moreover, in most carbon materials with high specific surface areas, capacitive contribution to K^+-storage capacity is also considerable. Capacitive contribution to the whole capacity can be qualitatively analyzed by power-law eqn (8) and quantitatively distinguished by eqn (9) based on CV data at various scan rates.[162] In eqn (8), a and b are adjustable values, and the current (i) dependence on the scan rate (v) can be revealed. If b approaches 1, then the main capacity contribution comes from capacitive contribution. Meanwhile, if b approaches 0.5, the diffusion-controlled capacity contribution is dominant. In eqn (9), the response current (i) is divided into the sum of capacitive contribution (k_1v) and diffusion-controlled

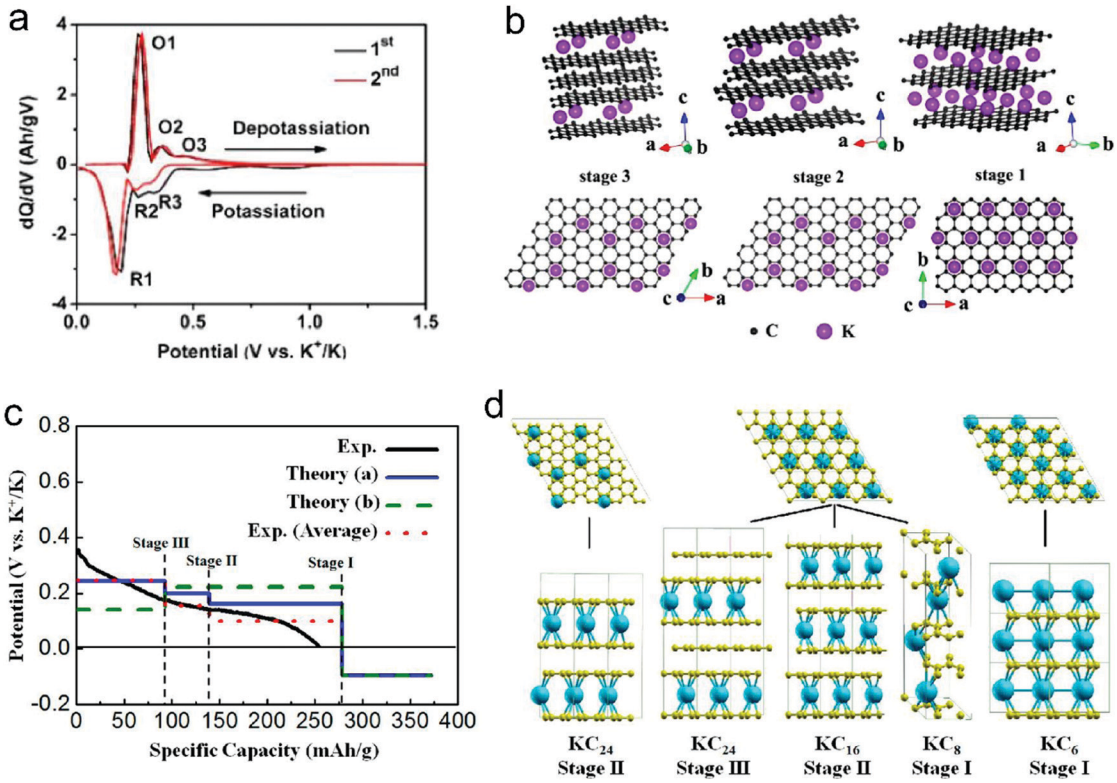

Fig. 8 (a) dQ/dV profiles of K^+-intercalated graphite. (b) Structure diagrams of K^+-intercalated graphite at different stages, side view (top row) and top view (bottom row). Reproduced from ref. 125 with permission from American Chemical Society. (c) Calculated potential profile for K ion intercalation into graphite for different staging scenarios. The blue line (Theory (a)) corresponds to an intercalation staging: KC_{24} (stage-III) → KC_{16} (stage-II) → KC_8 (stage-I). The green dotted line (Theory (b)) corresponds to calculated values for the previously reported staging: KC_{24} (stage-II) → KC_8 (stage-I). The red dotted line corresponds to the averaged experimental data shifted by 26 mA h g^{-1} to correct the capacity contribution from SEI formation. (d) Scheme of the different stages of K-intercalated graphite; K shown in blue and C in yellow. Reproduced from ref. 160 with permission from American Chemical Society.

contribution ($k_2v^{1/2}$). The fundamental understanding of K^+-storage in carbon materials is still at the preliminary stage, and more in-depth investigation of storage sites, diffusion pathway, and kinetics associated with K^+ storage is critically needed.

$$i = av^b \quad (8)$$

$$i = k_1v + k_2v^{1/2} \quad (9)$$

3.2 Anion intercalation

Beside cations, negatively charged ions can also intercalate into graphite to form acceptor-type GICs, as illustrated by reaction (10).

$$C_n + A^- \rightleftharpoons C_n^+A^- + e^- \quad (10)$$

Anions like HSO_4^-, PF_6^-, ClO_4^-, $AlCl_4^-$, $TFSI^-$, FSI^-, BF_4^-, *etc.* have been explored for acceptor-type GICs.[173] Fundamentally, anion intercalation into graphitic carbon is the basis of recently reported dual-ion batteries (DIBs) and Al-ion batteries (AIBs). Compared to conventional alkaline metal-rich transition-metal oxide cathodes ($LiCoO_2$, $LiMnCoNiO_x$, *etc.*), the main advantages of graphitic carbon cathodes lie in the high working potential (up to 5.3 V *vs.* Li^+/Li), low cost, low CO_2 emission during the production process, high sustainability, and zero-oxygen release in overcharge, making them promising for sustainable grid storage.

3.2.1 Anion intercalation mechanism. Anion intercalation into graphitic carbon is also featured with the "staging" intercalation mechanism.[130] The "stage" was defined by the sorting sequence of the occupied galleries and neighboring graphene sheets along the *c*-axis (Fig. 4c and d). Not every gallery has to be uniformly occupied during the intercalation process, which can be ascribed to the conductive and flexible graphene sheets with minimized electronic and mechanical strain energies.[174,175] According to eqn (6) and (7), d_i and Δc correlate strongly with the anion type in GICs (Table 3). It was reported that stage-I $Br^{-0.05}Cl^{-0.25}$-intercalated graphite displayed a Δc of 104% on account of a d_i of 6.85 Å.[172,176] For PF_6^-, $TFSI^-$, fluorosulfonyl-(trifluoromethanesulfonyl)imide ($FTFSI^-$), FSI^- and BF_4^- anions, *in situ* XRD measurements reveal that a stage-I GIC delivers an expansion of 130–140% with d_i in the range of 7.83–8.05 Å.[129,166,167] In contrast, an $AlCl_4^-$ based GIC shows a high d_i of 9.54 Å due to the large size of $AlCl_4^-$. Apparently, d_i and Δc of acceptor-type GICs are much higher than those of donor-type GICs (3.70 Å and 10% for Li^+-GICs and 5.35 Å and 60% for K^+-GICs).

It is worth noting that during anion intercalation, both clear two-phase transitions and solid solution transitions exist.[129]

Table 3 Summary of acceptor-type GICs reported for rechargeable batteries

Anions	n	d_i (Å)	Δc (%)	Electrolyte	Ref.
PF_6^-	1	7.77–7.83	133	2 M $LiPF_6$/EMC	163 and 164
$TFSI^-$	1	7.95	137	1 M LiTFSI/Pyr_{14}TFSI + 2 wt% ES	165
$FTFSI^-$	1	7.97	137	1 M LiFTFSI/Pyr_{14}FTFSI	166
FSI^-	1	7.83	134	5 M KFSI/EC/EMC	167
BF_4^-	1	7.96–8.06	140	1 M $LiBF_4$/EMS	166
$AlCl_4^-$	3	9.54	—	EMImCl + $AlCl_3$	168–171
$Br^{-0.05}Cl^{-0.25}$	1	6.85	104	21 mol kg^{-1} LiTFSI + 7 mol kg^{-1} LiTfO/water	172

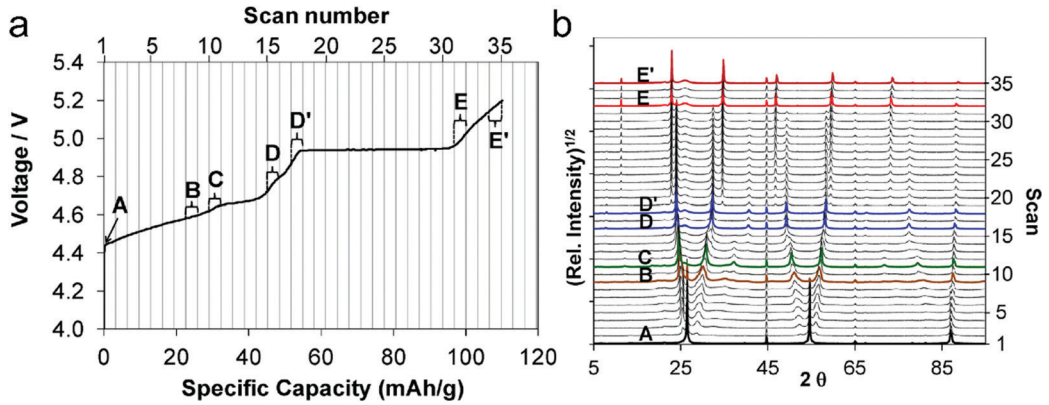

Fig. 9 (a) First charge curve and (b) corresponding *in situ* XRD spectra (5–90° 2θ) of the graphite cathode during PF_6^- intercalation. Reproduced from ref. 129 with permission from American Chemical Society.

In the former, one stage GIC is transformed to another lower-stage GIC, while in the latter (D–D′ and E–E′ in Fig. 9a and b), no lower stage GIC is formed and anion storage is accompanied by dense anion packing in the existing stage.

3.2.2 Potential origin of anion intercalation. The high working potential of anion intercalation is a key advantage of graphitic carbon cathodes for high-voltage energy storage applications. To reveal the origin of potential for anion intercalation into graphitic carbon, a simplified Li//C half cell is adopted (eqn (11)–(13)). The anion intercalation potential (*vs.* Li^+/Li) equals the cell voltage of the Li//C cell. During the operation of the cell, the following one-electron reactions occur on the anode and cathode:

$$\text{Anode: } Li^+ + e^- \rightleftharpoons Li \quad (11)$$

$$\text{Cathode: } C_n + A^- \rightleftharpoons C_n^+A^- + e^- \quad (12)$$

$$\text{Overall reaction: } Li^+ + A^- + C_n \rightleftharpoons Li + C_n^+A^- \quad (13)$$

The cell voltage is given by eqn (14),[130] where μ^0_{Li}, μ_{Li^+}, $\mu_{C_n^+A^-}$ and μ_{A^-} are chemical potentials of Li deposition onto Li foil, Li^+ in the electrolyte, A^- intercalation into carbon, and A^- in the electrolyte. In the dilute electrolyte limit, μ_{Li^+} and μ_{A^-} are given by the Nernst equation (eqn (15)), where μ^0, $[Li^+]$, $[A^-]$, k and T represent the chemical potential of the ions in a 1 M solution, Li^+ concentration, A^- concentration, a constant and temperature. Assuming a neutral electrolyte, the cell voltage is as given by eqn (16). Judging from the above equation, the anion intercalation potential is determined by anion type (Fig. 10), solvent system and electrolyte concentration. These factors are not presented in alkali metal cation (Li^+, Na^+, and K^+)-based batteries.

$$-eV = (\mu^0_{Li} - \mu_{Li^+}) + (\mu_{C_n^+A^-} - \mu_{A^-}) \quad (14)$$

$$\mu_{Li^+} = \mu^0_{Li^+} + kT\ln[Li^+] \text{ and } \mu_{A^-} = \mu^0_{A^-} + kT\ln[A^-] \quad (15)$$

$$-eV = \mu^0_{Li} + \mu_{C_n^+A^-} - \mu^0_{Li^+} - \mu^0_{A^-} - 2kT\ln[Li^+] \quad (16)$$

(1) Anion type effect on anion intercalation. HSO_4^- is the first anion that was intercalated into graphite. As early as 1840, a H_2SO_4-based GIC was prepared.[120] In 1938, Rüdorff and Hofmann[27] discovered HSO_4^- intercalation into graphite from a concentrated acid electrolyte and proposed the first "rocking-chair" battery with graphite functioning as both anode and cathode. However, the use of a concentrated acid raises safety concerns for practical applications. And the proposed dual-graphite batteries showed limited working voltage (<0.8 V).

PF_6^- has been the most frequently explored anion for graphitic carbon cathodes since 1989, when McCullough *et al.*[30] patented the first energy storage device based on a non-aqueous electrolyte and two carbonaceous electrodes. Owing to the high ionic conductivity and excellent electrochemical stability, $LiPF_6$ has been adopted as the state-of-the-art electrolyte for commercial LIBs. At high potentials, PF_6^- forms F-containing passivation films on the Al or stainless steel current collector,[177] suppressing unexpected side reactions. Dahn *et al.*[130] first conducted *in situ* XRD to study the PF_6^- intercalation process into the graphite lattice and proved that a variety of staged phases existed; they measured the

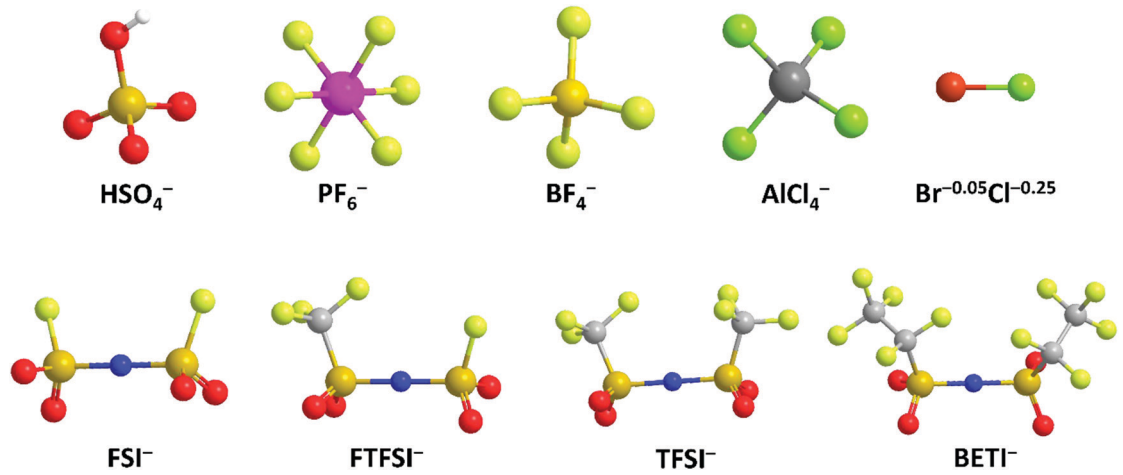

Fig. 10 Schematic structure of different anions.

average layer spacing and PF_6^--containing gallery height. A maximum stage-II' phase with a stoichiometry of $C_8(PF_6)_{0.5}$ was speculated, leading to a specific capacity of 140 mA h g^{-1} in the potential range of 3.5–5.45 V (*vs.* Li^+/Li). With the assistance of various *in situ* characterization techniques, Read *et al.*[129] investigated highly oriented pyrolytic graphite (HOPG) lattice expansion and revealed the solvent co-intercalation phenomenon during PF_6^- intercalation. Stage and composition progression of PF_6^--GICs was proposed as follows: $C_{24}PF_6$ (stage-IV) → $C_{24}PF_6$ (stage-III) → $C_{24}PF_6$ (stage-II) → $C_{20}PF_6$ (stage-II) → $C_{24}PF_6$ (stage-I) → $C_{20}PF_6$ (stage-I). The final $C_{20}PF_6$ (stage-I) GIC at 5.20 V (*vs.* Li^+/Li) corresponded to a specific capacity of 112 mA h g^{-1} and led to an expansion of 130%, as confirmed by *in situ* dilatometry measurements. Further, gravimetric measurements indicated that anion intercalation was accompanied by solvent co-intercalation at a ratio of ~0.7 ± 0.2 solvent molecules per PF_6^-. Recently, it was evidenced with electrochemical quartz crystal microbalance (EQCM) that ethyl methyl carbonate (EMC) participated in the PF_6^- intercalation/deintercalation process by repeated release/feedback from/to the graphite cathode.[164] To explore the molecular structure of PF_6^- in graphite, the DFT calculation was applied to simulate PF_6^- orientation between graphene sheets.[178] A periodic unit cell constructed by two layers of 24 graphitic carbons and one PF_6^- showed that PF_6^- had a tilted octahedral shape.

Besides, imide anions (bis(trifluoromethanesulfonyl)imide ($TFSI^-$), fluorosulfonyl-(trifluoromethanesulfonyl)imide ($FTFSI^-$) and bis(fluorosulfonyl)imide (FSI^-)) with better thermal/chemical stability and lower sensitivity towards hydrolysis than PF_6^- have been surveyed for graphitic carbon cathodes. Winter *et al.*[179] pioneered $TFSI^-$ intercalation research in ionic liquid (IL) electrolytes. The upper cut-off potential for $TFSI^-$ intercalation into graphite was optimized (4.8–5.1 V *vs.* Li^+/Li) to balance capacity and CE. The onset potential of $TFSI^-$ intercalation, especially in the first cycle, was dependent on temperature. Increasing the temperature (20 → 60 °C) resulted in an increased $TFSI^-$ uptake (30 → 100 mA h g^{-1}). However, the self-discharge rate of the $TFSI^-$-intercalated graphite cathode was also accelerated (1.3% per hour at 40 °C *vs.* 5% per hour at 60 °C). Further, after screening various graphite carbon cathodes, a maximum capacity of 115 mA h g^{-1} ($C_{19-20}TFSI$) was achieved.[180] *In situ* XRD was conducted to probe the structure evolution of the graphite cathode during $TFSI^-$ intercalation.[166,175] Stage-II and stage-I $TFSI^-$-GICs could be achieved at 20 °C and 60 °C, respectively. In spite of no solvent co-intercalation issue in the IL system, the calculated d_i of $TFSI^-$-intercalated graphite was in the range of 7.95–8.21 Å, which is higher than 7.77–7.83 Å for PF_6^--intercalated graphite[163] in a carbonate electrolyte. $FTFSI^-$ (3.9 × 6.5 Å), an imide anion with smaller size (3.9 × 6.5 Å) compared to $TFSI^-$ (3.9 × 8.0 Å), brought about higher capacities than $FTFSI^-$ at all surveyed upper cut-off potentials.[181] However, the CE is problematic due to the inferior electrochemical stability of $FTFSI^-$. The bis(pentafluoroethanesulfonyl) imide anion ($BETI^-$; 5.1 × 9.4 Å) was also investigated.[182] A high onset intercalation potential (5 V) and limited capacity (27 mA h g^{-1} at 3.4–5.6 V) were obtained, which can be mainly attributed to the large size of $BETI^-$. A more detailed investigation was carried out on the anion size effect on anion intercalation behavior in IL electrolytes. It was found that the onset potential for anion intercalation is in the sequence of $BETI^-$ > FSI^- > $FTFSI^-$ > (FSI^-/$TFSI^-$) > $TFSI^-$ > ($TFSI^-$/FSI^-), indicating that ion-pair formation and self-aggregation overrule the influence of the anion size on anion intercalation.[183] FSI^- anions were recently intercalated into the graphite cathode in a concentrated carbonate electrolyte, rather than in an IL.[167] The FSI^- intercalation was initialized at 4.6 V (*vs.* Li^+/Li) and reached a stage-I GIC at 5.25 V (*vs.* Li^+/Li). The maximum capacity achieved was 112 mA h g^{-1}, corresponding to a stoichiometry of $C_{20}(FSI)$. The d_i and Δc of stage-I FSI^--GIC are 7.83 Å and 134%, which are similar to those of PF_6^--GIC. Nevertheless, FSI^- intercalation into graphite suffers from gradually decreased CE (99% → 93% within 300 cycles), which can be ascribed to anodic etching problems faced by many imide electrolytes.[184,185]

BF_4^- with quite a small size (2.6 × 2.6 Å), low molecular weight, and high thermal and hydrolytic stability (compared to PF_6^-) was a promising anion candidate for the graphitic carbon cathode.[186] In the ethyl methyl sulfone electrolyte, BF_4^- intercalation occurs

above 4.83 V (*vs.* Li^+/Li), which is higher than 4.67 V for PF_6^- under the same condition.[166] In the potential range of 3.4–5.4 V, BF_4^- intercalation into graphite led to a capacity of 97.6 mA h g^{-1}, corresponding to a GIC stoichiometry of $C_{23}BF_4$. *In situ* XRD measurements further indicated a stage-I GIC and a d_i of 8.01 ± 0.05 Å. Although BF_4^- is smaller than PF_6^- in size, the d_i of BF_4^--GIC is higher than that of PF_6^--GIC, which can be explained by BF_4^- solvation states and solvent co-intercalation. In carbonate electrolytes (*e.g.* EMC) which work efficiently for PF_6^- intercalation into the graphite cathode, BF_4^- intercalation was found to be largely hindered with limited capacity (6 mA h g^{-1} at 3–5 V) yet high polarization over 1 V.[187] The strong attraction between Li^+ and BF_4^- clusters and the special anion solvation states were believed as the main reasons. By introducing the additional trimethyl phosphate solvent, Wang *et al.*[188] facilitated BF_4^- intercalation into graphite, leading to an enhanced capacity (26.7 mA h g^{-1}) and suppressed polarization (0.3–0.4 V).

Metal chlorides (*e.g.* UCl_5 and $AlCl_3$), as an important family of intercalants, were intercalated into graphite as early as 1973 by a solution method.[170] It was not until 2015 that electrochemical $AlCl_4^-$ intercalation into graphitic carbon was first accomplished by Dai and coworkers in an IL electrolyte composed of $AlCl_3$/1-ethyl-3-methylimidazolium chloride (EMImCl).[170] A 3D graphene foam cathode was used as the cathode and a capacity of 66 mA h g^{-1} was achieved. *Ex situ* XRD suggested the formation of a stage-IV $AlCl_4^-$-GIC under a fully charged state. A broad shoulder was noticed in the XRD pattern of the fully discharged sample, indicating irreversible change of stacking between graphene layers or trapped intercalants. *In situ* Raman spectroscopy revealed that, during $AlCl_4^-$ intercalation, the graphite G band at 1584 cm^{-1} diminished and split into a doublet (E_{2g2}(i) mode at 1587 cm^{-1} and E_{2g2}(b) mode at 1608 cm^{-1}), and eventually evolved into a sharp new peak at 1636 cm^{-1}. E_{2g2}(i) was attributed to vibrations of carbon atoms in the interior of graphite layer planes, while E_{2g2}(b) was derived from vibrations of carbon atoms in the bound graphite layers adjacent to intercalant layer planes. On replacing graphene foam by natural graphite, the capacity was largely enhanced to 110 mA h g^{-1}.[189] Reversible oxidation/reduction of carbon was verified by X-ray photoelectron spectroscopy (XPS) and X-ray adsorption spectroscopy (XAS). The geometry structure of $AlCl_4^-$ between graphene layers was further simulated by DFT and first-principles calculations. The four bond angles of $AlCl_4^-$ were changed to 107.8°, 106.8°, 110.1° and 107.6°. It means that $AlCl_4^-$ was distorted/flattened from the tetrahedron structure. Moreover, the temperature has a significant impact on the structure of the $AlCl_4^-$-GIC. It was found that at −10 °C, $AlCl_4^-$ intercalation into graphite led to a stage-III GIC, rather than a stage-IV GIC at room temperature.[168] At the same time, a new charge/discharge plateau was observed at 2.5 V (*vs.* $Al_2Cl_7^-/Al$) in the charge–discharge profiles of the graphite cathode. The d_i of stage-III $AlCl_4^-$-GIC was 9.59 Å, as indicated by theoretical modeling. $AlCl_4^-$ intercalation into graphitic carbon can additionally occur in inorganic ILs like $AlCl_3$–urea[190] and $AlCl_3$–NaCl–KCl (at 393 K).[191]

$$LiBr + C_n \rightleftharpoons C_nBr + Li^+ + e^- \quad (4.0–4.2\ V) \qquad (17)$$

$$LiCl + C_nBr \rightleftharpoons C_nBrCl + Li^+ + e^- \quad (4.2–4.5\ V) \qquad (18)$$

Different from the above complex anions that have no redox capability, redox-active halogen anions can also be electrochemically intercalated into graphite. Wang's group[172] recently prepared stage-I $Br^{-0.05}Cl^{-0.25}$-GIC within a "water-in-bisalt" electrolyte. A composite cathode containing LiBr, LiCl and graphite was applied. During the charging process, a new conversion–intercalation mechanism took place inside the composite cathode, where Br^- and Cl^- in LiBr and LiCl were converted into $Br^{-0.05}$ and $Cl^{-0.25}$ and intercalated into graphite. The two-step electrochemical reactions are represented by eqn (17) and (18). Due to the oxidation of Br^- and Cl^- and their low molecular mass, more electron transfer can be achieved. Furthermore, the slightly negatively charged $Br^{-0.05}$ and $Cl^{-0.25}$ would not cause strong Coulomb repulsion within the graphite host. The average nearest in-plane distance of halogen intercalants was 2.43 Å for Br–Cl1, which is much shorter than 4.3–4.92 Å for alkali-metal GICs and 8–10 Å for conventional anion-GICs. Therefore, a densely packed stage-I GIC, $C_{3.5}Br_{0.5}Cl_{0.5}$, and a high capacity of 243 mA h g^{-1} were achieved (based on the total mass of the composite electrode) at an average potential of 4.2 V *vs.* Li^+/Li. Note that the initial onset potential for Br^- intercalation was around 4 V, which is lower than >4.4 V *vs.* Li^+/Li for PF_6^-, $TFSI^-$ and FSI^-. As revealed by *in situ* XRD, the d_i of $C_{3.5}Br_{0.5}Cl_{0.5}$ was only 6.85 Å, which is much lower than those for complex anions (Table 3). It can be ascribed to the small size of BrCl and the absence of solvent co-intercalation. This unique halogen conversion–intercalation mechanism provides a new design principle for intercalation chemistry of layered materials.

(2) Solvent role in anion intercalation. Solvent, an important component of liquid electrolytes, plays a key role in dissolving active salts and offering a medium for charge carrier migration. The interaction between anions and solvent significantly influences anion intercalation behavior and therefore the electrochemical performance of graphitic carbons. An ideal electrolyte should possess a wide electrochemical stability window, high ionic conductivity, low viscosity, excellent thermal stability, low toxicity and ability to form a passivation film to prevent continuous electrolyte decomposition.[192–194]

Carbonate electrolytes have been frequently utilized for the graphitic carbon cathode due to their high dielectric constant, low viscosity, and excellent electrochemical stability.[195] Ethyl carbonate (EC), an important SEI forming agent for LIBs, largely prevents anions from intercalating into graphitic carbon[196] due to its strong solvation power against PF_6^-, which makes it difficult for PF_6^- to be de-solvated for intercalation. However, such strong solvation power of EC is necessary to dissolve salts with limited solubility or to achieve concentrated electrolytes. Therefore, EC is still used for $NaPF_6$,[178,197–199] KPF_6,[200,201] $Ca(PF_6)_2$[202] and KFSI[167]-based electrolytes. In these electrolytes, anion intercalation will be accompanied by EC co-intercalation. Lu with his colleagues[203] investigated the interaction between PF_6^- and different solvents, including EMC, dimethyl carbonate (DMC), EC, PC, 1,3-dioxolane (DOL) and dimethyl ether (DME). The van der Waals forces between

PF_6^- and DMC or EMC are positive while they are negative for PF_6^- with DME, DOL, EC and PC, indicating repulsion and attraction, respectively. Among these solvents, EMC is closest to the balance site, leading to the highest anion intercalation capacity in the range of 3–5 V *vs.* Li^+/Li. In PC solvent, the onset potential for PF_6^- intercalation moves to a higher value (4.7 V *vs.* Li^+/Li), which is higher than 4.4–4.5 V *vs.* Li^+/Li in EMC solvent and results from the strong interaction of PF_6^- with PC. Besides, it is found that DMC can lower the anion intercalation potential plateau, indicating enhanced intercalation kinetics.[202]

To further enhance the oxidative stability of carbonate electrolytes, F-containing carbonate is adopted due to its low highest occupied molecular orbital (HOMO) energy.[204,205] Moreover, F-containing carbonate can contribute to the formation of a F-rich interphase, which is beneficial for both cathode and anode. Read *et al.*[206] prepared an electrolyte of 1.7 M $LiPF_6$ in monofluoroethylene carbonate (FEC)–EMC with 5 mM tris(hexafluoro-isopropyl)phosphate. PF_6^- intercalation works efficiently in this electrolyte up to 5.2 V with a high average CE of 96%. It is worth noting that in carbonate electrolytes, solvent co-intercalation into graphitic carbon cathodes appears to be inevitable, but it does not necessarily cause graphitic carbon exfoliation as happened in the Li-PC[207] system for the graphite anode.

In addition, ILs with broad electrochemical stability windows, high safety properties (low volatility and low flammability), a broad liquid range and high thermal stability are attractive alternatives to carbonate solvents. As a typical example, $TFSI^-$, which severely corrodes Al current collectors in dilute carbonate electrolytes, however, performs stably up to 5.1 V (*vs.* Li^+/Li) in *N*-butyl-*N*-methylpyrrolidinium bis(trifluoromethanesulfonyl)imide ($Pyr_{14}TFSI$) with 1 M LiTFSI.[165,179] Good compatibility with Al current collectors was noticed for $BETI^-$, $FTFSI^-$ and $TFSI^-$ in ILs, which originates from the poor solubility of initially formed corrosion products in the ILs, thus generating a protective layer on the Al surface.[208,209] Regarding FSI-, as the products $[Al(FSI)_x]$ can be dissolved in IL, no protection layer can be formed, resulting in continuous Al etching.[210] Therefore, $BETI^-$, $FTFSI^-$ and $TFSI^-$ intercalation into graphitic carbon in IL electrolytes was quite efficient without obvious side reactions. Nevertheless, the high viscosity of ILs may be a concern for low ionic conductivity and limited intercalation kinetics compared to carbonate electrolytes, especially at low temperature ($\leq$RT). The salt solubility in ILs also seems to be limited ($\leq$1 M), making it difficult to prepare concentrated electrolytes.

(3) Electrolyte concentration effect on anion intercalation. Unlike in rocking-chair alkaline metal-ion batteries, electrolyte concentration has a profound effect on anion intercalation behavior. Within a Li//graphite cell, our group noticed that increasing $LiPF_6$ concentration (1 $\rightarrow$ 4 M) in EMC not only reduced the onset potential (4.45 $\rightarrow$ 4.25 V) of PF_6^- intercalation into graphite but also increased the specific capacity (67 $\rightarrow$ 98 mA h g^{-1}, Fig. 11), which can be explained by that under a high concentration electrolyte, most solvent molecules are coordinated/shared with/by adjacent cations and anions. This means that the solvent coordination number of anions decreases. Therefore, the desolvation energy of anions in a concentrated

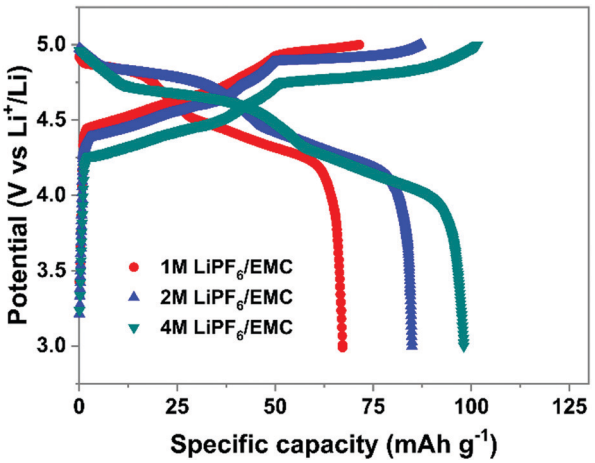

Fig. 11 Charge–discharge profiles of the graphite cathode in different concentration electrolytes. Li//graphite half cells were used. Electrolytes are 1–4 M $LiPF_6$ in EMC. The current density is 100 mA g^{-1}.

electrolyte is lower than that in a dilute electrolyte, leading to reduced anion intercalation potential. Similar phenomena were noticed in $LiPF_6$ FEC/DEC,[211] LiTFSI DMC,[212] $LiPF_6$ methyl propionate[213] and even $AlCl_3$-EMImCl[214] electrolytes.

On the other hand, high concentration electrolytes can enhance the reversibility of anion intercalation by suppressing side reactions (anodic dissolution/etching). The recently reported $Br^{-0.05}Cl^{-0.25}$-GIC[172] can only be prepared in a highly concentrated aqueous electrolyte; otherwise side reactions like water oxidation will take place and Br^- and Cl^- are impossible to intercalate into graphitic carbon. Another example is that the dilute LiTFSI carbonate electrolyte suffers from the Al etching problem, which was well resolved by increasing LITFSI concentration. A high oxidation stability of up to 5.6 V was obtained in 2.7 M LiTFSI/DEC,[212] which is attributed to the lack of free solvent molecules, thereby stabilizing the Al current collector.[215] The concentrated electrolyte strategy is kinetically effective to enhance the electrolyte oxidative stability, which performs well in rocking-chair batteries.[216,217] Because electrolyte concentration remain constant during battery operation. For graphitic carbon cathode working under the anion intercalation mechanism, it remains to be confirmed whether anodic etching will reappear once most salts are consumed during charging, especially under lean electrolyte conditions.

3.2.3 Anion intercalation kinetics. The intrinsic anion diffusivity into graphitic carbon is a key property that determines the rate capability of graphitic carbon cathodes. Ishihara *et al.*[218] measured apparent PF_6^- diffusivity in KS-6 graphite using the galvanostatic intermittent titration technique (GITT). The calculated diffusion coefficient of PF_6^- in graphite ranges from 6.2×10^{-14} to 1.5×10^{-11} cm^2 s^{-1} with the minimum values obtained during phase transition from stage-II to stage-I (Fig. 12a). Comparing diffusion coefficients in the same stage structure and considering experiment error, the authors concluded that the diffusion coefficient of PF_6^- is independent of electrolyte concentration. Besides, electrochemical impedance spectroscopy (EIS) measurements were also carried out which showed diffusion coefficients

of 1.18–7.7 × 10^{-13} cm^2 s^{-1} for electrolytes with different concentrations. These values are similar to those obtained from GITT. DFT further indicates a preferable ⟨100⟩ diffusion route for PF_6^- and a low theoretical activation energy of 0.23 eV (Fig. 12b). Compared with diffusion coefficients of Li^+ in $LiFePO_4$ (10^{-14} cm^2 s^{-1})[219] and $LiCoO_2$ (3×10^{-15} cm^2 s^{-1}),[220] the diffusivity of PF_6^- in graphitic carbon is high.

Our group investigated PF_6^- intercalation kinetics in graphite flakes by a CV method (Fig. 12c),[221] where a strong binder was used to address the electrode disintegration problem. Four main pairs of redox peaks corresponding to reversible formation of different stage PF_6^--GICs were clearly observed in the CV curves of the graphite cathode. The current increased along with the scan rate without generating much polarization (peak shift), behaving like pseudocapacitive materials. According to eqn (8),[222] the *b* values of each redox peak were estimated to be approaching 1, implying that PF_6^- intercalation into graphite is not a diffusion-limited process. The *b* value of the oxidation peak derived from phase transition (stage-II to stage-I) is found to be lower than others, suggesting relatively slow PF_6^- intercalation in this range. This result fits very well with diffusion coefficient data attained from GITT measurements. The capacitive contribution was quantitatively determined by eqn (9). At 1 mV s^{-1}, 93% capacity is from capacitive-like intercalation (Fig. 12d). Our results suggest that kinetically PF_6^- intercalation into graphite displays capacitor-like (pseudocapacitive) characteristics.

Winter *et al.*[223] conducted a comprehensive study on $TFSI^-$ intercalation kinetics into various graphitic carbons in IL electrolytes. The specific discharge capacity strongly depends on the "non-basal plane" surface area of graphite at <40 °C, which can be related to additional overpotential evolution close to the formation of intercalation stages of the graphite host. Due to large anion size, the diffusion coefficient (2 × 10^{-15} cm^2 s^{-1} at 20 °C, Fig. 12e) of $TFSI^-$ within the graphite lattice is lower than that for PF_6^-. At operating temperatures >50 °C, the capacity increases remarkably from 60 mA h g^{-1} to 100 mA h g^{-1} owing to the presence of stage-I GIC enabled by further overpotential reduction. With respect to $AlCl_4^-$, the energy barrier for $AlCl_4^-$ diffusion in graphitic carbon calculated using the NEB method is in the range of 0.021–0.028 eV,[224] much lower than 0.3–0.4 eV for Li diffusion in graphite.[225] Considering a large d_i of 9.25 Å for $AlCl_4^-$-GIC, Sun *et al.*[224] suggested a configuration with 3-fold rotation symmetry about the direction normal to the graphite basal plane, even though its energy is higher than that of the configuration with 2-fold rotation symmetry. Lu *et al.*[226] performed first-principles calculations on $AlCl_4^-$-GICs and revealed that $AlCl_4^-$ prefers single-layer tetrahedron geometry between graphene sheets with AB stacking manner preserved. Diffusion energy barriers of $AlCl_4^-$ were determined as 0.012–0.029 eV (Fig. 12f), leading to a high diffusion coefficient in the order of 10^{-4} cm^2 s^{-1} and fast $AlCl_4^-$ intercalation into graphitic carbon.

3.2.4 Effect of graphitic carbon characteristics on anion intercalation. As the host of anions, the structural features (graphitization degree, defect, crystal structure, morphology and so on) of graphitic carbon thermodynamically and kinetically affect the anion intercalation behavior (onset potential, voltage

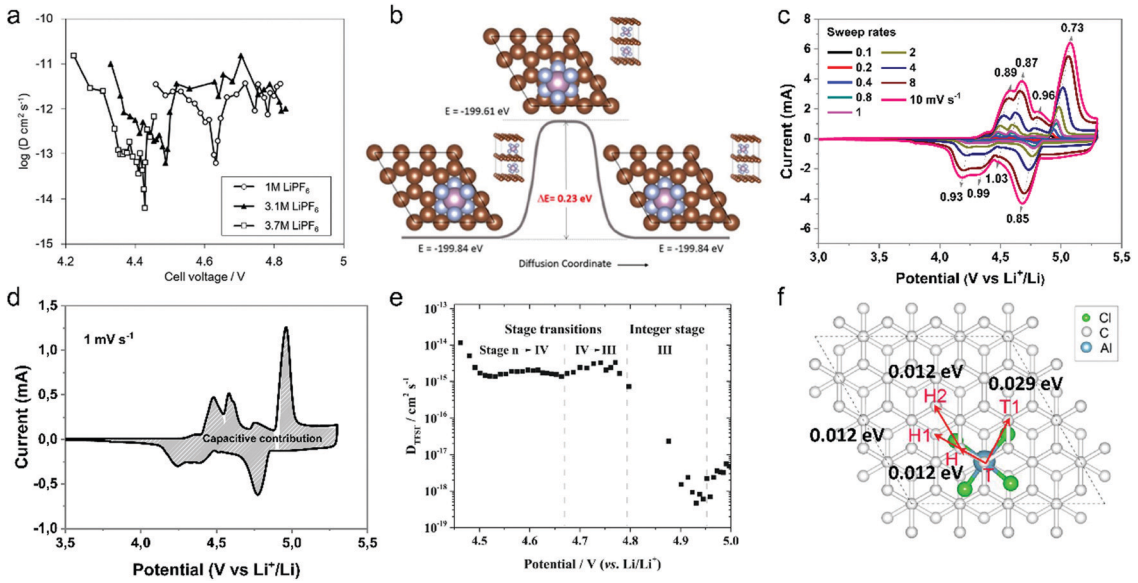

Fig. 12 (a) Diffusion coefficient of PF_6^- into graphitic carbon calculated using GITT as a function of cell voltage during the charging process. (b) The CI-NEB calculation result for estimating the diffusion energy barrier along the ⟨100⟩ direction. Reproduced from ref. 218 with permission from American Chemical Society. (c) CV curves of graphite cathodes at various sweep rates. (d) Separation of the capacitive and diffusion currents of the graphite cathode at a scan rate of 1 mV s^{-1}. Reproduced from ref. 221 with permission from Wiley-VCH. (e) Representation of the (apparent) diffusion coefficient of the TFSI anion in graphite in relation to the charging potential and estimated stage of the acceptor-type GIC. Working electrode: KS6 graphite; reference/counter electrodes: lithium metal; 2nd cycle, operating temperature 20 °C. Reproduced from ref. 223 with permission from Elsevier. (f) Four elementary diffusion pathways for $AlCl_4^-$ in the graphite denoted by arrows connecting two sites. Reproduced from ref. 226 with permission from American Chemical Society.

efficiency, reversible capacity and rate capability). These factors will be analyzed in detail to provide a general understanding of anion intercalation.

The first key parameter for graphitic carbons is graphitization degree (GD), which is defined as the extent of the transformation of nongraphitic carbon materials into a perfectly ordered graphitic structure, can be expressed by eqn (19),[227] where 0.3440 nm and 0.3354 nm are the interlayer spacing of non-graphitic carbon and perfectly stacked graphite, respectively. d_{002} is the interlayer spacing of the studied carbon materials. Ishihara *et al.*[228] conducted electrochemical PF_6^- intercalation experiments on various carbon materials, and noticed that the capacity of PF_6^- intercalation increases with decreasing d_{002} (enhancing GD). To further reveal the structure–electrochemical property correlation, a detailed investigation was carried out on carbon materials with controlled GD. Under a high temperature treatment (2200–2800 °C), non-graphitic carbons gradually evolve into graphitic ones with d_{002} decreased from >0.3415 nm to 0.3360 nm while GD enhanced from 30% to 90%.[229] It was found that the electrochemical performance of the carbon cathode is directly dependent on the GD, where the specific capacity increases along with GD at a rate of ~0.3 mA h g^{-1} per GD and a maximum discharge capacity of 100 mA h g^{-1} was achieved in a LiTFSI/IL electrolyte. The voltage efficiency was found to be improved in the carbon cathode with a high GD. For $AlCl_4^-$, a similar phenomenon was recognized. Kish graphite flakes with the smallest d_{002} showed a typical staging intercalation/deintercalation process and the highest capacity, while the amorphous carbon presents a linear charge–discharge curve and the lowest capacity.[230]

$$\mathrm{GD}\ (\%) = \frac{0.3440 - d_{002}}{0.3440 - 0.3354} \times 100 \qquad (19)$$

As mentioned earlier, heteroatom-doping/defect engineering is an efficient strategy to modulate the electronic structure and physicochemical characteristics of carbon materials, especially for electrochemical catalysis[231] and alkali metal-ion storage.[232,233] The current results indicate that O dopants and defects appear to be detrimental for anion storage. The O dopants will influence the delocalized π electronic structure of graphitic carbon and deteriorate the conductivity. For instance, reduced graphene oxide aerogel containing considerable oxygen dopants exhibited a limited capacity of <10 mA h g^{-1} for $AlCl_4^-$ storage. In sharp contrast, the defect-free graphene aerogel prepared after the annealing process at 3000 °C delivered a high capacity of 100 mA h g^{-1} and a high discharge voltage of 1.95 V.[234] Fast charging within several seconds was reported as well on this graphene aerogel cathode, which was attributed to the defect-free structure and fast $AlCl_4^-$ intercalation. Few-layer graphene with few defects can be alternatively prepared by an electrochemical exfoliation method using Co^{2+} as the antioxidant.[235] The oxygen content was suppressed to as low as <3% and a bulk conductivity of 29 800 S m^{-1} was obtained. As a result, the few-layer graphene enabled both PF_6^- and $AlCl_4^-$ intercalation for DIBs and AIBs, achieving high capacity over >120 mA h g^{-1} even at a high rate.[230] More investigation is required to confirm the effect of other dopants (like B, N, P) on anion intercalation behavior in graphitic carbon.

Particle size is another important parameter for graphitic carbon, where two different planes, basal plane and edge plane, exist. The smaller the size, the more the edge plane exposed. Considering the "entrance" feature of the edge plane for guest ion intercalation, more edge exposure indicates a short diffusion path and a fast intercalation rate, leading to high capacity and rate capability as evidenced by the graphite anode for LIBs.[236] For the anion intercalation process, the graphite particle size effect was studied in $TFSI^-$-based IL electrolytes.[180,237] Small-size graphite indeed exhibited higher capacity at 20 °C, even though the electrode conductivity decreased with particle size due to the increased number of high-resistance particle surface contacts.[238] However, this effect gradually blurred at 60 °C, which is explained by the fact that the enhanced ion diffusion at elevated temperature prevails the effect of entrance sites present at low temperature. In addition, the irreversible charge capacity of the graphite cathode in the first cycle was found to be independent of graphite size (surface area), which is different from the SEI formation process for the graphite anode.[239] No correlation between the first cycle efficiency and the particle size (specific surface area) of graphitic carbon could be concluded. The anion intercalation stability was proved to be better in large-size graphitic carbon (graphite, graphene) than small-size one.[238,240]

The thickness of graphitic carbon with a compact stacking structure can be tailored by exfoliation or introducing pores between graphitic carbon layers. Thin graphitic carbon is expected to possess enhanced ion diffusion and to better alleviate volume expansion. It is reported that the few-layer graphene cathode exhibited a much higher rate than the graphite counterpart for $AlCl_4^-$ intercalation/deintercalation.[240] To facilitate fast $AlCl_4^-$ diffusion inside graphitic carbon, vertically aligned pores were introduced into compact pyrolytic graphite foil *via* $AlCl_4^-$ intercalation followed by thermal expansion and electrochemical H_2 expansion (Fig. 13a),[97] avoiding irreversible oxidation of graphite and defect introduction. The resultant monolithic vertically aligned graphitic structure afforded complete $AlCl_4^-$ intercalation within 18 s (60 mA h g^{-1} at 12 A g^{-1}) and remained stable for over 4000 intercalation–deintercalation cycles.

Besides, the morphology of graphitic carbon also plays a critical role in anion intercalation. The exposure state (well exposed or blocked) of the edge plane and basal plane (bent or not) of graphitic carbon may influence the anion intercalation behavior. The comparison between potato-like graphite particles and graphite flakes indicates that potato-like graphite with bent graphene layers showed a reduced ability for $AlCl_4^-$ intercalation (65 mA h g^{-1} *vs.* 95 mA h g^{-1} for graphite flakes),[230] which is different from the Li^+ intercalation case. Three-dimensional graphene foam that was made *via* chemical vapor deposition possessed well interconnected pores and led to a maximum capacity of 70 mA h g^{-1}.[170] The graphene foam cathode enabled fast yet durable $AlCl_4^-$ intercalation/deintercalation, affording a charge time of 1 minute and stability over 7500 cycles. Recently,

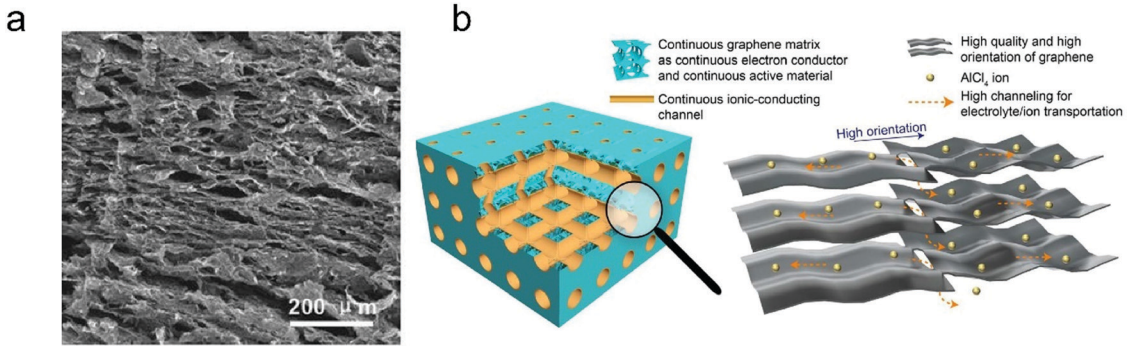

Fig. 13 (a) The SEM image of three-dimensional graphite foam. Reproduced from ref. 97 with permission from Wiley-VCH. (b) Illustration of tri-continuous and tri-high design for a desired graphene film. Reproduced from ref. 169 with permission from AAAS.

a thin graphene film was reported as a high-rate anion intercalation host, which possessed high-quality, high-orientation graphene and a high channeling local structure as well as a continuous electrically conductive/electrochemically active matrix and ion-conducting channels (Fig. 13b).[169] The graphene film delivered a high capacity of 120 mA h g^{-1} (stage-III $AlCl_4^-$-GIC) at an ultrahigh current density of 400 A g^{-1} and a long cycle life of 0.25 million cycles.

4. Energy storage devices based on ion-intercalative carbon

4.1 Cation-intercalation carbon anode for 'rocking-chair' batteries

In this part, we mainly survey the recent developments in the structure design/modification of carbon-based materials, and the emerging battery devices based on these carbon materials. It should be pointed out that most of the research about carbon anodes focused on the correlation between microstructure and charge-storage performance, which mainly relies on the half-cell tests rather than implantation in full-cell devices. Therefore, particular efforts have been put on emerging carbon structures by associating their morphological properties with their electrochemical behavior.

4.1.1 Carbon anodes for LIBs

(1) Ordered carbon anodes. In spite of the great success of graphite anodes in commercial LIBs, the prospect of carbon anodes in LIBs is still obstructed in terms of the lower theoretical capacity of graphite compared with other conversion- or alloy-type anodes (*e.g.* silicon, Sn, transition metal oxides/dichalcogenides).[36] In this context, extensive efforts have been devoted to constructing fantastic carbon structures with favorable metrics, such as high specific surface area, hierarchical porosity, and doping with heteroatoms/functional groups.

The early studies on Li-ion storage carbon anodes mainly focused on ordered carbon materials, which have been well documented in some previous review literature.[37,242–244] Most of the studies rely on constructing hierarchical structures with ordered carbon building blocks (*e.g.* 2D graphene, 1D CNTs) to achieve high specific capacity, as such kind of structures promote the access of the electrode surface to the electrolyte.[245–255] For example, graphene was employed early to construct a binder-free anode for LIBs by directly drop-casting the graphene ink on Cu foil.[256] Hassoun *et al.*[257] reported full LIBs with graphene anodes and lithium ion phosphate cathodes delivering a high specific capacity of 165 mA h g^{-1} and an energy density of 190 W h kg^{-1}. On the other hand, the ion mobility of 2D materials is considered as the key factor that limits their rate performance.[258] To improve the compact geometry of carbon materials and enhance their accessible volume, creating ordered pores was also widely investigated. For example, Zhao and co-authors[251] prepared a kind of mesoporous graphene nanosheet through controllable assembly of monomicelles and heterogeneous nucleation processes. Phenolic resol molecules were assembled with a Pluronic triblock copolymer, forming spherical monomicelles and depositing on the channel walls of an anodic aluminum film. After pyrolysis at 700 °C for 2 h in argon, the mesoporous graphene nanosheets were synthesized. The mesoporous graphene nanosheets exhibited a low coulombic efficiency of 29.4% in the first cycle, with a discharge specific capacity of 3535 mA h g^{-1} and a charge specific capacity of 1040 mA h g^{-1} at 100 mA g^{-1}. In 2010, our group designed a kind of graphene-based mesoporous nanosheet with a sandwich structure.[241] As shown in Fig. 14a, graphene-based mesoporous silica sheets were synthesized by using negatively charged graphene oxide to electrostatically adsorb cationic cetyltrimethyl ammonium bromide and annealing in Ar at 800 °C for 3 h. The graphene-based mesoporous nanosheets were further synthesized by using graphene-based silica sheets as the templates and sucrose as the carbon source. The SEM image (Fig. 14b) revealed the 2D morphology of the graphene-based mesoporous carbon materials. The specific surface area was measured to be 910 m^2 g^{-1} with the presence of abundant micro- and meso-pores (Fig. 14c). The first-cycle reversible capacity of this graphene-based mesoporous carbon nanosheet reached up to 915 mA h g^{-1} (Fig. 14d).

Besides, vertically aligned MWCNT arrays were obtained on various catalytic substrates (*e.g.* graphene paper,[249] stainless steel,[250] copper,[245] nickel foil,[254] silicon[252]) through CVD methods. The reversible specific capacity at a low rate ranged from 350 to 1455 mA h g^{-1}. For example, Li *et al.*[249] fabricated a novel kind of free-standing graphene paper with vertically

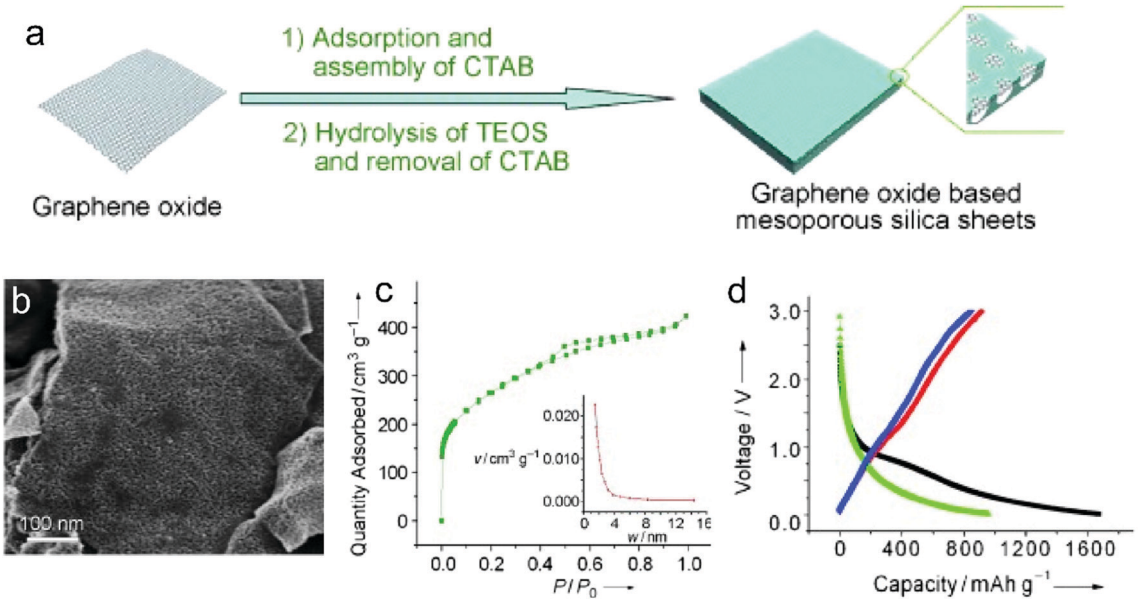

Fig. 14 (a) Schematic of the formation process for graphene oxide based mesoporous silica sheets. (b) SEM and (c) nitrogen adsorption/desorption isotherm of the obtained graphene-based mesoporous nanosheets. (d) First and second cycles of galvanostatic discharge/charge curves of the graphene-based mesoporous nanosheets. Reproduced from ref. 241 with permission from Wiley-VCH.

aligned MWCNTs grown on the surface. A reversible capacity of 290 mA h g^{-1} at 30 mA g^{-1} was reached. By using a similar two-step process, Choi's group[245] grew MWCNT arrays on a copper current collector through a two-step process of sputtering catalytic Ti and Ni on Cu foil and MWCNT growth by a CVD method. At a low current density of 38 mA g^{-1}, the first discharge and charge capacity of the obtained electrode were 2500 and 1455 mA h g^{-1}, indicating the first-cycle CE of 58%. Even at a very large current density of 1116 mA g^{-1}, the reversible specific capacity of the vertical aligned MWCNT arrays reached 767 mA h g^{-1}.

(2) Disordered carbon anodes. Developing disordered carbon materials by searching suitable carbon-rich precursors represents another important development trend in high-capacity carbon anode materials.[260] In this research direction, the employed precursors play a crucial role in determining the structural properties of hard carbon materials. So far, the employed precursors mainly include biomass (*e.g.* egg white,[261] sheep bone,[262] Portobello mushroom,[263] filter paper[264,265]) and synthetic carbon-rich compounds (zeolitic imidazolate framework-8,[266] ethylenediaminetetraacetic acid manganese disodium salt hydrate,[267] alkyl surfactant sulfonate anion-intercalated NiAl-layered double hydroxide,[268] polyacrylonitrile (PAN),[259,269–272] phenol resin,[273,274] and hexa-*peri*-hexabenzocoronene[275]). One of the targets for these studies is to find green and low-cost precursors for large-scale production of hard carbon materials with a high specific surface area. For example, electrospun PAN based nanosized fibers were widely used as carbon precursors. Kim *et al.*[270] directly used pure PAN fibers as the precursor to get carbon nanofibers for the LIB anode. As revealed, the carbon fibers obtained at 1000 °C depict an optimal reversible specific capacity of 450 mA h g^{-1} at 100 mA g^{-1}, outclassing the carbon fibers obtained at 700 °C (300 mA h g^{-1}) and 2800 °C (130 mA h g^{-1}).[270] To create porosity in the carbon fibers, poly(methyl methacrylate)[259,271] and poly-L-lactic acid[272] were added into the PAN based fiber precursor. During the thermal decomposition, poly(methyl methacrylate) or poly-L-lactic acid can produce a complex gas as the soft template, which induces the massive formation of large pores.

Apart from the direct pyrolysis of organic precursors for hard carbon materials, additional templates (*e.g.* $ZnCl_2$ salt,[276,277] SiO_2,[274,278,279] MgO,[280] Ni[259]) were also widely used to create more mass transport channels, which can significantly boost the specific capacity and rate capability of hard carbon materials. For example, our group demonstrated a kind of hollow carbon sphere by using hexadodecyl-substituted hexa-*peri*-hexabenzocoronene (HBC-C12) as the precursor and eyelike silica/space/mesoporous silica as the template.[275] The template was mixed with the tetrahydrofuran solution of HBC-C12 to allow the impregnation of HBC-C12 into the pores of the template. Afterwards, the samples were annealed in Ar at 700 °C for 5 h. After etching of silica in a NaOH solution, hollow carbon spheres were obtained, showing a specific surface area of 260 m^2 g^{-1}. Remarkably, the reversible specific capacity of the hollow carbon spheres reached 600 mA h g^{-1}. In addition, Chen *et al.*[259] first prepared PAN/$Ni(Ac)_2$/poly(methyl methacrylate) composite nanofibers by employing a coaxial electrospinning approach. The pyrolysis of these nanofibers was conducted at 700 °C under a vacuum of around −750 torr for 6 hours. During the pyrolysis, the strong stress induced by the vacuum condition cracked the graphitic layer, guiding the diffusion of Ni to the carbon fiber surface (as revealed in Fig. 15a). After the removal of Ni, the porous carbon fibers were obtained, featuring rich hollow tunnels (Fig. 15b). The Brunauer–Emmett–Teller (BET) results confirm the important role

of poly(methyl methacrylate) in producing pores with diameters of 3.2, 9, 25, and 40 nm (Fig. 15c). Meanwhile, the removal of Ni particles further increases the number of pores with a size of ~63 and 120 nm. Interestingly, the porous carbon nanofibers demonstrated excellent Li-ion storage performance with a high reversible capacity of 1560 mA h g^{-1} (corresponding to a volumetric capacity of 1.8 A h cm^{-3}) at 100 mA g^{-1} (Fig. 15d). At a large current of 10 A g^{-1}, the reversible specific capacity of the porous carbon nanofibers remained at 380 mA h g^{-1} (Fig. 15e). Moreover, the porous carbon nanofibers show excellent cycling stability with a slight capacity decay after 2000 charge/discharge cycles at 10 A g^{-1} (Fig. 15f).

(3) Heteroatom-doped carbon anodes. In addition, heteroatom doping represents an important strategy for further boosting the Li-ion storage ability of carbon anodes. It can induce the formation of topological defects in carbonaceous materials, which is beneficial for the diffusion and insertion of Li-ions into carbon structures. N-Doping has been the most common method, which was initially studied in ordered carbon materials (graphene[52,266,281–285] and CNTs[286]). Cao *et al.*[281] performed first-principles calculations to evaluate the Li-ion storage properties of different N-doped graphene, including graphitic, pyridinic and pyrrolic N-doped graphene. They demonstrated that the adsorption of Li^+ on pyridinic N-doped graphene was the most stable one among the three kinds of graphene, while graphitic N-doped graphene was the least stable one. The calculated specific capacity of pyridinic N-doped graphene can be up to 1262 mA h g^{-1}. Ajayan's group[52] synthesized N-doped graphene films through a CVD method with acetonitrile as the precursor. Compared with the pure graphene film, the N-doped graphene films demonstrated a 1-fold increase in their reversible capacity. The authors assigned the enhanced capacity to the enriched topological defects induced by the doped N atoms, which promote the Li intercalation properties. Moreover, high-level N doping can be realized by thermally treated carbon materials together with additional N resources, such as melamine[282,284,285] and ammonia.[283] For example, Cai *et al.*[282] mixed pristine graphene with melamine together, and thermally treated the mixture at a temperature of 700 °C under an Ar atmosphere. The N-doping level in the obtained N-doped graphene reached more than 7%, which endowed the N-doped graphene anode with a high reversible capacity of 1123 mA h g^{-1} at 50 mA g^{-1} and 241 mA h g^{-1} at 2 A g^{-1}. On the other hand, N-doped disordered carbon materials can be easily obtained by selecting N-containing precursors. These precursors can be N-containing polymers,[259,287–289] metal–organic frameworks,[266] and biomass.[278,290]

Heteroatoms, like P and S, were also doped into carbon materials to boost the Li-ion storage ability. Different from the N atom having a similar diameter to the C atom, P and S atoms have much larger diameters than the C atom.[291] Therefore, P and S dopants can expand the distance between the neighbor carbon layers, thus promoting the migration of Li ions within carbon materials. Hou's group[292] carried out the first study of P-doped graphene for Li-ion storage. They synthesized P-doped graphene by thermally annealing the mixture of graphite oxide and triphenylphosphine under an Ar atmosphere. As revealed, the specific capacity of P-doped graphene (460 mA h g^{-1} at 100 mA g^{-1}) greatly outweighed that of pure graphene (280 mA h g^{-1} at 100 mA g^{-1}). Zhang *et al.*[268] reported the synthesis of S-doped mesoporous carbon materials by the pyrolysis of alkyl surfactant sulfonate anion-intercalated NiAl-layered double hydroxide. The reversible specific capacity of the obtained S-doped mesoporous carbon reached an outstanding value of 1157 mA h g^{-1} at 100 mA g^{-1}. Moreover, to reach a synergistic effect, researchers also fabricated dual-doped carbon materials, like N,S-codoped and N,P-codoped carbon materials.[293–296] These materials all show great potential as large-capacity and highly stable anode materials for LIBs.

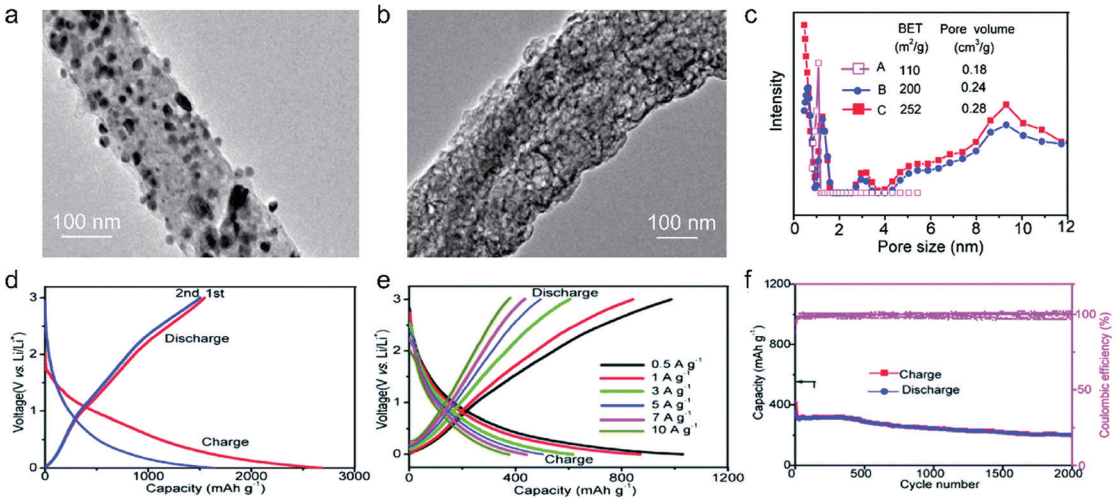

Fig. 15 TEM images of (a) N-doped carbon/Ni nanofiber and (b) porous N-doped carbon nanofiber. (c) Pore size distribution of sample A by calcining PAN/$Ni(Ac)_2$ composite nanofibers, sample B by calcining PAN/PMMA/$Ni(Ac)_2$ composite nanofibers, and sample C from sample B after Ni diffusion. (d) Initial two charge–discharge voltage profiles of the obtained porous carbon nanofibers cycled at a current density of 100 mA g^{-1}. (e) Charge–discharge profiles at various rates from 500 mA g^{-1} to 10 A g^{-1}. (f) Cycling performance at a current density of 10 A g^{-1}. Reproduced from ref. 259 with permission from Royal Society of Chemistry.

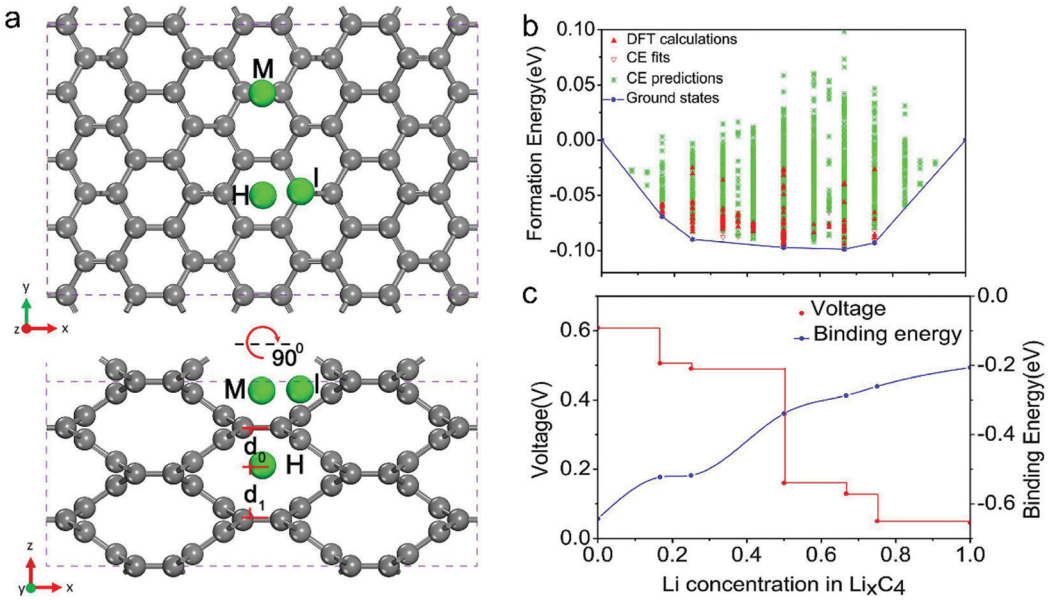

Fig. 16 (a) Structure of bco-C_{16} and the schematics of the possible Li-ion absorption sites in top and side view. (b) Formation energies predicted for the 150 different Li configurations with 5 stable intermediate phases. (c) Corresponding voltage profile (marked in red) and binding energy profile (marked in blue) calculated along the minimum energy path. Reproduced from ref. 298 with permission from United States National Academy of Sciences.

(4) Others. To go beyond the well-known ordered and disordered carbon structures, theoretical calculations were performed to predict the brand-new carbon structures for Li-ion storage. In 2016, Wang *et al.*[297] predicted a topological semimetal all-sp^2 bonding carbon structure consisting of a 16-atom body-centered orthorhombic unit cell (defined as bco-C16). The configuration of bco-C16 can be considered as a three-dimensional modification of graphite in AA stacking, which is made up of linear chains of benzene linked by ethene-type planar π-conjugation. Liu with his colleagues[298] used DFT calculations to identify the favorable Li-ion storage capability (558 mA h g^{-1}) of bco-C60 with a feasible Li-intercalated compound (LiC_4). Fig. 16a shows the possible Li-ion storage sites for bco-C16. Five stable intermediate configurations were simulated, corresponding to Li_xC_4 (x = 0.167, 0.25, 0.5, 0.667, and 0.75). The binding energies calculated for all these five intermediates are negative, revealing that Li ions can be stably stored in the bco-C16 structure (Fig. 16b and c). The simulated voltage profile reveals three main voltage platforms within the voltage range of 0.63–0.05 V and an average voltage of 0.25 V. Recently, Wang *et al.*[299] simulated a new 2D planar carbon allotrope, made up of 5-8-5 carbon rings. They revealed that such a structure principally depicts a high Li-ion adsorption capacity of 1487 mA h g^{-1} (Li_4C_6), a low open circuit voltage of 0.45 V, and a low Li-ion diffusion energy barrier (less than 0.55 eV). All these theoretical efforts provide an insightful understanding to further stimulate the design and synthesis of new carbon structures for Li-ion storage.

4.1.2 Carbon anodes for NIBs

(1) Ordered carbon anodes. As stated earlier, pristine graphite closes the door for Na-ion storage, owing to the difficult Na^+ intercalation into carbon bilayers. Considering the open structure and good electronic conductivity, graphene-based materials as NIB anodes attracted researchers' interest.[149,151,300–304] Wang *et al.*[151] synthesized rGO and studied its Na-ion storage capability in an electrolyte of 1 M $NaClO_4$ in PC. Compared with graphite materials, rGO presents a larger interlayer distance (0.36–0.37 nm) and a more disordered structure, which favors the intercalation of Na^+ into rGO. The specific capacity of rGO reached 174.3 and 93.3 mA h g^{-1} at 40 and 200 mA g^{-1}, respectively. David and Singh[300] investigated the NIB anodes made up of thermally reduced GO. rGO based materials annealed under an Ar atmosphere showed the optimal Na-ion storage performance at a thermal treatment temperature of 500 °C. The specific capacity reached 140 mA h g^{-1} at a current density of 100 mA g^{-1}. When the thermal treatment temperature was above 500 °C, the obtained rGO anodes exhibited an apparent capacity decrease. The authors attributed this capacity decay to the decreased interlayer spacing and the increased ordering level of the graphene sheets. Chang's group[301] synthesized a holey graphene material by thermally reducing GO at a low temperature of 300 °C with a fast temperature increase rate (>100 °C s^{-1}). The resultant rGO allowed the retention of oxygen-containing functional groups on the graphene surface, which not only provided additional redox sites but also expanded the interlayer spacing. For comparison, the rGO sample was also fabricated at a high temperature of 1000 °C. Clearly, the rGO electrode prepared under 300 °C (220 mA h g^{-1} at 30 mA g^{-1}) delivered a significantly higher specific capacity than the rGO electrode prepared under 1000 °C (147 mA h g^{-1} at 30 mA g^{-1}). Moreover, improvement in the Na-ion storage ability of graphene materials was also demonstrated by strategies like hydrogenation,[302] constructing crumpled morphology[304] and 3D foams.[305] The improved performance can be explained by the increased accessible surface area, the improved conductivity, and the favorable Na^+ diffusion.

(2) Disordered carbon anodes. Although graphene materials achieved great improvement in the ability of storing Na^+, particularly when compared with graphite materials, the limited specific capacity of graphene-based anodes still cannot fulfill the increasing capacity demand for SIBs. Following the developing roadmap of carbon-based LIB anodes, the development of new carbon structures for NIB anodes has been recently focused on the exploration of large-capacity disordered carbon materials. Synthesizing hard carbon materials from biomass materials is extremely attractive, as most of biomass materials are abundant, low-cost, and renewable. Typically, biomass derived carbon materials were fabricated by directly annealing pre-dried biomass materials under an inert atmosphere at high temperature. Gases (*e.g.* CO, C_2O, H_2O) would be produced during the pyrolysis, producing large amounts of micro- and meso-pores in the obtained carbon materials. Meanwhile, the impurities in biomass materials function as cross-linking agents, restraining the graphitization level of the obtained hard carbon materials. These features make biomass derived carbon particularly suitable for Na^+ storage. So far, numerous biomass materials have been explored, including peat moss,[306] banana peel,[307] peanut shell,[308] coconut oil,[309] cotton,[310] garlic peel,[311] wood,[312] apple,[313] cellulose,[314,315] okara,[316] leaf,[317] argan shell,[318] pistachio shell,[319] shrimp skin,[320] mangosteen shell,[321] artemia cyst shell,[322] and macadamia shell.[323] Mitilin's group[306] reported a kind of carbon nanosheet framework derived from peat moss. The obtained carbon nanosheet frameworks well inherited the cellular structure of peat moss leaves, showing the unique morphology of 3D interconnected nanosheet networks. The highly crosslinking, abundant hemicellulose and lignin in the peat moss structure effectively suppressed the graphitization ordering during the pyrolysis, which induced a highly ordered pseudographitic structure with a large interlayer spacing of 0.39 nm. The optimal sample was obtained by a combination of carbonization in Ar at 1100 °C and activation in air at 300 °C, showing a stable specific capacity of 298 mA h g^{-1} at 50 mA g^{-1}. Using almost the same method, this group further prepared interesting carbon materials with a banana peel precursor.[307] The stable specific capacity of the derived carbon anodes reached 355 mA h g^{-1} at 50 mA g^{-1}. In 2016, Yang *et al.*[316] reported the synthesis of carbon sheets with okara as the precursor (Fig. 17a). The dried okara was first hydrothermally treated in dilute sulfuric acid at 180 °C to remove the impurities and then annealed in a N_2 atmosphere at 500–900 °C for 2 hours. Afterwards, modified Hummers' method was further employed to expand and exfoliate the graphitic layers. The reversible specific capacity of the obtained carbon sheets reached 302.1 and 32.3 mA h g^{-1} at 56 mA g^{-1} and 11.25 A g^{-1}, respectively (Fig. 17b). Remarkably, the carbon sheets demonstrated an ultrastable Na-ion storage performance with no capacity decay after 2000 cycles at 1.68 A g^{-1}. The carbon sheets were further subjected to assemble a Na-ion full cell with $Na_3V_2(PO_4)_3$ cathodes. As shown in Fig. 17c, the full cell device delivered a stable capacity of 103 mA h g^{-1} at 562 mA g^{-1} with a voltage window of 0.3–4.2 V. Moreover, cotton[310] and wood[312] were carbonized at a temperature more than 1000 °C and directly used as the anode for SIBs. Both derived carbon materials showed a pseudographitic structure with rich short-range graphitic domains, which allowed a good reversible specific capacity around 300 mA h g^{-1} at low current densities and a high first-cycle CE (more than 70%). These features enable the practical application of those low-cost carbon anodes in assembling Na-ion full-cell devices.

Synthetic carbon-rich compounds are another category of precursors for synthesizing hard carbon materials.[324] Most of these materials are polymers, like polyvinyl chloride,[325] polyaniline,[326–328] polyamic acid,[329] and PAN.[330,331] Wang *et al.*[329] used an electrospinning technique to fabricate a thin film composed of polyamic acid nanofibers. The carbon film, obtained by direct carbonization at a temperature of 650 °C for 3 hours, was capable of delivering a reversible specific capacity of 377 mA h g^{-1}. Tarascon's group[330] fabricated a series of hard carbon materials by the pyrolysis of electrospun PAN nanofibers at temperatures ranging from 650 to 2800 °C. They revealed the Na-ion storage ability of the obtained hard carbon strongly depending on the different features induced by the pyrolysis temperature. With a low pyrolysis temperature (<1000 °C), the derived carbon materials contained numerous heteroatoms (including O, N). Heteroatoms were gradually removed when the pyrolysis temperature was above 1000 °C; meanwhile the increase of the ordered structure and mesoporous volume was demonstrated. Importantly, when the pyrolysis temperature reached more than 2000 °C, high-density graphite domains were observed, accompanied by the formation of rich pores surrounded by graphite layers. Meanwhile, the voltage curve of the derived carbon showed a clear single plateau at around 0.1 V, corresponding to a reversible capacity of 200 mA h g^{-1}. The authors verified that such a plateau was associated with the filling of nanopores by Na^+. Recently, Chen *et al.*[331] used a similar electro-spinning method to achieve PAN/$Zn(Ac)_2$/$Co(Ac)_2$ nanofiber networks. The obtained fiber was subsequently immersed in 2-methylimidazole solution, allowing the growth of Zn–Co bimetallic zeolitic imidazolate frameworks onto the nanofibers. Afterwards, the nanofibers were carbonized at 700 °C for 20 hours and washed with acid, affording the flexible free-standing film made of N-doped porous carbon nanofibers (Fig. 18a). As depicted in Fig. 18b, the obtained carbon nanofibers have a rough surface and a characteristic tubular structure with a diameter of 170–190 nm. Such a morphology is beneficial for the access of the carbon surface to the electrolyte and for the efficient transportation of electrolyte ions. The high-resolution TEM image (Fig. 18c) shows a large interlayer spacing of 0.38–0.44 nm, significantly outclassing the interlayer spacing of typical graphite. Moreover, the derived carbon nanofibers showed a high specific surface area of 438 m^2 g^{-1} and rich micro-pores (diameter of 0.6 and 1.5 nm) and meso-pores (diameter of 3.5 nm) (Fig. 18d). The first-cycle discharge capacity and charge capacity of the obtained carbon nanofibers were measured to be 346 and 735 mA h g^{-1} at 120 mA g^{-1}, respectively, corresponding to a first-cycle CE of 47.1% (Fig. 18e). The excellent rate capability and cycling stability of the carbon nanofibers were further evidenced by the high reversible capacity of 128 mA h g^{-1} at a large current density of 7 A g^{-1} and no clear capacity decay after cycling at 4.5 A g^{-1} for

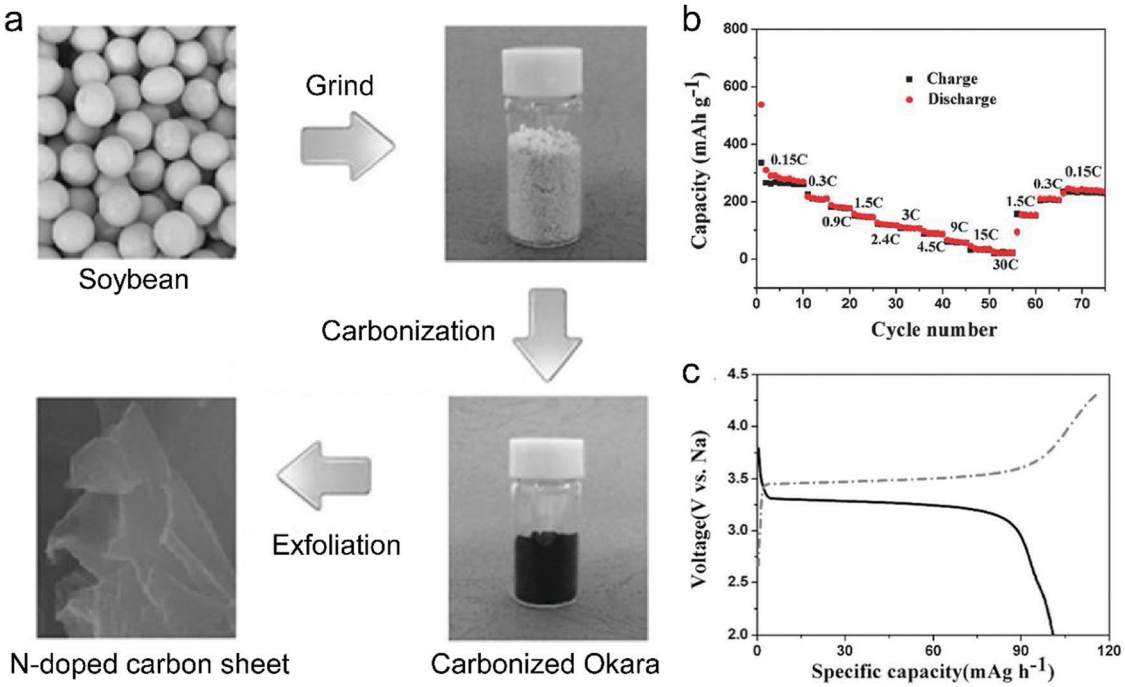

Fig. 17 (a) Schematic representation of the preparation of N-doped carbon sheets. (b) The capacity retention of the N-doped carbon sheets at current densities from 56.25 mA g^{-1} to 11.25 A g^{-1}. (c) Charge and discharge curves of the carbon sheets//$Na_3V_2(PO_4)_3$ sodium ion batteries at 562 mA g^{-1}. Reproduced from ref. 316 with permission from Wiley-VCH.

10 000 cycles (Fig. 18f). Apart from polymers, other carbon-rich compounds were used to synthesize disordered carbon.[332–334] For instance, Ji's group[333] first synthesized oligomer chain-based carbon quantum dots from acetone through aldol and polymerization reaction. After carbonization at 800 °C, the quantum dots were self-assembled into 3D porous carbon frameworks with an interlayer spacing of 0.42 nm. The maximum reversible capacity of these 3D porous carbon frameworks reached 255.5 mA h g^{-1}. By directly carbonizing sodium citrate at 700 °C, Yan with his colleagues[332] reported a kind of 3D carbon framework with a high reversible specific capacity of 330 mA h g^{-1} at 50 mA g^{-1}.

(3) Heteroatom-doped carbon anodes. Heteroatom doping (including N-doping,[158,159,305,314,322,326,335–338] P-doping,[115,336,339] S-doping,[159,314,339,340] B-doping[338,339]) is also viewed as an efficient way to boost the Na-ion storage capacity. Two functions of heteroatoms were concluded: one is to dilate the carbon layer and promote Na^+ intercalation/deintercalation into graphite, and the other is to provide additional Na^+ storage sites. Like heteroatom-doped carbon materials for LIBs, heteroatom-doped carbon materials for NIBs were realized by either using heteroatom-containing carbon precursors or using additional heteroatom donors. N-Doped carbon has been the earliest and also the most studied heteroatom-doped carbon. As an example, Zhao with his colleagues[322] obtained a kind of N-doped hard carbon nanoshell from an artemia cyst shell precursor. The precursor was mixed with KOH and $Ni(AC)_2$ and carbonized at 850 °C. During the pyrolysis, Ni^{2+} first chelated with chitosan in artemia cyst shells, and then catalyzed the graphitization of carbon. Meanwhile, KOH activated the carbon materials by producing a great deal of micropores. The obtained N-doped carbon materials exhibited a high reversible Na^+-storage capacity of 325 mA h g^{-1} at 100 mA g^{-1}. After 200 cycles, a specific capacity of 174 mA h g^{-1} was retained. Xu *et al.*[305] annealed 3D graphite oxide under a mixture of NH_3 and Ar at 800 °C to synthesize a 3D N-doped graphene material (denoted as N-GF). XPS revealed a N-doping level of 5.9 at% for the obtained 3D N-doped graphene. 3D graphene without N doping was also synthesized for comparison (denoted as rGF). Impressively, the initial reversible capacity of N-GF (1057.1 mA h g^{-1}) at 100 mA g^{-1} was substantially higher than that of rGF (836.2 mA h g^{-1}). At an ultra large current density of 5 A g^{-1}, the specific capacity of N-GF was still maintained at 137.7 mA h g^{-1}, whilst rGF only showed a low specific capacity of 10.5 mA h g^{-1}.

Apart from the N dopant, other heteroatoms also have a significant influence on the structure of carbon materials. Recently, with the assistance of experimental studies and computational calculations, Li *et al.*[339] evaluated the effect of P doping, S doping and N-doping on the Na-storage behavior. Different kinds of heteroatom-doped carbon materials were synthesized by pyrolyzing the mixture of carbon precursor (sucrose/graphite oxide, 80 : 1) with different oxo acids (H_3PO_4, H_2SO_4 or H_3BO_3). The XRD results (Fig. 19a) identified that P-doped (0.395 nm) and S-doped (0.383 nm) carbon had enlarged average interlayer spacings, while B-doped carbon (0.378 nm) had almost the same interlayer spacing as non-doped carbon materials (0.377 nm). Fig. 19b further compares the first-cycle charge/discharge curves at 20 mA g^{-1}. As revealed, the Na^+-storage capacity at low-voltage plateau is greatly improved for P-doped (240 mA h g^{-1}) and S-doped (213 mA h g^{-1}) carbon compared with non-doped carbon (175 mA h g^{-1}), which

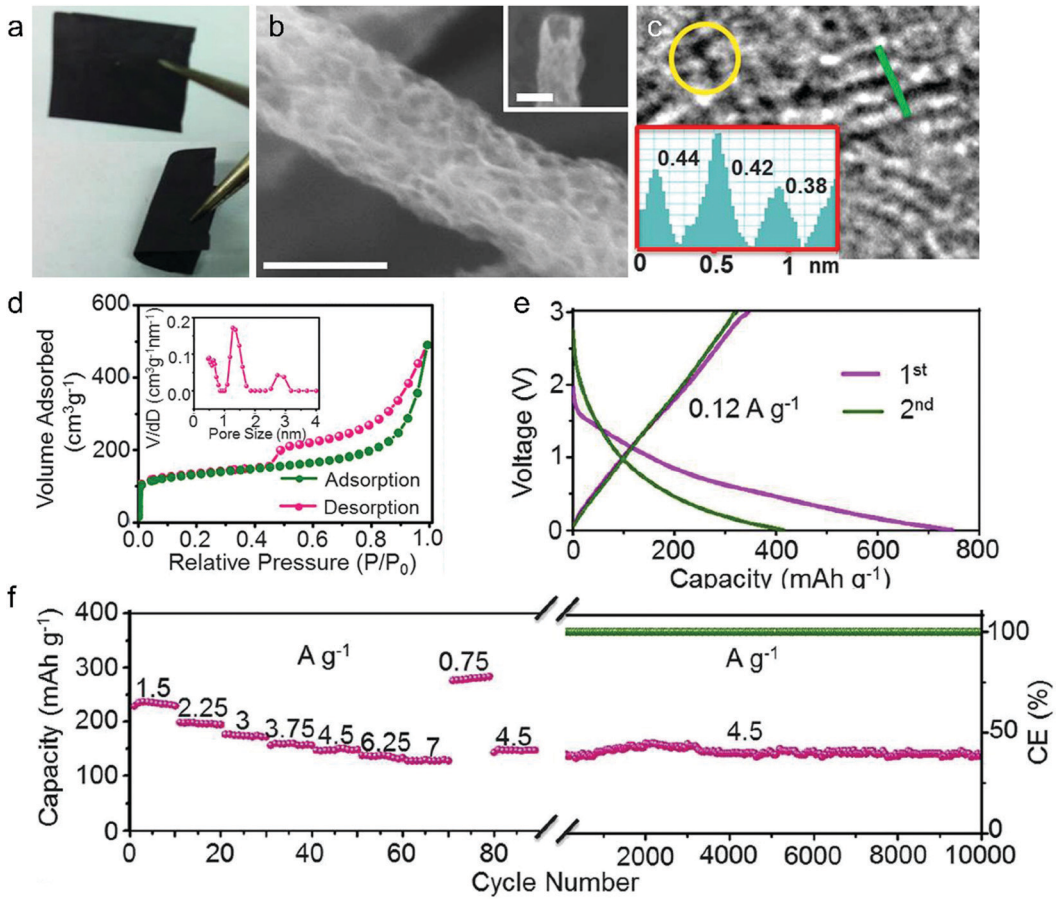

Fig. 18 (a) Digital photograph, (b) SEM image (scale bars: 100 nm), (c) high-resolution TEM image, (d) nitrogen adsorption–desorption isotherms and pore-size distributions, (e) charge–discharge voltage profiles at 0.12 A g^{-1}, and (f) cycling performance at 4.5 A g^{-1} of the polyacrylonitrile/$Zn(Ac)_2$/$Co(Ac)_2$ nanofiber derived porous carbon nanofiber networks. Reproduced from ref. 331 with permission from Elsevier.

can be assigned to the promoted Na^+ intercalation into the carbon interlayer. Meanwhile, the Na^+-storage capacity at the sloping voltage region is enhanced for P-doped (245 mA h g^{-1}) and B-doped (304 mA h g^{-1}) carbon compared to non-doped carbon (178 mA h g^{-1}), which was explained by the increased defect concentration of carbon materials. This study suggests that the

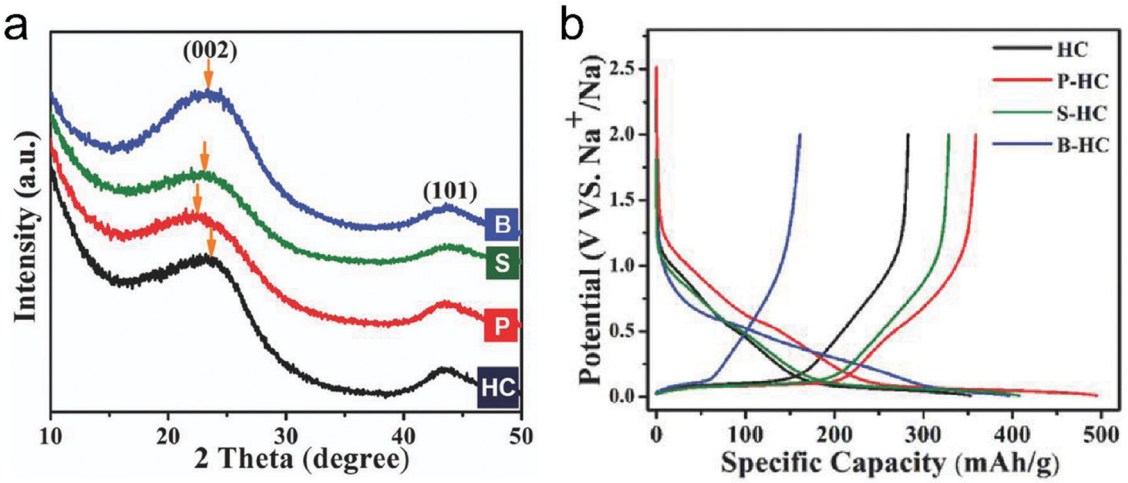

Fig. 19 (a) XRD patterns of doped and undoped carbons. After P- and S-doping, the (002) peak shifts to a lower angle, which indicates a larger d-spacing. However, B-doping barely shifts the peak. (b) Galvanostatic sodiation/desodiation potential profiles of hard carbon and doped hard carbons at a current rate of 20 mA g^{-1}. Reproduced from ref. 339 with permission from Wiley-VCH.

superior hard carbon materials for SIBs should have both high reversibly Na-binding defects and expanded carbon interlayer spacing. Moreover, Zhou's group[159] employed a sol–gel approach to first get a mixed precursor containing urea and citric acid. Afterwards, the precursor was annealed under Ar/H_2S at 650 °C, obtaining N,S-codoped carbon nanosheets. Interestingly, compared with only N-doped carbon nanosheets (0.350 nm), N,S-codoped carbon nanosheets show obviously expanded interlayer spacings (0.377 nm). The specific capacity of N,S-codoped carbon nanosheets also showed great enhancement compared with N-doped carbon nanosheets, for example, 419 mA h g^{-1} *vs.* 237.2 mA h g^{-1} for the first-cycle reversible capacity at 50 mA g^{-1}. Wang *et al.*[338] reported a kind of B,N-codoped carbon nanofiber by annealing the mixture of bacterial cellulose with $NH_4HB_4O_7{\cdot}H_2O$ under an Ar atmosphere. The obtained B,N-codoped carbon nanofibers exhibited an ultrahigh reversible capacity of 691 mA h g^{-1} at 100 mA g^{-1}, but a low CE of 36.6%. A good cycling stability was also verified by a low capacity decay of 0.57% per cycle after 120 cycles at 100 mA g^{-1}.

To correlate the structural parameters of carbon materials with their Na^+-storage performance, Table 4 compares the recently reported carbon materials for Na^+ storage.

4.1.3 Carbon anodes for KIBs

(1) Ordered carbon anodes. The research on carbon anodes for KIBs has been stimulated starting from 2015, when Ji's group[125] and Hu's group[160] reported the reversible K^+ intercalation/de-intercalation behavior of graphite, respectively (as discussed early in Section 3.1.3). However, in these two early studied cases, K^+ intercalation into graphite suffers from low initial CE, low rate capability, as well as fast capacity decay. To alleviate these issues faced by K^+ intercalated graphite, early research tried to optimize the employed electrolytes and binders. For example, Komaba *et al.*[341] demonstrated that the binders sodium polyacrylate and sodium carboxymethylcellulose were beneficial to improve the first-cycle CE. In an electrolyte of 1 M KFSI in EC/DEC, graphite with sodium polyacrylate (89%) and sodium carboxymethylcellulose binders (79%) showed superior first-cycle CEs compared to graphite with the traditional poly(vinylidene fluoride) binder (only 59%). The improved CE was explained by the pre-formation of the SEI and the suppressed defluorination of poly(vinylidene fluoride). Wang with his colleagues[342] studied the K^+-storage performance of graphite in different electrolytes, including 1 M KPF_6 dissolved in EC/DMC, EC/DEC, and EC/PC. Both electrolytes with EC/DEC and EC/PC solvents enabled a high first-cycle CE and stable cycling performance after 200 cycles for the graphite electrode. By contrast, graphite with the EC/DMC based electrolyte could not form a stable SEI film, thus resulting in a fast capacity decay after 70 cycles. Moreover, Cohn *et al.*[343] reported K^+ intercalation into graphite with diglyme and monoglyme based electrolytes. Without the desolvation process, the co-intercalation of K^+ and solvent into graphite allowed for a specific capacity of 100 mA h g^{-1} at 200 mA g^{-1}, a fast rate capability with a capacity retention of 80% at 10 A g^{-1}, and stable cycling performance with 5% capacity decay after 2000 cycles at 2 A g^{-1}A g^{-1}.

Recently, the K^+-storage behavior was also studied for other ordered nanoscale carbon materials, like nanosized graphitic carbon,[345] graphene,[161,346] and CNTs.[344,347,348] For instance, Song *et al.*[345] annealed Ketjen carbon black at 2800 °C and obtained graphitic carbon nanocages with an average diameter of about 50 nm and a thin shell of 5 nm. Such a unique structure was capable of accommodating strain relaxation during K^+ intercalation/de-intercalation, reducing the ion diffusion length and accelerating electron transport. The obtained graphitic carbon nanocages delivered a reversible specific capacity of 221.5 mA h g^{-1} at 28 mA g^{-1}. Remarkably, the specific capacity maintained 79% of the capacity at 28 mA g^{-1} when the current was increased to 9.7 A g^{-1}, suggesting the ultrahigh rate capability. By using Ni foam as a catalyst and CH_3CN as a precursor, Share and co-authors[161] employed the CVD method to grow N-doped graphene materials. The obtained N-doped graphene showed a high specific capacity of 350 mA h g^{-1}, significantly outperforming the theoretical capacity of graphite (278 mA h g^{-1}). The cycling tests at 100 mA g^{-1} revealed a fair electrochemical stability of the N-doped graphene anode with an initial capacity of 270 mA h g^{-1} and a final capacity of 210 mA h g^{-1} after 100 charge/discharge cycles. In addition, Wang *et al.*[344] reported a kind of hyperporous sponge made of highly tangled CNTs, which were synthesized by a CVD approach with ferrocene as the catalyst and 1,2-dichlorobenzene as the carbon precursor. The CNTs were featured by dense-stacked inner walls and loose-stacked outer walls (Fig. 20a). The interlayer spacing of inner walls was revealed to be 0.344 nm, close to that of graphite, while the outer walls appeared to be disordered with an average interlayer spacing of 0.427 nm (Fig. 20b). Fig. 20c shows the initial three CV cycles of the sponge as the anode for K^+ storage. During the first cathodic scan, there are three cathodic peaks at 0.01, 0.2, and 0.5 V *vs.* K^+/K. Afterwards, the peak at 0.5 V *vs.* K^+/K disappeared due to the formation of an irreversible SEI film, and two anodic peaks at 0.4 and 0.6 V *vs.* K^+/K appeared. After activation for 50 cycles, the obtained CNT sponge delivered a reversible specific capacity of 232 mA h g^{-1} at 100 mA g^{-1}, and an outstanding stability with negligible capacity decay after 500 cycles (Fig. 20d). *Ex situ* TEM images provide important understanding of the superior K^+-storage behavior of the obtained CNT sponge (Fig. 20e). The K^+ intercalation mainly took place within the outer CNT walls, while the inner CNT walls functioned as a robust skeleton. During the repeat charge/discharge, the obtained CNT sponge presented reversible expansion/shrinkage.

(2) Disordered carbon anodes. Research on disordered carbon for KIBs occupies the dominant research trend for carbon based KIB anodes, particularly in these five years. Biomass materials (*e.g.* chitin,[350,351] bacterial cellulose,[341,349] potato,[352] pepper,[353] walnut septum,[354] and juice[355]) are one key category to synthesize disordered carbon materials for K^+ storage, owing to their abundant, renewable and eco-friendly features. Through a simple pyrolysis process as well as washing and drying, the derived carbon can be produced on a large scale. For instance, Zhang's group[351] developed an emulsion method to fabricate chitin microspheres by dissolving chitin in NaOH/urea aqueous solution. By directly carbonizing chitin microspheres under an

Table 4 Comparison of recently reported carbon materials for Na^+ storage

Type of carbon material	Specific surface area	Interlayer distance	Specific capacity	First-cycle CE	Cycling stability	Ref.
rGO	330.9 $m^2 g^{-1}$	—	174.3 mA h g^{-1} at 40 mA g^{-1} 95.6 mA h g^{-1} at 1 A g^{-1}	20%	45% at 40 mA g^{-1} over 1000 cycles	151
rGO paper	—	0.365 nm	115 mA h g^{-1} at 100 mA g^{-1} 52 mA h g^{-1} at 2.4 A g^{-1}	28%	87% at 100 mA g^{-1} over 1000 cycles	300
Holey graphene	750 $m^2 g^{-1}$	0.375 nm	220 mA h g^{-1} at 30 mA g^{-1} 85 mA h g^{-1} at 10 A g^{-1}	22%	72% at 100 mA g^{-1} over 500 cycles	301
Hydrogenated graphene	—	—	430 mA h g^{-1} at 100 mA g^{-1} 240 mA h g^{-1} at 5 A g^{-1}	8.6%	—	302
rGO		0.365 nm	428 mA h g^{-1} at 25 mA g^{-1} 162 mA h g^{-1} at 500 mA g^{-1}	18.5%	81% at 125 mA g^{-1} over 750 cycles	303
Graphene paper	47.4 $m^2 g^{-1}$	—	183 mA h g^{-1} at 100 mA g^{-1} 61 mA h g^{-1} at 8 A g^{-1}	32.7%	74% at 1 A g^{-1} over 500 cycles	304
Graphene	523 $m^2 g^{-1}$	0.374 nm	225 mA h g^{-1} at 50 mA g^{-1} 51 mA h g^{-1} at 1 A g^{-1}	46.8%	—	149
3D N-doped graphene	357 $m^2 g^{-1}$	0.342 nm	1057 mA h g^{-1} at 100 mA g^{-1} 137.7 mA h g^{-1} at 5 A g^{-1}	42.6%	70% at 500 mA g^{-1} over 150 cycles	305
Peat moss derived N-doped carbon	196 $m^2 g^{-1}$	0.388 nm	203 mA h g^{-1} at 500 mA g^{-1} 66 mA h g^{-1} at 5 A g^{-1}	57.5%	88% at 100 mA g^{-1} over 200 cycles	306
Banana peel derived N-doped carbon	130.8 $m^2 g^{-1}$	0.392 nm	355 mA h g^{-1} at 50 mA g^{-1} 80 mA h g^{-1} at 5 A g^{-1}	70%	93% at 500 mA g^{-1} over 600 cycles	307
Peanut shell derived N-doped carbon	706.1 $m^2 g^{-1}$	—	320 mA h g^{-1} at 250 mA g^{-1} 140 mA h g^{-1} at 1 A g^{-1}	30%	77% at 250 mA g^{-1} over 400 cycles	308
Coconut oil derived S-doped carbon	56 $m^2 g^{-1}$	—	198 mA h g^{-1} at 100 mA g^{-1} 78 mA h g^{-1} at 1 A g^{-1}	49%	85% at 100 mA g^{-1} over 200 cycles	309
Cotton derived hard carbon	38 $m^2 g^{-1}$	0.410 nm	315 mA h g^{-1} at 30 mA g^{-1} 180 mA h g^{-1} at 300 mA g^{-1}	83%	97% at 30 mA g^{-1} over 100 cycles	310
Garlic peel derived N-doped carbon	1710 $m^2 g^{-1}$	0.379 nm	270 mA h g^{-1} at 250 mA g^{-1} 37 mA h g^{-1} at 4 A g^{-1}	41%	88% at 100 mA g^{-1} over 100 cycles	311
Wood derived carbon	—	—	270 mA h g^{-1} at 10 mA g^{-1}	70%	—	312
Apple-biowaste derived carbon	196.3 $m^2 g^{-1}$	0.385 nm	245 mA h g^{-1} at 4 mA g^{-1} 86 mA h g^{-1} at 2 A g^{-1}	61%	113% at 1 A g^{-1} over 1000 cycles	313
Cellulose/polyaniline derived N,S-doped carbon	—	0.406 nm	280 mA h g^{-1} at 30 mA g^{-1} 131 mA h g^{-1} at 5 A g^{-1}	23%	100% at 500 mA g^{-1} over 3400 cycles	314
Cellulose derived carbon	117 $m^2 g^{-1}$	0.377 nm	280 mA h g^{-1} at 20 mA g^{-1}	54%	83% at 200 mA g^{-1} over 170 cycles	315
Okara derived N-doped carbon	—	0.390 nm	302 mA h g^{-1} at 56 mA g^{-1} 32 mA h g^{-1} at 11.25 A g^{-1}	—	65% at 1.7 A g^{-1} over 2000 cycles	316
Leaf-derived lamellar carbon	—	—	254 mA h g^{-1} at 20 mA g^{-1} 103 mA h g^{-1} at 200 mA g^{-1}	60%	99% at 20 mA g^{-1} over 100 cycles	317
Argan shell derived carbon	23 $m^2 g^{-1}$	0.393 nm	333 mA h g^{-1} at 25 mA g^{-1}	79%	96% at 25 mA g^{-1} over 100 cycles	318
Pistachio shell derived carbon	760.9 $m^2 g^{-1}$	0.370 nm	225 mA h g^{-1} at 10 mA g^{-1} 90 mA h g^{-1} at 200 mA g^{-1}	71%	86.3% at 40 mA g^{-1} over 50 cycles	319
Shrimp skin derived N-doped carbon	531 $m^2 g^{-1}$	0.366 nm	276 mA h g^{-1} at 100 mA g^{-1} 160 mA h g^{-1} at 1 A g^{-1}	32%	71% at 50 mA g^{-1} over 300 cycles	320
Mangosteen shell derived carbon	81.5 $m^2 g^{-1}$	0.371 nm	275 mA h g^{-1} at 20 mA g^{-1} 98 mA h g^{-1} at 200 mA g^{-1}	74%	98% at 20 mA g^{-1} over 100 cycles	321
Artemia cyst shell derived N-doped carbon	1490 $m^2 g^{-1}$	0.347–0.400 nm	1253 mA h g^{-1} at 100 mA g^{-1} 175 mA h g^{-1} at 20 A g^{-1}	53.4%	54% at 100 mA g^{-1} over 200 cycles	322
Macadamia shell derived carbon	32.4 $m^2 g^{-1}$	0.390 nm	297 mA h g^{-1} at 30 mA g^{-1} 260 mA h g^{-1} at 300 A g^{-1}	91.4%	30 mA g^{-1} for 850 h	323
Polyvinyl chloride nanofiber derived carbon	—	0.351 nm	389 mA h g^{-1} at 12 mA g^{-1} 147 mA h g^{-1} at 240 mA g^{-1}	69.9%	84% at 12 mA g^{-1} over 150 cycles	325
N-Doped carbon/graphene	94.1 $m^2 g^{-1}$	0.360 nm	336 mA h g^{-1} at 30 mA g^{-1} 94 mA h g^{-1} at 5 A g^{-1}	52%	89% at 50 mA g^{-1} over 200 cycles	326
Polyaniline derived N-doped carbon	23.5 $m^2 g^{-1}$	0.366 nm	270 mA h g^{-1} at 50 mA g^{-1} 45 mA h g^{-1} at 2.5 A g^{-1}	51.6%	77% at 50 mA g^{-1} over 500 cycles	327
N-Doped carbon nanofiber film	564.4 $m^2 g^{-1}$	—	564 mA h g^{-1} at 100 mA g^{-1} 154 mA h g^{-1} at 15 A g^{-1}	35%	99% at 5 A g^{-1} over 7000 cycles	329
Polyaniline derived carbon nanofibers	21 $m^2 g^{-1}$	—	200 mA h g^{-1} at 35 mA g^{-1}	—	87% at 35 mA g^{-1} over 50 cycles	330
PAN/$Co(Ac)_2$/ZIF derived N-doped carbon	438 $m^2 g^{-1}$	0.380–0.440 nm	346 mA h g^{-1} at 120 mA g^{-1} 128 mA h g^{-1} at 7 A g^{-1}	47%	95% at 4.5 A g^{-1} over 10 000 cycles	331
Sodium citrate derived 3D carbon	<370 $m^2 g^{-1}$	0.340–0.510 nm	440 mA h g^{-1} at 50 mA g^{-1} 100 mA h g^{-1} at 20 A g^{-1}	32.2%	100% at 10 A g^{-1} over 10 000 cycles	332
3D porous carbon	467 $m^2 g^{-1}$	0.420 nm	255 mA h g^{-1} at 500 mA g^{-1} 100 mA h g^{-1} at 20 A g^{-1}	34.7%	96% at 5 A g^{-1} over 10 000 cycles	333
$C_{24}H_8O_6$ derived soft carbon	20.2 $m^2 g^{-1}$	0.356 nm	200 mA h g^{-1} at 20 mA g^{-1} 114 mA h g^{-1} at 1 A g^{-1}	67.6%	89% at 1 A g^{-1} over 240 cycles	334

Table 4 (*continued*)

Type of carbon material	Specific surface area	Interlayer distance	Specific capacity	First-cycle CE	Cycling stability	Ref.
Hard carbon	8.5 $m^2 g^{-1}$	0.377 nm	283 mA h g^{-1} at 20 mA g^{-1}	80.1%	—	339
P-Doped hard carbon	7.3 $m^2 g^{-1}$	0.395 nm	359 mA h g^{-1} at 20 mA g^{-1}	74.0%	91% at 20 mA g^{-1} over 200 cycles	
B-Doped hard carbon	8.0 $m^2 g^{-1}$	0.378 nm	147 mA h g^{-1} at 20 mA g^{-1}	36.4%	98% at 20 mA g^{-1} over 200 cycles	
S-Doped hard carbon	5.2 $m^2 g^{-1}$	0.383 nm	328 mA h g^{-1} at 20 mA g^{-1}	80.4%	87% at 20 mA g^{-1} over 200 cycles	
N-doped carbon	945 $m^2 g^{-1}$	0.367 nm	437 mA h g^{-1} at 100 mA g^{-1} 96 mA h g^{-1} at 6.4 A g^{-1}	52%	79% at 1.6 A g^{-1} over 5000 cycles	335
N,P-Doped carbon	432 $m^2 g^{-1}$	—	305 mA h g^{-1} at 100 mA g^{-1} 136 mA h g^{-1} at 5 A g^{-1}	47%	80% at 100 mA g^{-1} over 50 cycles	336
B,N-Doped carbon nanofibers	1585 $m^2 g^{-1}$	0.440 nm	691 mA h g^{-1} at 100 mA g^{-1} 314 mA h g^{-1} at 10 A g^{-1}	36.6%	85% at 10 A g^{-1} over 1000 cycles	338
N-Doped carbon nanosheets	214 $m^2 g^{-1}$	0.361 nm	278 mA h g^{-1} at 100 mA g^{-1} 159 mA h g^{-1} at 10 A g^{-1}	54.2%	114% at 10 A g^{-1} over 10 000 cycles	337
N,S-Doped carbon	379.4 $m^2 g^{-1}$	0.378 nm	350 mA h g^{-1} at 50 mA g^{-1} 110 mA h g^{-1} at 10 A g^{-1}	44%	96% at 1 A g^{-1} over 1000 cycles	159
PO_x-Doped carbon	—	0.386 nm	359 mA h g^{-1} at 20 mA g^{-1}	73%	92% at 200 mA g^{-1} over 150 cycles	115
S-Doped carbon	139.7 $m^2 g^{-1}$	0.386 nm	482 mA h g^{-1} at 100 mA g^{-1} 119 mA h g^{-1} at 5 A g^{-1}	73.6%	94.2% at 500 mA g^{-1} over 700 cycles	340

Ar atmosphere, they further prepared N-doped carbon nanospheres and employed them as the anode for KIBs. It was demonstrated that the obtained carbon nanospheres delivered a high specific capacity of 250 mA h g^{-1} at 33.6 mA g^{-1}, an excellent rate capability with a specific capacity of 154 mA h g^{-1} at 20.16 A g^{-1}, as well as an ultralong stability of 4000 cycles. Recently, Li *et al.*[349] also reported a kind of carbon aerogel derived from bacterial cellulose, which showed a remarkable K^+-storage ability. Bacterial cellulose can be produced by the fermentation of *Acetobacter xylinum*, which is a cost-effective and upscalable process. In this study, bacterial cellulose hydrogel was first freeze-dried into aerogel, and then pyrolyzed at a temperature of 1000 °C under a N_2 atmosphere (Fig. 21a). The lightweight carbon aerogel has a mass density of about 5.3 mg cm^{-3}, which enables it to stand on a flower stably (Fig. 21b). It can bear a compression of up to 90% volume change and recover to the initial state without structural collapse, implying its robust elasticity. The SEM image (Fig. 21c) reveals that the carbon aerogel is featured with a porous 3D reticulated structure made of numerous tangled carbon nanofibers. The high-resolution TEM image (Fig. 21d) clearly shows numerous nanopores uniformly distributed on the surface of each nanofiber. With such a hierarchical porous structure, the obtained carbon aerogel shows a large specific surface area of 778 $m^2 g^{-1}$ with rich micropores accounting for 53% of the total surface area (Fig. 21e). The K^+-storage ability of the carbon aerogel was assessed in a half cell with a voltage window of 0.01–2.80 V *vs.* K^+/K. By collecting CV curves at various scan rates, the K^+-storage behavior of the obtained carbon aerogel was determined to be a surface-driven dominant process (Fig. 21f). Even at a low scan rate of 0.2 mV s^{-1}, the capacitive contribution to the whole K^+ storage reached up to 51%. This surface-dominant K^+ storage behavior enabled the carbon aerogel a fast rate capability. The specific capacity of the carbon aerogel was 240 mA h g^{-1} at 50 mA g^{-1}; meanwhile the specific capacity was still maintained at 164 mA h g^{-1} at 1 A g^{-1} (Fig. 21g). Moreover, after 2000 charge/discharge cycles at 1 A g^{-1}, the carbon aerogel still showed a specific capacity of 158 mA h g^{-1}, indicating an average capacity decay rate of only 0.006% per cycle (Fig. 21h). Afterwards, the carbon aerogel could be stably operated at 2 A g^{-1} for another 1500 cycles, and subsequently at 5 A g^{-1} for another 1000 cycles. It should be pointed out that, although the high porosity and large specific surface area endowed a fast rate capability of the obtained carbon anodes for KIBs, they also led to the low first-cycle CE of the carbon anodes (less than 50%).

Synthetic carbon-rich compounds have also attracted widespread attention as carbon precursors for synthesizing K^+-storage disordered carbon. So far, various polymers have been explored to fabricate porous hard carbon materials for K^+ storage, including electrospun PAN,[357,358] polymerization product of sucrose,[359] melamine–formaldehyde resin,[158,356] polyaniline,[360] and sodium polyacrylate.[361] For instance, Ji's group[359] used a hydrothermal reaction of sucrose solution to get the polymerization microspheres of sucrose, which were further carbonized at 1100 °C for 5 hours under Ar gas. The obtained carbon microspheres were subjected to assessment of their Na^+- and K^+- storage ability. Interestingly, they showed a lower K^+-storage capacity (262 mA h g^{-1}) than Na^+-storage capacity (322 mA h g^{-1}) at a low current density of 28 mA g^{-1}, but a better K^+-storage rate capability (136 mA h g^{-1} at 1.4 A g^{-1}) than Na^+-storage rate capability (73 mA h g^{-1} at 1.4 A g^{-1}). This result was explained by the larger diffusion coefficient of K^+ in carbon microspheres compared to that of Na^+. Bin *et al.*[356] recently observed an interesting glass blowing effect of the melamine–formaldehyde resin during pyrolysis, which resulted in a hollow 3D carbon foam. They selected commercial melamine–formaldehyde resin sponge as the precursor, and annealed it at 1300 °C under a N_2 atmosphere. As shown in Fig. 22a, the pyrolysis process includes two steps, one is scission of ether linkages at temperature below 365 °C

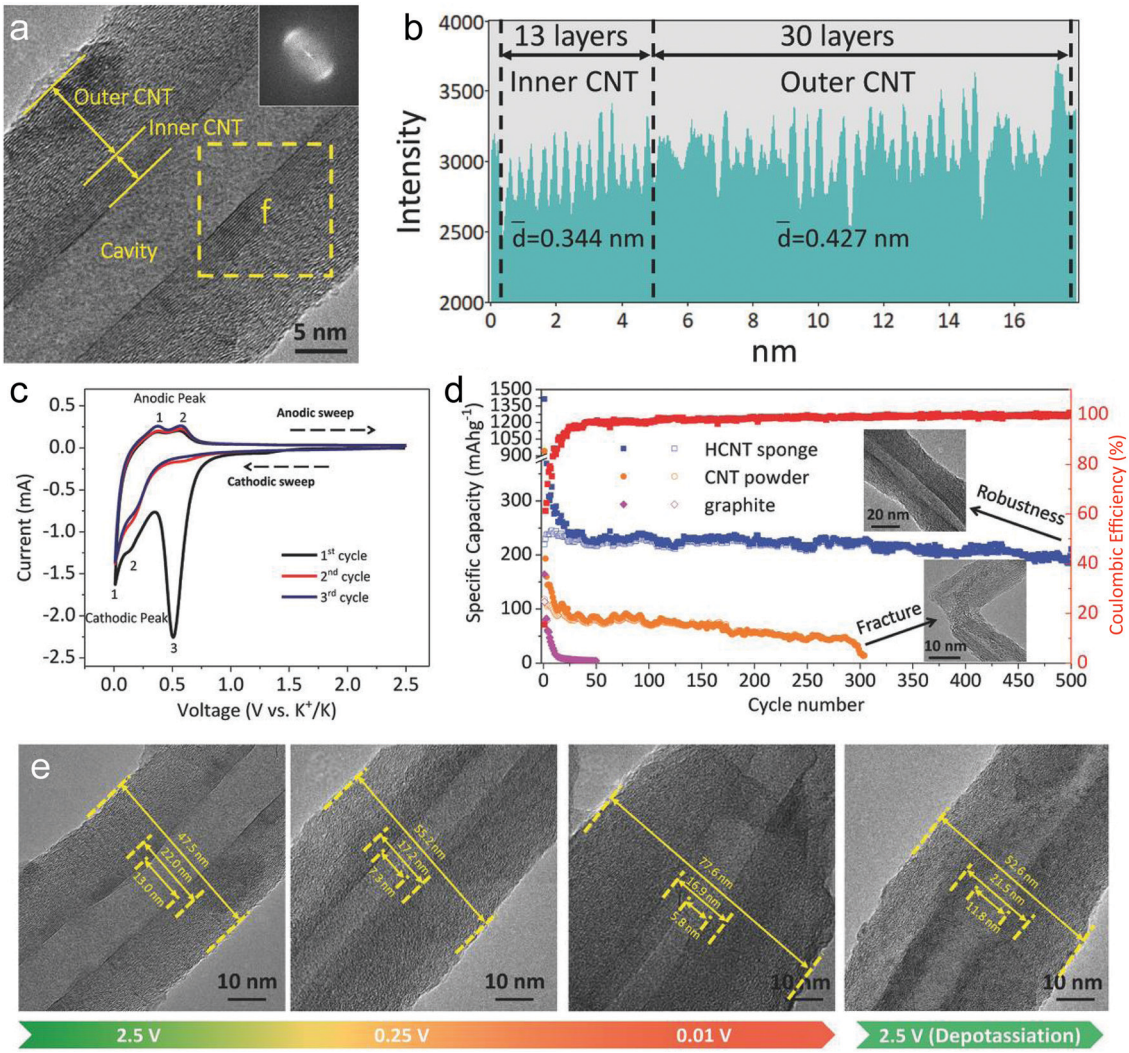

Fig. 20 (a) TEM image of a CNT. (b) Line profile obtained from the wall of a CNT. (c) CV curves of CNT sponge at 0.3 mV s^{-1}. (d) Cycling performance of CNT sponge, commercial CNT powder and graphite electrodes at a current density of 100 mA g^{-1}. (e) *Ex situ* TEM images of the CNT structure at different potassiation and de-potassiation potential in the first cycle. Reproduced from ref. 344 with permission from Wiley-VCH.

which softens the resin structure, and the other is release of large amounts of gas at temperature above 365 °C, which inflated the skeleton. The important role of ether linkages was also verified by the control experiment, in which solid carbon foam was obtained by firstly annealing the sponge at 365 °C to remove the ether bridge, then cooling down, and finally annealing it again at 1300 °C. EIS results (Fig. 22b) revealed that hollow carbon foam showed the lowest charge-transfer impedance compared with solid carbon foam and carbon powder, which could be attributed to the shortened K^+ diffusion distance of the hollow structure with thin walls. Remarkably, the obtained hollow carbon foam showed a high reversible capacity of 340 mA h g^{-1} at 28 mA g^{-1}, greatly outperforming the solid carbon foam and powder carbon (Fig. 22c). Of note is that the first-cycle CE of the hollow carbon foam reached up to 72.1%. At a high current density of 558 mA g^{-1}, the specific capacity of the hollow carbon foam was still maintained around 110 mA h g^{-1}.

Metal–organic frameworks featured with ultra-large porosity and high crystallinity are also appropriate precursors for synthesizing nanoporous carbon materials.[362–364] MOFs are composed of metal centers and organic ligands. The organic ligands provide sufficient carbon sources, while the metal content (*e.g.* Co) shows a good catalytic ability to promote the formation of graphitic carbon even at low temperatures. For example, Hu and co-authors[362] directly annealed Co-containing zeolitic imidazolate frameworks (ZIF-67) at 600 °C, followed by washing with hard carbon to remove metal particles. They found that the size of the ZIF-67 precursor played a significant role in determining the morphology of the obtained carbon materials. When ZIF-67 was changed from microsize to nanosize, the derived carbon changed from particle morphology to interconnected 3D porous network morphology. At a low current density of 50 mA g^{-1}, the reversible specific capacity of the 3D porous carbon networks reached 270 mA h g^{-1}. Li *et al.*[364] reported the synthesis of the core–shell Zn-containing ZIF @ Co-containing ZIF structure, and carbonized it at 900 °C under N_2 for 5 hours. As the anode for KIBs, this carbon material also delivered an outstanding performance with a reversible specific capacity of

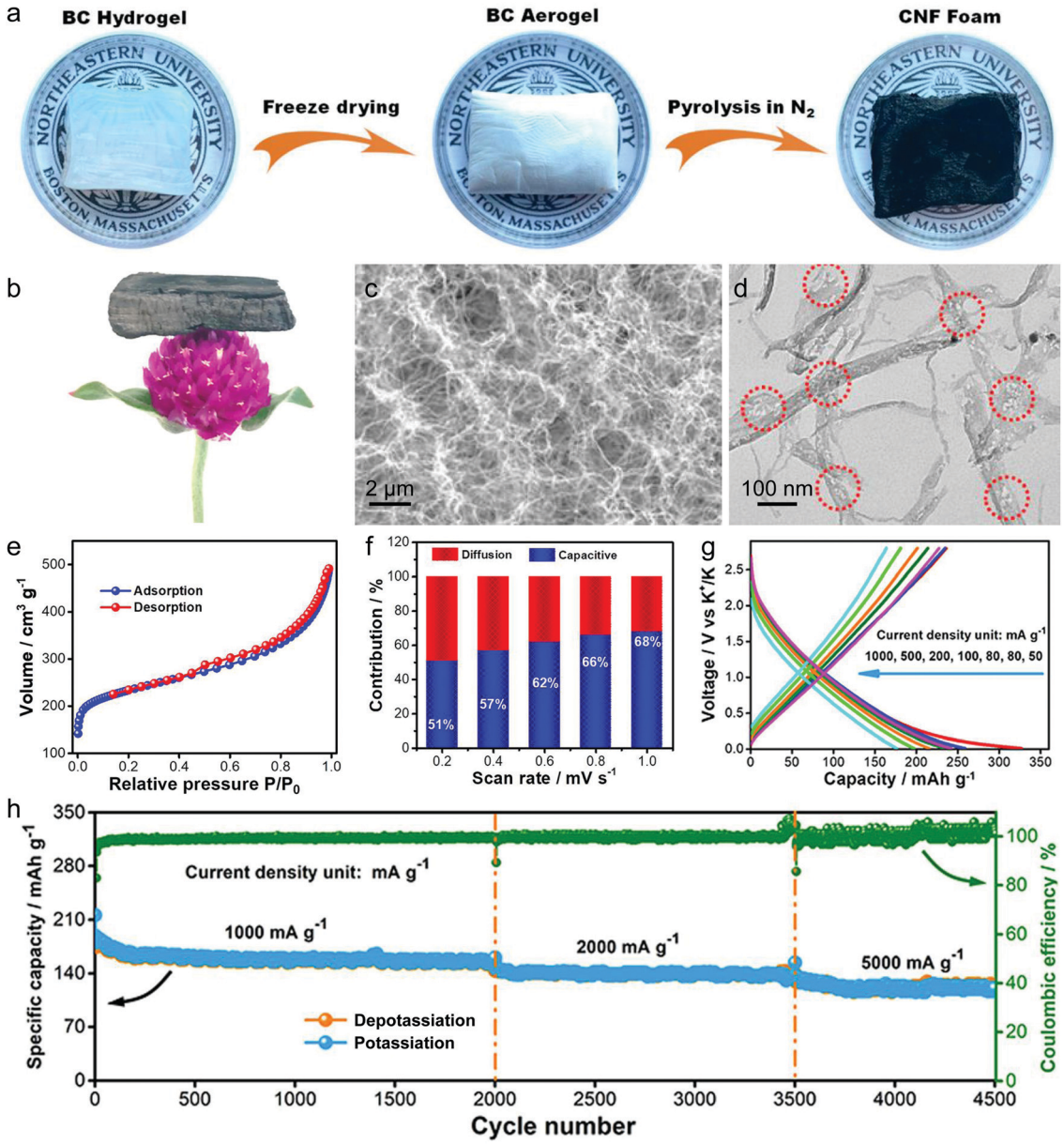

Fig. 21 (a) Schematic diagram of preparation of the bacterial cellulose derived carbon aerogel. (b) Photograph of the carbon aerogel standing on a flower, indicating its foam-like property. (c) SEM image, (d) TEM image, and (e) nitrogen adsorption–desorption isotherm curve of the carbon aerogel. (f) Contribution ratios of capacitive and diffusion capacities of the carbon aerogel electrode at various scan rates. (g) Depotassiation–potassiation profiles at various current densities. (h) Long-term cycling performances. Reproduced from ref. 349 with permission from American Chemical Society.

310 mA h g^{-1} at 100 mA g^{-1} after 200 cycles and good rate capability with a specific capacity of 120 mA h g^{-1} at 5 A g^{-1}.

Besides, some other organic molecules, including citric acid/urea,[365] sodium citrate/urea,[366] resorcinol formaldehyde,[367] 2-amino terephthalic acid,[368] sucrose,[80] and melamine,[369] were also directly selected as the precursors for the synthesis of disordered carbon. In most of the cases, templates were involved to promote the generation of pores with defined size, such as salts[361,366,369] and SiO_2.[80,367] Li *et al.*[366] ball-milled and annealed the mixture of sodium citrate and urea to synthesize a porous carbon anode for KIBs. During the calcination process, a large amount of Na_2CO_3 was formed which was wrapped by carbon nanosheets. After the removal of Na_2CO_3 templates, hierarchically porous carbon was obtained, showing favorable structural features, such as a large average interlayer distance (0.38 nm), a high specific surface area (340 m^2 g^{-1}), and multi-scale pores ranging from micro- to macro-pores. Importantly, the derived porous carbon showed a good K^+-storage ability with a high reversible specific capacity of 384.2 mA h g^{-1} at 100 mA g^{-1} after 500 cycles and a high rate capability with a specific capacity of 185 mA h g^{-1} at 10 A g^{-1}. Recently, Guo's group[80] used a silica template (SBA-15) and a sucrose precursor to fabricate mesoporous carbon with ordered 1D 6.5 nm-width channels (Fig. 23a). Meanwhile, the obtained mesoporous carbon showed

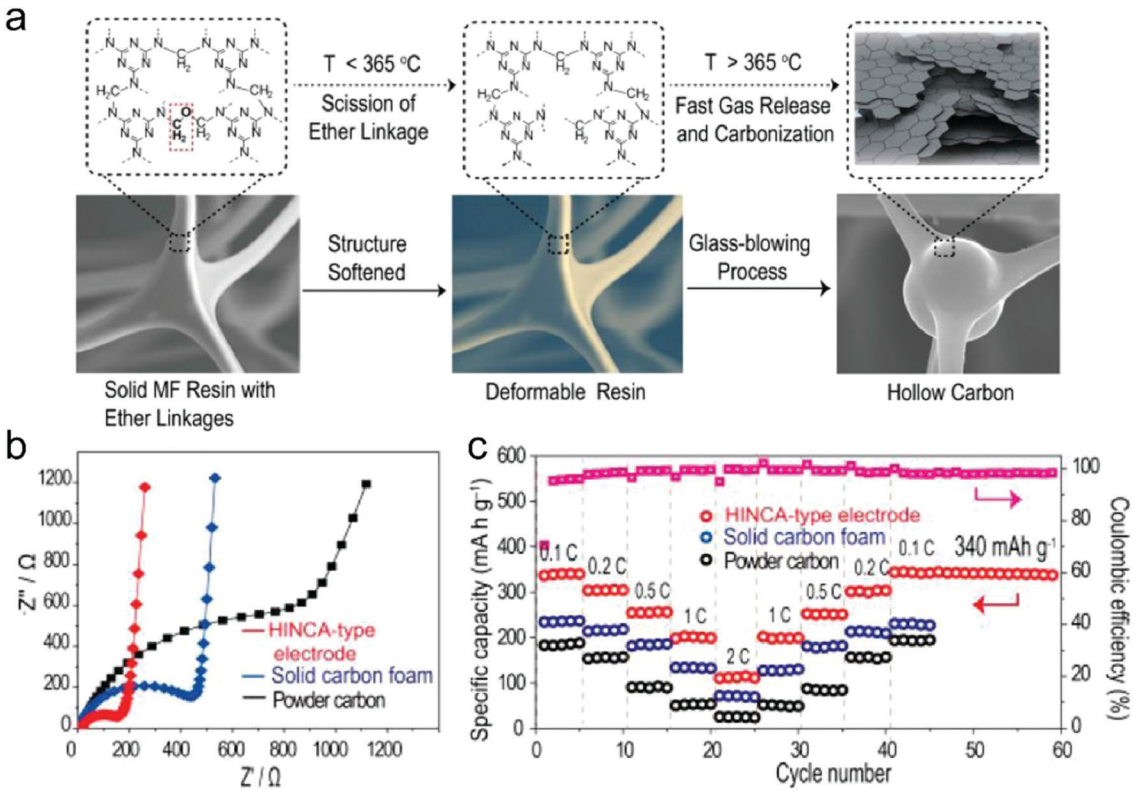

Fig. 22 (a) Schematic illustration of the spontaneous formation of the hollow carbon structure. (b) EIS and (c) rate capability of the obtained hollow carbon foam, solid carbon foam and carbon powder. Reproduced from ref. 356 with permission from American Chemical Society.

much larger interlayer spacing (0.52 nm) than crystalline graphite, allowing the storage of more K^+ into carbon layers and the toleration of the volume change during potassiation/de-potassiation. The initial discharge/charge capacities of the mesoporous carbon at 50 mA g^{-1} were measured to be 483.2 and 307.4 mA h g^{-1}, respectively, with a first-cycle CE of 63.6% (Fig. 23b). In the following 100 cycles, the capacity decay was much less, implying the reversible potassiation/de-potassiation. *Ex situ* XRD results (Fig. 23c) provided insightful understanding of the role of meso-channels in K^+ storage. A peak at 1.1° was observed at the initial state, evidencing the ordered mesoporous arrangement. At the potassiation state, the peak shifted towards a higher angle, suggesting the narrowed meso-channels. After de-potassiation, the peak recovered to the angle between the initial state and the full potassiation state, implying a decrease in the diameter of meso-channels. Moreover, the cycling test demonstrated that the mesoporous carbon could maintain a reversible capacity of 146.5 mA h g^{-1} for 1000 cycles at 1 A g^{-1} (Fig. 23d).

(3) Heteroatom-doped carbon anodes. As for Li^+-storage and Na^+-storage disordered carbon materials, introduction of heteroatoms is also pursued to improve the K^+-storage ability of disordered carbon materials. The most general approach to realize heteroatom doping is selecting heteroatom-containing precursors (biomass or synthetic carbon rich compounds). The most widely studied case is N doping.[158,358,360,363,365,368–370] Recently, Chang with his colleagues[365] conducted DFT calculations to simulate the adsorption of K^+ on different kinds of N-doping modes. The results showed that pyridinic N possessed the strongest K^+ adsorption ability with an adsorption energy of −3.71 eV, whilst pyrrolic N and quaternary N had a K^+ adsorption energy of −3.48 and −0.74 eV, respectively. This study inspires the design and synthesis of carbon materials with rich pyrrolic and pyridinic N for K^+ storage. Lei and co-authors[360] assessed the influence of the annealing temperature on N doping in polypyrrole nanofiber derived carbon. The derived carbon materials at 650, 950, and 1100 °C (denoted as NCNF-650, NCNF-950, and NCNF-1100) showed a similar hollow structure with an inner diameter of 30–40 nm and a wall thickness of 20 nm (Fig. 24a). As the annealing temperature increased, one could observe the diminishment of pyrrolic and pyridinic N, and the generation of quaternary N (Fig. 24b). Remarkably, NCNF-650 (368 mA h g^{-1}) presented much higher initial capacity than NCNF-950 (297 mA h g^{-1}) and NCNF-1100 (281 mA h g^{-1}), which agrees well with the previous conclusion that pyrrolic and pyridinic N contribute to K^+ storage (Fig. 24c). Moreover, the study demonstrated that the K^+ storage of NCNF-650 showed higher surface-dominated contribution than that of NCNF-950 and NCNF-1100 (Fig. 24d). This fact can be explained by the rich surface/edge defects in NCNF-650 induced by the N dopants, which benefited the high-kinetics K^+ storage. To demonstrate the possibility of the NCNF-650 anode for KIBs, a full cell was assembled by coupling with the Russian blue cathode. The cell tested in the voltage window of 2.0–4.2 V delivered a high specific capacity of 197 mA h g^{-1} (based on anode mass, Fig. 24e).

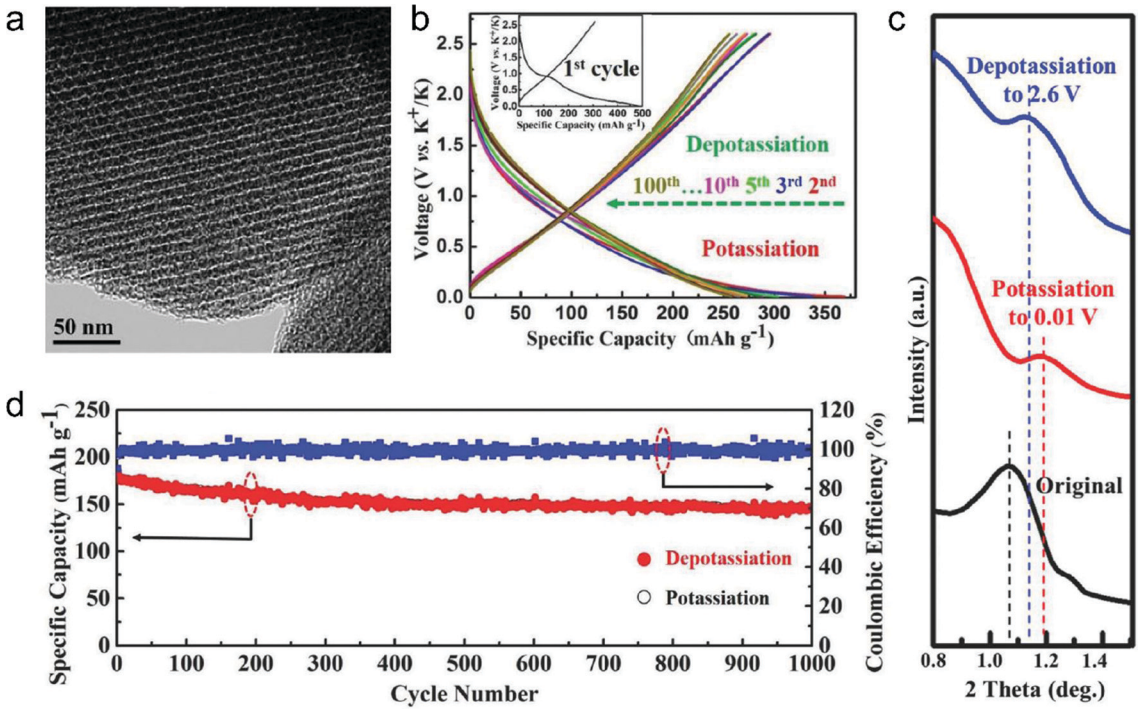

Fig. 23 (a) TEM, (b) the 2nd, 3rd, 5th, 10th, 20th, 30th, 50th, 75th, and 100th potassiation/depotassiation profiles, (c) *ex situ* XRD patterns, and (d) long-term cycling stability and CE of the mesoporous carbon. Reproduced from ref. 80 with permission from Wiley-VCH.

Aside from N doping, S doping was also explored by recent research by selecting sulfur-containing precursors.[203,346,371] For instance, Chen *et al.*[203] synthesized polymer microspheres by thermal curing the mixture of epoxy monomers and thiol hardeners in a liquid crystal solvent. Afterwards, S-doped carbon microspheres were derived by carbonizing the microspheres, which exhibited a

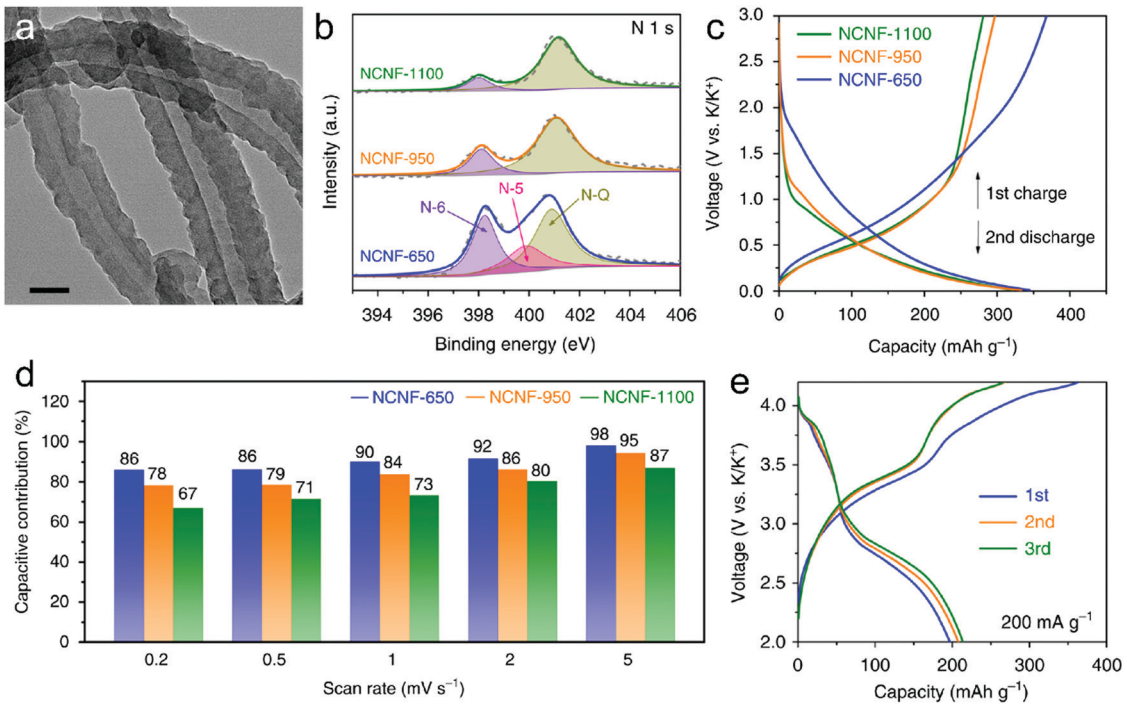

Fig. 24 (a) TEM of NCNF-650. (b) N 1s core level XPS high-resolution spectra, (c) first charge and second discharge profiles, and (d) contribution of the surface process at different scan rates of NCNF-650, NCNF-950, and NCNF-1100. (e) Galvanostatic charge/discharge profiles of the NCNF-650// Prussian blue full cell. Reproduced from ref. 360 with permission from Springer Nature.

high K^+-storage capacity of 226.6 mA h g^{-1} at 50 mA g^{-1}. Liu *et al.*[371] reported the synthesis of S,N-codoped hard carbon by annealing the mixture of polyacrylonitrile and sulfur. It showed a high reversible specific capacity of 293.8 mA h g^{-1} at 100 mA g^{-1}. In both studies, the role of S dopants was assigned to create defects in the carbon plane and provide additional active sites for K^+ adsorption.

Table 5 lists the structural properties and K^+-storage performance of recently reported carbon materials.

4.2 Batteries based on the anion-intercalation carbon cathode

In this section, we introduce the recent progress and achievement in energy devices based on anion-intercalation graphitic carbon cathodes (including DIBs and AIBs). DIBs are a general concept with both cations and anions involved in the electrochemistry[179] and they principally work in all electrolyte systems,[173] while AIBs refer to energy devices based on two different Al-containing anions ($AlCl_4^-$ and $Al_2Cl_7^-$).[170] We divide the discussion into separate parts according to the electrolyte systems. The electrochemistry, battery configuration, electrochemical performance, functions and remaining challenges are discussed in detail.

4.2.1 Li^+-based DIBs

(1) Intercalation-type anode//C batteries. Li^+-based DIBs are the most investigated systems among all DIBs due to their high compatibility with the infrastructure of LIBs. Simply replacing Li-rich transition metal oxide cathodes of LIBs (C//$LiMeO_x$) with graphitic carbon leads to dual-carbon or dual-graphite (C//C) batteries. The corresponding electrode reactions can be expressed as eqn (20) and (21). Exploiting graphitic carbon as both anode and cathode can largely reduce the cost of electrode materials and render C//C batteries with remarkable sustainability for scalable applications. The large potential gap between graphite cathode (4.2–4.7 V *vs.* Li^+/Li) and graphite anode (<0.2 V *vs.* Li^+/Li) affords a high working voltage of 4.0–4.5 V, which is superior to 3.7 V of the commercial LIBs. Even though proposed by McCullough[30] in 1989, the concept of C//C batteries was not well demonstrated before and most research work mainly concentrated on Li//graphite half cells.[130,372–374] Till 2007, Ishihara *et al.*[228] screened various carbon materials and found a correlation of electrochemical performance and crystallinity of graphitic carbon. By using a graphitic carbon with high crystallinity and a carbonate electrolyte (1 M $LiPF_6$ in EC/DMC), a rechargeable C//C battery with high capacity (90 mA h g^{-1}) and high rate capability (0.4–4 mA cm^{-2}) was, for the first time, demonstrated without describing cycling stability. The irreversible capacity in this system appeared to be quite high, leading to a relatively low CE (<64%). Read *et al.*[206] explored a high-voltage electrolyte based on a fluorinated solvent and additive (1.7 M $LiPF_6$ in FEC-EMC + 5 mM tris(hexafluoro-iso-propyl)phosphate), which can simultaneously enable Li^+ and PF_6^- intercalation into graphitic carbon with the formation of a protective SEI and sufficient oxidative stability (5.2 V *vs.* Li^+/Li). Specific capacities of 80 mA h g^{-1} and 330 mA h g^{-1} can be achieved on the MesoCarbon MicroBeads (MCMB) cathode and CGP graphite anode (CPreme from Conoco Phlillips) in this electrolyte in half cells. The C//C cell performed 50 cycles with a capacity retention of 70% and an average CE of ~97% (Fig. 25a). In addition to carbonate electrolytes, an IL electrolyte was also investigated for C//C batteries on account of its wide electrochemical voltage window and impressive safety properties. The addition of ethylene sulfite (ES) into the Pyr_{14}TFSI electrolyte contributed to the formation of SEI on the graphite anode and enhanced the capacity for $TFSI^-$ intercalation (50 → 97 mA h g^{-1}).[165,375] The final C//C cells showed a maximum capacity of 121 mA h g^{-1} at 10 mA g^{-1} and maintained a stable capacity of 50 mA h g^{-1} at 500 mA g^{-1} for 500 cycles.

$$\text{Cathode: } A^- + C_n \rightleftharpoons C_n{}^+A^- + e^- \quad (20)$$

$$\text{Anode: } Li^+ + C_n + e^- \rightleftharpoons C_n{}^-Li^+ \quad (21)$$

Compared to the above low-concentration (≤1 M) electrolyte systems, C//C batteries based on high-concentration electrolytes are more promising to achieve high device-level energy density.[374] In a $LiPF_6$/EMC electrolyte, the electrolyte concentration effect on Li^+ and PF_6^- intercalation into graphitic carbon was examined.[377] The optimal concentration was determined to be 3.1 M when balancing the capacity of the graphite cathode and anode. A prelithiated graphite anode was further used which contributed to the stable cycling performance of C//C cells at 25–70 °C. A high capacity of 90–105 mA h g^{-1} and an energy density of 95 W h kg^{-1} (170 W h L^{-1}) were achieved. C//C batteries based on high-concentration LiTFSI/carbonate electrolytes were also reported;[212] however, there have been concerns on anodic etching when most of the electrolyte is consumed during charging, as stated in Section 3.2.2.

Very recently, a special C//C battery was reported, where a composite graphite cathode (LiBr, LiCl and graphite), a modified graphite anode and a "water-in-bisalt" electrolyte were involved (Fig. 25b).[172] The highly concentrated aqueous electrolyte (21 mol kg^{-1} LiTFSI + 7 mol kg^{-1} LiOTf/water) played an essential role in this battery by providing high electrochemical oxidative stability up to 4.9 V (*vs.* Li^+/Li) and being immiscible with LiBr and LiCl in the cathode or formed Br_2 and BrCl, thus allowing Br^- and Cl^- to be oxidized to near-neutral states and intercalated into graphite. Note that such anion oxidation/intercalation reactions took place entirely inside the composite graphite cathode without anion uptake from the electrolyte. At the same time, Li^+ diffused from the composite cathode to the graphite anode, behaving like a rocking-chair LIB. Because no SEI could be formed on the graphite anode in this electrolyte, the graphite anode was protected by a highly fluorinated ether polymer gel. The resultant full cell delivered a stable capacity of 127 mA h g^{-1} based on anode/cathode mass at an average voltage of 4.1 V (at 0.2C). After 150 cycles, the capacity retention was around 74% with a high average CE of 99.8%. If the mass of the cathode, anode and electrolyte was all counted, an energy density of 304 W h kg^{-1} could still be reached. This value is an energy record for C//C batteries or DIBs, highlighting the advantages of the proposed conversion–intercalation chemistry. Nevertheless, the stability, scalability, compatibility and processability of such energy technology based on concentrated aqueous electrolytes remain to be enhanced before its commercial implementations.

Table 5 Comparison of recently reported carbon materials for K^+ storage

Type of carbon material	Specific surface area	Interlayer distance	Specific capacity	First-cycle CE	Cycling stability	Ref.
CNT sponge	93 $m^2 g^{-1}$	0.344–0.427 nm	1414 mA h g^{-1} at 100 mA g^{-1} 162 mA h g^{-1} at 1.6 A g^{-1}	15%	90% at 100 mA g^{-1} over 500 cycles	344
Graphitic carbon nanocages	102.7 $m^2 g^{-1}$	0.354 nm	221.5 mA h g^{-1} at 27.9 mA g^{-1} 175 mA h g^{-1} at 9.8 A g^{-1}	40%	95% at 56 mA g^{-1} over 100 cycles	345
N-Doped graphene	—	—	350 mA h g^{-1} at 50 mA g^{-1}	80%	78% at 100 mA g^{-1} over 100 cycles	161
S-Doped rGO	7.6 $m^2 g^{-1}$	—	435 mA h g^{-1} at 500 mA g^{-1} 224 mA h g^{-1} at 1 A g^{-1}	62%	76% at 1 A g^{-1} over 500 cycles	346
N-Doped CNTs	—	0.337–0.360 nm	324 mA h g^{-1} at 10 mA g^{-1} 75 mA h g^{-1} at 1 A g^{-1}	14.2%	76% at 20 mA g^{-1} over 100 cycles	347
CNT-modified graphitic carbon	57.2 $m^2 g^{-1}$	0.342–0.391 nm	229 mA h g^{-1} at 100 mA g^{-1} 180 mA h g^{-1} at 10 A g^{-1}	24%	98% at 100 mA g^{-1} over 800 cycles	348
Bacterial cellulose derived carbon	778.8 $m^2 g^{-1}$	0.370–0.390 nm	240 mA h g^{-1} at 50 mA g^{-1} 164 mA h g^{-1} at 1 A g^{-1}	—	88% at 10 A g^{-1} over 2000 cycles	349
N-Doped carbon	563 $m^2 g^{-1}$	—	250 mA h g^{-1} at 34 mA g^{-1} 156 mA h g^{-1} at 5 A g^{-1}	—	106% at 500 mA g^{-1} over 4000 cycles	351
Hard carbon	77 $m^2 g^{-1}$	0.382 nm	290 mA h g^{-1} at 25 mA g^{-1} 156 mA h g^{-1} at 5 A g^{-1}	81%	98% at 25 mA g^{-1} over 50 cycles	341
Potato derived carbon	532 $m^2 g^{-1}$	—	248 mA h g^{-1} at 100 mA g^{-1} 152 mA h g^{-1} at 1 A g^{-1}	43%	100% at 500 mA g^{-1} over 400 cycles	352
Pepper derived carbon	18.3 $m^2 g^{-1}$	0.386 nm	284 mA h g^{-1} at 28 mA g^{-1} 167 mA h g^{-1} at 279 mA g^{-1}	58%	71% at 140 mA g^{-1} over 300 cycles	353
Walnut septum derived N-doped carbon	99.6 $m^2 g^{-1}$	0.376 nm	305.7 mA h g^{-1} at 50 mA g^{-1} 102.6 mA h g^{-1} at 2 A g^{-1}	55.1%	78% at 1 A g^{-1} over 1000 cycles	354
Hollow multihole carbon bowls	425.1 $m^2 g^{-1}$	0.399 nm	377 mA h g^{-1} at 100 mA g^{-1} 182 mA h g^{-1} at 2 A g^{-1}	66%	81% at 100 mA g^{-1} over 150 cycles	355
N-Doped carbon nanofibers	153 $m^2 g^{-1}$	0.370 nm	220 mA h g^{-1} at 28 mA g^{-1} 110 mA h g^{-1} at 2.8 A g^{-1}	70%	79% at 279 mA g^{-1} over 1750 cycles	357
N-Doped hollow carbon	355.6 $m^2 g^{-1}$	0.371 nm	294 mA h g^{-1} at 100 mA g^{-1} 205 mA h g^{-1} at 2 A g^{-1}	15%	96% at 1 A g^{-1} over 1600 cycles	358
Carbon microspheres	65 $m^2 g^{-1}$	0.400 nm	262 mA h g^{-1} at 28 mA g^{-1} 130 mA h g^{-1} at 1.4 A g^{-1}	87%	83% at 28 mA g^{-1} over 100 cycles	359
Hollow carbon architecture	171 $m^2 g^{-1}$	0.356 nm	340 mA h g^{-1} at 28 mA g^{-1} 110 mA h g^{-1} at 560 mA g^{-1}	72.1%	100% at 140 mA g^{-1} over 150 cycles	356
N-Doped carbon nanofibers	99 $m^2 g^{-1}$	—	248 mA h g^{-1} at 25 mA g^{-1} 101 mA h g^{-1} at 20 A g^{-1}	49%	95% at 2 A g^{-1} over 4000 cycles	360
N-Doped porous carbon	326 $m^2 g^{-1}$	0.361 nm	349.4 mA h g^{-1} at 50 mA g^{-1} 193.1 mA h g^{-1} at 500 mA g^{-1}	30.3%	44% at 500 mA g^{-1} over 1000 cycles	361
ZIF-67 derived N-doped CNTs	126 $m^2 g^{-1}$	0.340 nm	297.2 mA h g^{-1} at 50 mA g^{-1} 131 mA h g^{-1} at 2 A g^{-1}	24%	78% at 2 A g^{-1} over 500 cycles	363
Zn-MOF/Co-MOF derived porous carbon	430 $m^2 g^{-1}$	0.338 nm	460 mA h g^{-1} at 100 mA g^{-1} 120 mA h g^{-1} at 5 A g^{-1}	15.7%	65% at 100 mA g^{-1} over 200 cycles	364
Mesoporous carbon	1089 $m^2 g^{-1}$	0.521 nm	286.4 mA h g^{-1} at 50 mA g^{-1} 144.2 mA h g^{-1} at 1 A g^{-1}	63.6%	70% at 1 A g^{-1} over 1000 cycles	80
N-Doped carbon nanosheets	54 $m^2 g^{-1}$	0.340 nm	440 mA h g^{-1} at 300 mA g^{-1} 170 mA h g^{-1} at 6 A g^{-1}	—	70% at 5 A g^{-1} over 3000 cycles	365
N-Doped porous carbon	341 $m^2 g^{-1}$	0.383 nm	420 mA h g^{-1} at 50 mA g^{-1} 185 mA h g^{-1} at 10 A g^{-1}	43.1%	88% at 1 A g^{-1} over 1000 cycles	366
Hollow carbon nanospheres	758 $m^2 g^{-1}$	0.379 nm	370 mA h g^{-1} at 200 mA g^{-1} 137 mA h g^{-1} at 4 A g^{-1}	44.2%	106% at 2 A g^{-1} over 5000 cycles	367
N,O-Doped hard carbon	1030 $m^2 g^{-1}$	0.45 nm	365 mA h g^{-1} at 25 mA g^{-1} 118 mA h g^{-1} at 3 A g^{-1}	25%	72% at 1.05 A g^{-1} over 1100 cycles	368
Wrinkled carbon tubes	290 $m^2 g^{-1}$	—	425 mA h g^{-1} at 50 mA g^{-1} 231 mA h g^{-1} at 2 A g^{-1}	45%	92.8% at 3 A g^{-1} over 2000 cycles	369
N-Doped carbon nanosheets	674 $m^2 g^{-1}$	0.369 nm	361 mA h g^{-1} at 50 mA g^{-1} 168 mA h g^{-1} at 2 A g^{-1}	20%	75.6% at 1 A g^{-1} over 1000 cycles	370
S,O-Doped porous carbon	983.2 $m^2 g^{-1}$	0.393 nm	225 mA h g^{-1} at 50 mA g^{-1} 158 mA h g^{-1} at 1 A g^{-1}	61.7	68% at 1 A g^{-1} over 2000 cycles	203
S,N-Doped hard carbon	109.8 $m^2 g^{-1}$	—	293.8 mA h g^{-1} at 100 mA g^{-1} 175 mA h g^{-1} at 3 A g^{-1}	35%	66% at 3 A g^{-1} over 1200 cycles	371
Pyridinic N-doped carbon	443 $m^2 g^{-1}$	0.346 nm	388 mA h g^{-1} at 500 mA g^{-1} 178 mA h g^{-1} at 5 A g^{-1}	57%	61.5% at 500 mA g^{-1} over 3000 cycles	158

For large-capacity applications, C//C pouch cells with capacities of 60–1600 mA h were assembled using low-cost expanded graphite and/or MCMB as active materials and dilute carbonate solutions (1 M $LiPF_6$) as electrolytes.[203,378] The full cell exhibited high cycling stability, a wide operation temperature (−20 to 100 °C) and low self-discharge. Due to the robust chemical stability of graphite, these carbon materials could be recycled for further battery use, which largely decreased the cost of C//C

batteries. At power densities of 48–584 W kg^{-1}, the device energy density ranged from 47.9 to 54.1 W h kg^{-1} (the overall battery mass). Although the obtained energy density is lower than that (100–200 W h kg^{-1}) of commercial LIBs, it is feasible to be promoted further by adopting concentrated electrolytes.

Potentially, C//C batteries can be symmetric batteries, which utilize the same active material as both anode and cathode. The main advantages of symmetric batteries lie in the largely simplified fabrication process, reduced manufacture cost[379] and switchable polarity, which endows full cells with high tolerance against accidental polarity mix-up and thus high safety property. Our group first investigated the polarity switchability of the graphite electrode between cathode and anode.[376] In a 2 M $LiPF_6$ electrolyte with 3 wt% vinylene carbonate (VC), an activation process was noticed on the graphite electrode during the polarity switch, which was attributed to SEI formation and/or expanded graphite edges. As a consequence, the resultant symmetric graphite battery could perform from both charge directions and could be reversibly switched multi times on polarity (Fig. 25c). In addition to the polarity switchability function, our group also explored the fast charge capability of dual-graphite cells. By using a pre-lithiated graphite anode from the above polarity-switch activation process, a dual-graphite cell was built, which achieved a high operating voltage, impressive cycling stability and rate performance. Specifically, the middle discharge voltage (V_m) was as high as 4.50 V. The capacity retention was 96% after 1400 cycles at 1 A g^{-1}. Additionally, the cell allowed fast charging within 30 s (10 A g^{-1}) with 80% capacity retained (Fig. 25d). Because of the unique faradaic pseudocapacitive anion intercalation behavior of the graphite cathode we discovered before,[221] we define such a dual-graphite system as a novel Li-ion pseudocapacitor,[163] which outperforms activated carbon (AC)-derived Li-ion capacitors (LICs) and metal oxide pseudocapacitors in energy density and power density.

Other than the graphitic carbon anode, intercalative metal oxides like $Li_4Ti_5O_{12}$,[380] TiO_2[381] and MoO_3[382] were additionally analyzed as the anode for DIBs. Different from the graphite anode with a low discharge voltage (0.1 V *vs.* Li^+/Li) and sluggish kinetics, the intercalative metal oxides mostly work above 1 V *vs.* Li^+/Li but show high rate performance, thus avoiding Li dendrite formation and affording long cycling life (up to 10 000 cycles) and fast charging capability of the full device. The drawback is the lower device voltage (V_m < 3.1 V) than that (V_m ~ 4.5 V) of C//C batteries.

(2) Alloy-type anode//C batteries. As an important family of anode materials for Li^+ storage, alloy-type anodes possess relatively low discharge potential (<0.4 V *vs.* Li^+/Li) but high capacities due to their alloy reaction mechanism. Two representative examples for alloy-type anodes are Al and Si; both are abundant on earth and promising for scalable applications. The theoretical capacities for Al and Si are 2235 mA h g^{-1} (Li_9Al_4)[384–386] and 3579 mA h g^{-1} ($Li_{15}Si_4$),[387] respectively. The alloy-type anode//C (Al//C as an example) batteries work under eqn (22) and (23). Tang *et al.*[383] first explored the use of the Al anode in DIBs with a battery configuration of Al//C (Fig. 26), where Al foil functioned as an anode and a current collector. Compared to C//C batteries, the Al//C batteries are simpler with respect to battery configuration. The VC additive was found to be effective in improving the cycling performance of the Al//C battery, which can be ascribed to VC-facilitated SEI formation

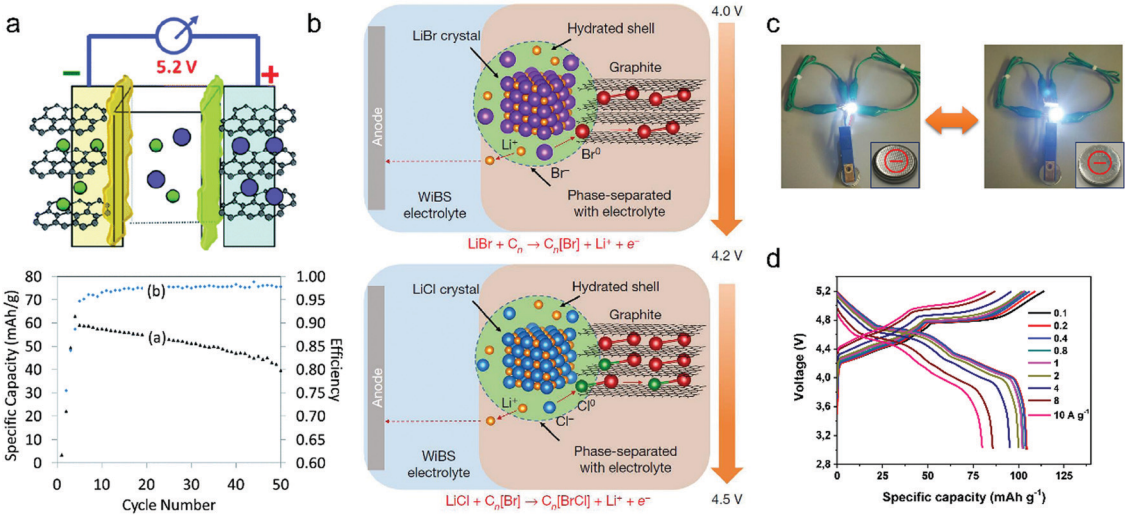

Fig. 25 (a) Schematic illustration of a dual-graphite intercalation cell and its electrochemical performance. Reproduced from ref. 206 with permission from The Royal Society of Chemistry. (b) Schematic of the conversion–intercalation mechanism occurring in the composite graphite cathode during its oxidation in the water-in-bisalt aqueous-gel electrolyte. The two-stage reactions involve the oxidation of Br^- (about 4.0 V) and Cl^- (about 4.2 V) and their subsequent intercalation into the graphitic structure. The discharge is a complete reversal of the charge process. Reproduced from ref. 172 with permission from Springer Nature. (c) Powering a white light-emitting diode by the polarity-switchable symmetric graphite battery from both directions. Reproduced from ref. 376 with permission from Wiley-VCH. (d) Rate performance of the Li-ion pseudocapacitor in a voltage window of 3–5.2 V. Reproduced from ref. 163 with permission from Wiley-VCH.

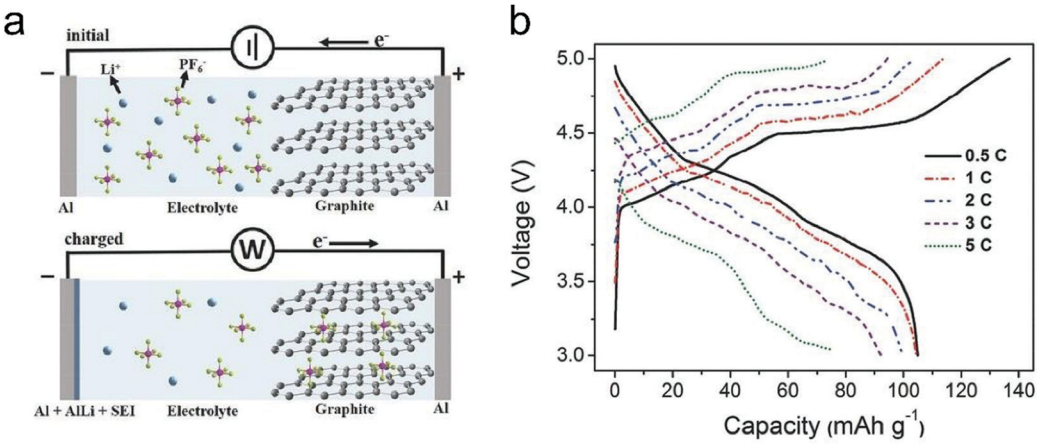

Fig. 26 (a) Schematic illustration of the Al-graphite DIB in the initial and the charged states. (b) Charge–discharge curves of the Al-graphite DIB under 0.5, 1, 2, 3, and 5C. 1C corresponds to 100 mA g^{-1}. Reproduced from ref. 383 with permission from Wiley-VCH.

of the Al anode. The final Al//C battery showed stable cycling performance at 0.5C with a V_m of 4.1 V, a high rate performance (1–5C) and a fair cycling life of 200 cycles. The formation of the AlLi alloy on the Al anode was confirmed in the half cells and full cells. To alleviate the pulverization of the Al anode during lithiation and delithiation, various Al anodes were constructed, like carbon-coated porous Al foil,[388] bubble-like Al/C,[389] 3D Al deposited on glass fiber,[390] modified Al foil[391] and core–shell Al@C.[392] The cycling life of Al//C batteries was successfully increased from <400 cycles to over 1000 cycles, and the rate capability was elevated to 20–120C. The remaining issue for Al//C batteries is the relatively low CE, especially at low current >rates (<80% at 1–2C), which indicates the involvement of significant irreversible side reactions and continuous consumption of the electrolyte. One possible reason is the growth of the SEI on the Al anode during large volume variation.

$$\text{Cathode: } A^- + C_n \rightleftharpoons C_n^+A^- + e^- \quad (22)$$

$$\text{Anode: } Li^+ + Al + e^- \rightleftharpoons Al_x^-Li^+ \quad (23)$$

Si, another high-capacity alloy-type anode, was also exploited as the anode in DIBs. To accommodate the volume expansion and enhance the electrical conductivity of Si, a composite Si@graphene was fabricated.[393] The Si@graphene//C cells show a V_m of 4 V as well as stable cycling and rate performance. During cycling, the CE quickly increased from 73.5% (for the 1st cycle) to >90%. After 1000 cycles, 83% capacity was retained with a high CE of 98.5%. In another case, Si was prelithiated before assembly into the full cells.[393] The optimal voltage window of Si//C batteries locates at 3–5 V with a balanced cycling stability and CE.

(3) Conversion-type or adsorption-type anode//C batteries. Conversion-type (WS_2, $MnSiO_3$)[394,395] or adsorption-type anode (AC)[396] materials also can be used in Li^+-based DIBs. The electrode reactions in the WS_2//C battery are shown as eqn (24) and (25). Since the working potential of these anodes was much higher (1.75 V *vs.* Li^+/Li) than that of the graphite anode, the fabricated full cells show a limited V_m of ≤2 V. The irreversibility of the conversion-type anode generally will lead to huge polarization of full cells, giving rise to low energy efficiency.

$$\text{Cathode: } A^- + C_n \rightleftharpoons C_n^+A^- + e^- \quad (24)$$

$$\text{Anode: } Li^+ + 1/4WS_2 + e^- \rightleftharpoons 1/4W + 1/2Li_2S \quad (25)$$

4.2.2 Na^+-based DIBs

(1) "Adsorption + intercalation"-type anode//C batteries. Due to the special chemical bonding change during the formation of Na^+-GICs, pure Na^+ intercalation into graphite encountered thermodynamic problems, leading to very limited capacity (12–35 mA h g^{-1}).[43] Alternatively, soft carbon and hard carbon[398] containing crystalline graphitic domains but with much lower stacking order than graphite were applied as the anode materials for Na^+-based DIBs and an "adsorption + insertion" mechanism was associated with soft carbon and hard carbon anodes. A soft carbon prepared by thermal polymerization of an organic compound showed a trace amount of oxygen (1.4%) and an interlayer distance of 0.39 nm.[399] A high D band was noticed from Raman spectroscopy, indicating its high structural disorder. For Na storage, the soft carbon exhibited good rate capability and stable cycling performance (400 cycles) in half cells. Owing to the high working potential of soft carbon (0–1 V *vs.* Na^+/Na), the soft carbon//C full cell exhibited a moderate V_m of 3.58 V in a dilute $NaPF_6$/EC-DMC (1 M) electrolyte. In the voltage window of 2–4.7 V, the full cells delivered a maximum capacity of 103 mA h g^{-1} on soft carbon mass (52 mA h g^{-1} on graphite mass) and high capacity retention after 800 cycles. The capacity of full cells decayed much (from 100 to 56 mA h g^{-1}) when elevating the current rate (from 200 to 1000 mA g^{-1}). No typical three-region charge–discharge curve was noticed for the soft carbon//C cells, indicating incomplete utilization of the graphite cathode. Hard carbon from biomass (pine needles) was also fabricated, which showed a reversible capacity of 180 mA h g^{-1} for Na^+ storage.[400] The resultant hard carbon//C full cell in a dilute $NaPF_6$/EC–EMC (1 M) electrolyte possessed a high V_m of 4.1 V (0.8–4.7 V) and long cycling life (87.2% capacity retention after 1000 cycles). By using PC as the

electrolyte solvent (0.8 M $NaPF_6$/PC), the V_m of hard carbon//C batteries can be increased to 4.3 V in a voltage window of 1.5–4.9 V.[401]

A nonflammable hard carbon//C battery based on NaTFSI was reported,[397] which was enabled by the addition of nonflammable trimethyl phosphate (TMP). At a molar ratio of 1 : 2 (NaTFSI/TMP), the graphite cathode can form a stage-II GIC during $TFSI^-$ intercalation, while a stable SEI is formed on the hard carbon anode. The final hard carbon//C cell is capable of providing a V_m of 4.0 V and excellent electrochemical performance (Fig. 27a and b). However, the capacity of the hard carbon//C cell (46.6 mA h g^{-1} on graphite mass) is relatively low at the current stage, and further optimization of battery configuration may be needed. Besides soft carbon and hard carbon, our group recently demonstrated a dual-graphene Na^+-based DIB.[402] The electrochemically exfoliated graphene (EG) can reversibly store PF_6^- and Na^+, endowing dual-graphite batteries with a 4.0 V working voltage. On account of the high processability of EG and the symmetric electrode feature, the dual-graphene battery can be readily printed for various miniaturized applications.

Other intercalation- or insertion-type Na^+ hosts such as $Na_2Ti_3O_7$,[403] $FePO_4$[404] and $FeFe(CN)_6$[405] also find applications in DIBs. In the dilute carbonate and IL electrolyte ($\leq$1 M), the full cells performed in the voltage range of 0–3.5 V, 1.2–4.2 V and 0.1–1.6 V and outputted a low V_m of 2.5 V, 2.3 V and 1.1 V, respectively.

(2) Alloy-type anode//C batteries. Sn, a conventional alloy type anode for LIBs, was studied as the Na host for DIBs. Theoretically, Sn can deliver a capacity of 847 mA h g^{-1} with a stoichiometry of $Na_{15}Sn_4$ and three intermediate phases ($NaSn_5$, NaSn and Na_9Sn_4) exist.[406] To enable Sn//C batteries, a dilute carbonate electrolyte (1 M $NaPF_6$ in EC–DMC–EMC)[197] was prepared, where EC plays a role in dissolving sodium salt and forming the SEI. The Sn foil//C cells operating under eqn (26) and (27) displayed a reversible capacity of 74 mA h g^{-1} at 2C over a voltage window of 2–4.8 V (Fig. 27c and d) and stable cycling performance with 94% capacity retained after 400 cycles. In spite of a relatively low V_m of 3.75 V than 4.0–4.3 V for hard carbon//C cells, Sn//C cells feature a simplified battery configuration and a few inactive components. As confirmed by XRD results, NaSn was formed during charging Sn//C cells. Compared to other alloy-type anodes (Pb and Sb), the full cells made from the Sn anode showed the highest reversible capacity, indicating the highest reactivity of Sn. To further push forward the electrochemical performance of Sn//C cells, a hybrid electrolyte ($LiPF_6$ + $NaPF_6$) was applied.[407] The presence of more active Li^+ (compared to Na^+) in the electrolyte largely reduces the charge transfer resistance, eventually enhancing the rate capability (5C → 30C). The V_m of Sn//C cells was increased by 4.0 V due to the low reaction potential of LiSn.

$$\text{Cathode: } PF_6^- + C_n \rightleftharpoons C_n^+PF_6^- + e^- \quad (26)$$

$$\text{Anode: } Na^+ + Sn + e^- \rightleftharpoons Na + Sn^- \quad (27)$$

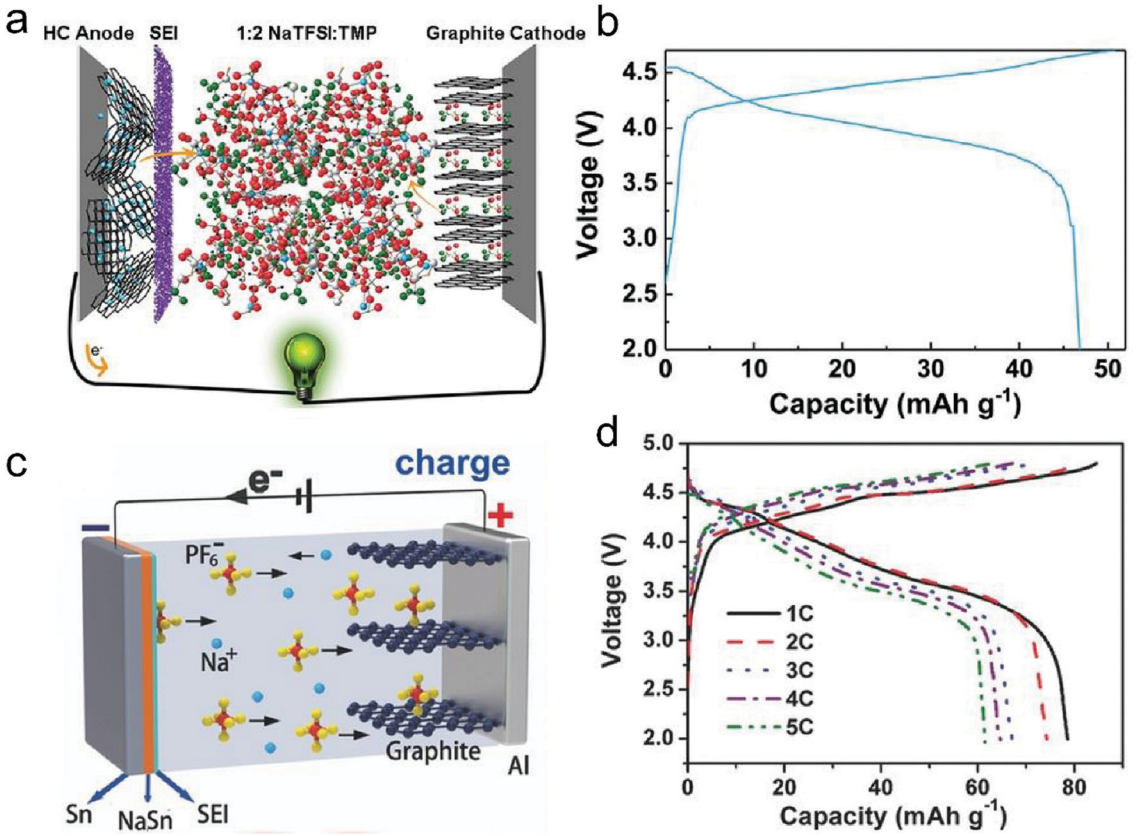

Fig. 27 (a) Schematic illustration and (b) typical charge–discharge curves of Na^+-dual carbon batteries using a 1 : 2 NaTFSI : TMP electrolyte at 500 mA g^{-1}. Reproduced from ref. 397 with permission from Wiley-VCH. (c) Schematic illustration of the working mechanism and (d) charge–discharge curves of a Sn//C DIB at various current rates from 1 to 5C. Reproduced from ref. 197 with permission from Wiley-VCH.

(3) Conversion-type anode//C batteries. As a high-capacity conversion-type anode, MoS_2 was used to build MoS_2//C Na^+-based DIBs.[198,408] In the voltage windows of 1.0–4.0 V and 1.0–4.5 V, the MoS_2//C cells exhibited a cycling life of 200–500 cycles but suffered from polarization problems. The charge–discharge separation exceeded 1–2 V and no obvious charge–discharge plateaus appeared.

4.2.3 K^+-based DIBs

(1) Intercalation-type anode//C batteries. Although the ionic radius of K^+ (1.38 Å) is bigger than that (1.02 Å) of Na^+,[43] K^+ intercalation into graphite is thermodynamically favorable, leading to a theoretical capacity of 279 mA h g^{-1} (KC_8). C//C batteries in K^+-based electrolytes have been demonstrated by different groups since 2017.[200,409–411] A carbonate solution with 0.8–1 M KPF_6 was applied as the electrolyte; EC was indispensable for its high solvation ability and SEI formation. The assembled C//C batteries showed a reversible capacity of 62 mA h g^{-1} (on anode mass; 31–41 mA h g^{-1} on cathode mass) in the voltage range of 3.0–5.0 V.[410] A medium V_m of 3.96 V was achieved. Based on the charge–discharge curves and XRD data, the stage number of the charged graphite cathode in the K electrolyte is higher than stage-II, suggesting that the graphite cathode was not fully utilized. By expanding the voltage window to 3.0–5.2 V,[200] the capacity of C//C batteries was enhanced to 61 mA h g^{-1} (based on the mass of the graphite cathode), and the V_m of C//C batteries was successfully increased by 4.5 V, which is comparable to that of C//C batteries in Li electrolytes. The remaining challenges for C//C batteries are further elevating the CE (>80%) and long-term cycling stability. The C//C cells were further built in K^+-based IL electrolytes (0.3 M KTFSI in Pyr_{14}TFSI) with 2 wt% ES.[409] Eqn (28) and (29) shows the electrochemical reaction of each electrode during cell operation. The electrochemical performance of the graphite anode and cathode was systematically investigated, where stage-I K^+-GIC and >stage-II $TFSI^-$-GIC were realized at 0.01–1.5 V and 3.4–5.0 V (*vs.* K^+/K). The reversible capacities of the graphite anode and cathode stabilized around 230 and 45 mA h g^{-1} (at 50 mA g^{-1}) with an average CE of 97%. Regarding the full cells, a stable capacity of 42 mA h g^{-1} and a long cycling life of 1500 cycles (95% capacity retention) were attained.

$$\text{Cathode: } TFSI^- + C_n \rightleftharpoons C_n{}^+TFSI^- + e^- \quad (28)$$

$$\text{Anode: } K^+ + C_8 + e^- \rightleftharpoons K^+C_8{}^- \quad (29)$$

(2) K//C batteries. For DIBs, the electrolyte containing active charge carriers (cations and anions) should be considered as the active material when calculating device-level energy density. The lower the concentration of the electrolyte, the more inactive the solvent involved, thus leading to low energy density of DIBs. The limited solubility of potassium salts in carbonates ($NaPF_6$) and ILs (KTFSI) severely hinders the energy enhancement of K^+-based DIBs. To address this problem, a concentrated KFSI electrolyte (5 M) was prepared in EC/DMC,[167] where stage-I FSI^--GIC was formed when the graphite cathode was fully charged to 5.25 V *vs.* K^+/K. On pairing the graphite cathode with a thin K foil anode, the K//C cells delivered a specific capacity of 98 mA h g^{-1}, an average discharge voltage of 4.7 V and a cycling life of 300 cycles (Fig. 28). A high energy density of 207 W h kg^{-1} was claimed based on the mass of the graphite cathode and electrolyte. Due to the low ionic diffusion of the concentrated electrolyte, the rate capability of K//C cells was reasonable; around half capacity can be retained when the current was elevated from 0.05 to 0.5 A g^{-1} (Fig. 28c). The CE of K//C cells was found to decrease along with cycles from 99% to 93% (Fig. 28d), which was attributed to anodic corrosion even though a stable TiN coated current collector was employed. Anodic etching associated with corrosive anions remains a concern in DIBs, especially under lean electrolytes at the charged states. Note that K metal was used in this case; the dendrite formation issue of the K metal in carbonate electrolytes should be well deliberated in case of potential safety concerns.

(3) Alloy-type anode//C batteries. Sn can be applied as a host for K^+ storage other than Na^+ storage. Using a similar work methodology to Sn//C Na^+-based DIBs, a Sn//C K^+-based DIB was reported,[201] where 1 M KPF_6 in EC–DMC–EMC was adopted as the electrolyte. The Sn//C cell gave a reversible capacity of 66 mA h g^{-1} (at 50 mA g^{-1}) at 3.0–5.0 V and a V_m of 4.25 V, and it exhibited high cycling stability with 93% capacity retention after 300 cycles. To confirm the phase composition of the K–Sn alloy, four phases KSn_4, KSn_2, KSn and K_2Sn were formed in the half cell while only K_2Sn was noticed in the charged Sn//C DIB.

(4) Adsorption-type anode//C batteries. Regarding K^+ storage kinetics, the adsorption-type anode possesses intrinsically fast rate capability than intercalation-type and alloy-type anodes, and thus the adsorption-type anode is appealing to construct high-power DIBs. Hierarchical porous carbon from pyrolysis of biomass and KOH activation manifested a high surface area of up to 3300 m^2 g^{-1},[412] leading to a stable capacity of 60.7–63 mA h g^{-1} independent of current density (0.5–3 A g^{-1}). The final porous carbon//C hybrid cell displays very stable capacity up to 3 A g^{-1} and long-term cycling stability (74.2% capacity retention after 2000 cycles at 1 A g^{-1}). Due to the high working potential (1–3 V *vs.* K^+/K) of hierarchical porous carbon, the full hybrid cell works in a downshifted voltage window of 1.0–3.75 V with a V_m of 3.2 V.

4.2.4 $Al_2Cl_7{}^-$-based batteries.

Al, the most abundant metallic element in the earth's crust (8.13%), has been considered as an intriguing anode material for its low cost, high safety against water/moisture, relatively low redox potential at −1.66 V (*vs.* SHE) and high volumetric capacity up to 8035 mA h cm^{-3}. Although rechargeable Al batteries have been explored over 30 years, short cell life, fast performance fading and low cell voltage issues were not well addressed before.[101,413–415] In 2015, a graphene foam-based AIB was first reported in an $AlCl_3$/EMImCl electrolyte with Al foil as the anode (Fig. 29a).[170] The resultant AIB performs according to eqn (30) and (31)

$$\text{Cathode: } AlCl_4{}^- + C_n \rightleftharpoons C_n{}^+AlCl_4{}^- + e^- \quad (30)$$

$$\text{Anode: } 4Al_2Cl_7{}^- + 3e^- \rightleftharpoons Al + 7AlCl_4{}^- \quad (31)$$

Mixing solid $AlCl_3$ and EMImCl produces a liquid at room temperature, which can be attributed to the acid–base reaction

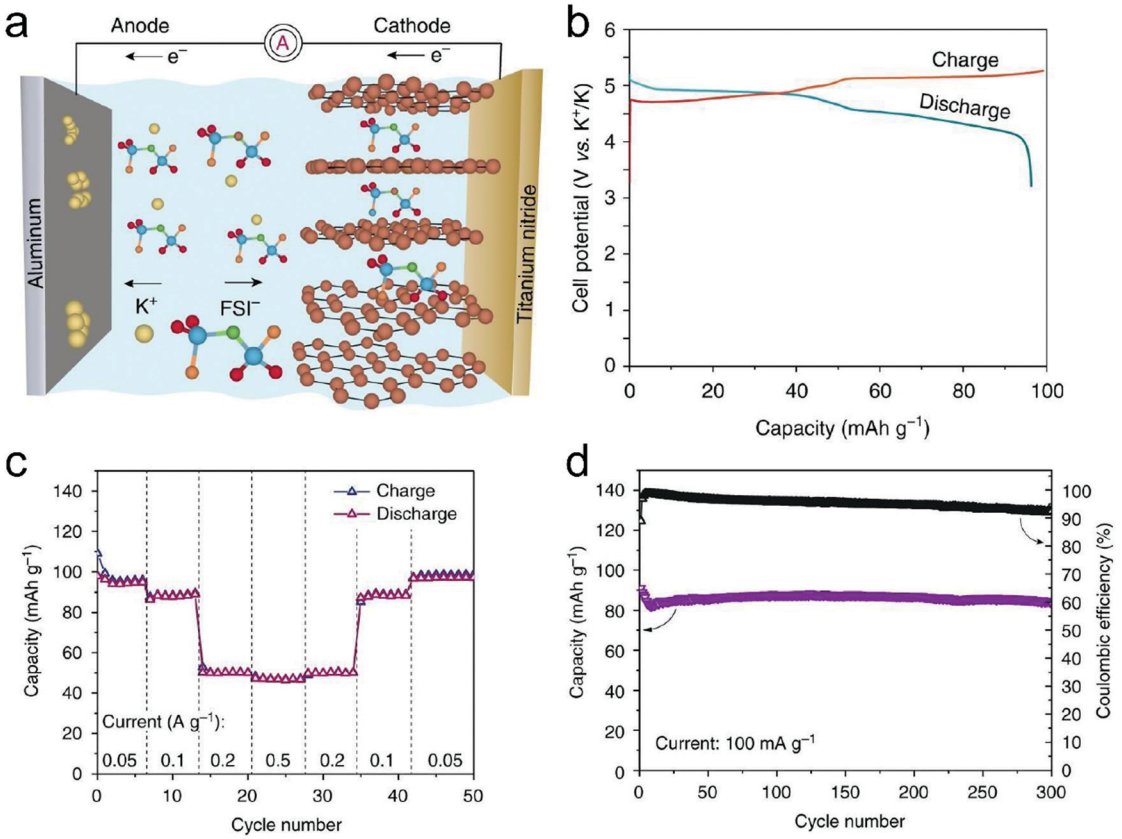

Fig. 28 (a) Schematic of the charging process in a K//C DIB. Fluorine, oxygen, sulfur, and nitrogen atoms in the FSI^- anion are shown in brown, red, blue, and green colors, respectively. (b) Typical galvanostatic voltage profile of a K//C DIB measured at a current density of 50 mA g^{-1}. (c) Rate capability measurements and (d) cycling performance of a K//C DIB. Reproduced from ref. 167 with permission from Springer Nature.

between these two compounds. The ratio of $AlCl_3$/EMImCl is a key parameter that determines the chemical composition of the electrolyte and the electrochemical performance of the AIB. Only when the ratio exceeds 1 : 1, there is $Al_2Cl_7^-$ formed in the acidic IL, which enables Al electroplating and thus an AIB. During charging, $Al_2Cl_7^-$ in the electrolyte was consumed and Al was deposited on the anode, while $AlCl_4^-$ was intercalated into graphitic carbon cathodes. The maximum ratio of $AlCl_3$/EMImCl is 2 : 1, beyond which, $AlCl_3$ did not dissolve in the IL. It was revealed that a high-ratio $AlCl_3$/EMImCl electrolyte led to a declined onset voltage of the AIB,[214] and the maximum capacity was obtained at an optimal ratio of 1.3 : 1.[170] The resultant Al// graphene-foam AIB exhibited a reversible capacity of 66 mA h g^{-1} and well-defined discharge plateaus at 2 V (Fig. 29b). The AIB could even operate at 4 A g^{-1} (<1 min charge/discharge) for 7500 cycles without capacity fading. The CE stabilizes at 90% at 100 mA g^{-1} and approaches 98% at high current rates (5 A g^{-1}; Fig. 29c).

To further boost the capacity and rate capability of AIBs, various graphitic carbons with higher GD[189,214,416,417] and rationally designed interlayer spacing/porous structure[97,169,234,240,418,419] were adopted. The capacity was increased to 110–150 mA h g^{-1} and the current rate can be as high as 400 A g^{-1} [169] at low mass loading. As Al plating/stripping takes place on the anode side of AIBs, the Al anode can be replaced by any other substrate that facilitates reversible electroplating of Al. C//C AIBs have been demonstrated recently.[29,420] For large capacity application, an industrialized prototype AIB with a capacity of 1.3 A h was assembled using a carbon paper cathode and Al foil.[421] The Ah-level AIB exhibited stable cycling performance at 10 mA g^{-1} for over 100 cycles with a CE of 93%. The capacity of AIBs decreased to 0.73 Ah at an elevated current density of 40 mA g^{-1}. The self-discharge rate of the AIB was estimated to be 5.89–7.23% per day. It is important to note that, after 120 cycles, the carbon paper turned into thin-layer graphene due to expansion and exfoliation of the graphite cathode. Similar large expansion of the graphite cathode was noticed before.[170] It appears that currently only $AlCl_4^-$ intercalation into graphite causes exfoliation of graphite, which is rarely reported in other anion systems (PF_6^-, $TFSI^-$, $FTFSI^-$, FSI^-, BF_4^- and $Br^{-0.05}Cl^{-0.25}$). The large d_i may be the main reason (Table 1). Owing to the use of IL electrolytes, the AIBs show impressive electrochemical performance under extreme conditions; the AIBs can survive the drill experiment during battery operation[170] and even heating under an alcohol lamp.[234] The broad liquid range of IL electrolytes further makes AIBs capable of performing within a wide temperature range of −40 to 120 °C (Fig. 29d and e),[169] which is suitable for all-climate energy storage applications.

To reduce the cost of IL electrolytes for AIBs, new electrolyte systems including $AlCl_3$–urea[190,422] $AlCl_3$–urea–[EMIm]Cl,[423] $AlCl_3/Et_3NHCl$[424] and inorganic molten salts ($AlCl_3$–NaCl,[425]

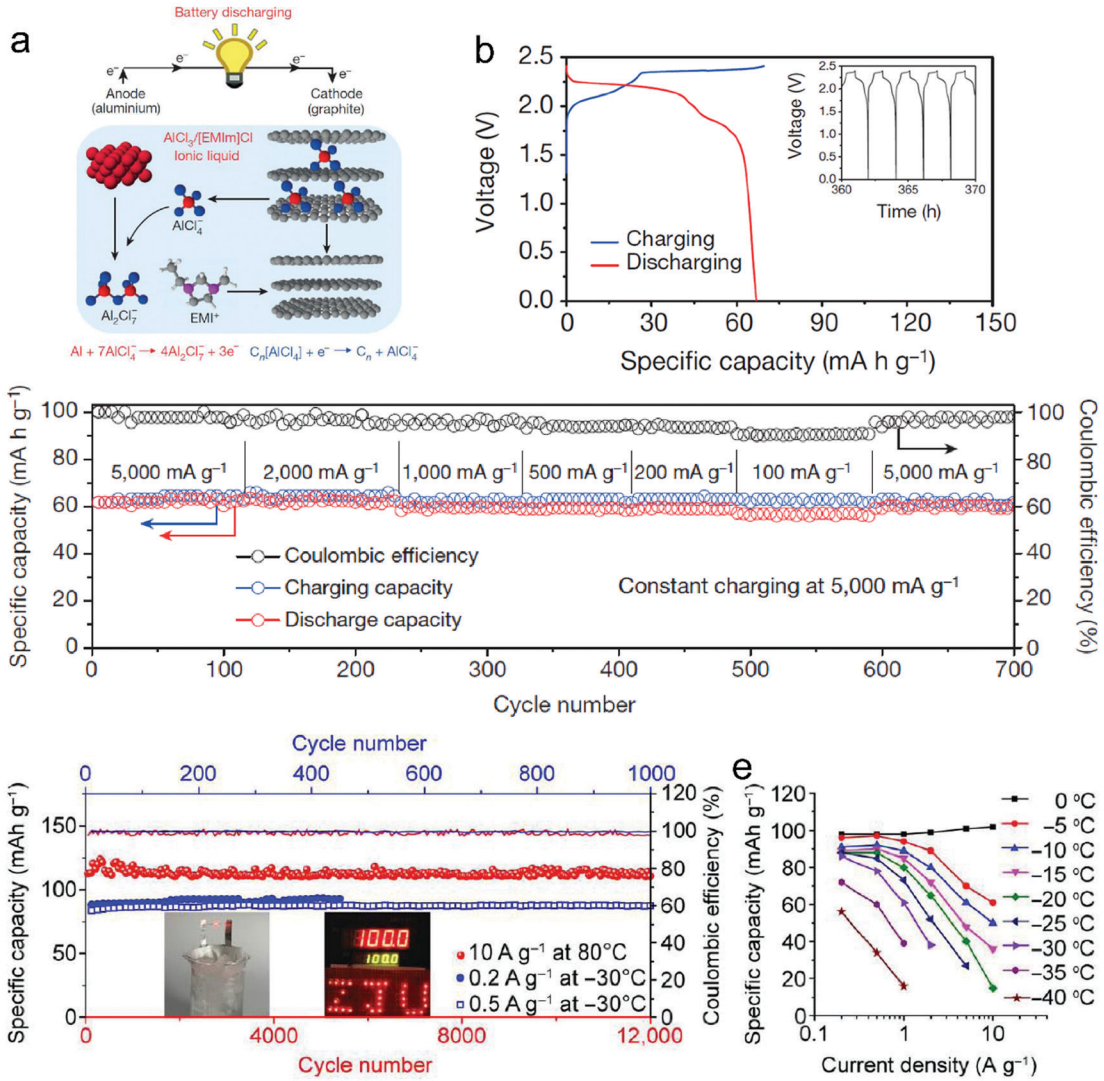

Fig. 29 (a) Schematic drawing of the Al/graphite cell during discharge, using the optimal composition of the $AlCl_3$/EMImCl IL electrolyte. (b) Galvanostatic charge and discharge curves of an Al/pyrolytic graphite (PG) Swagelok cell at a current density of 66 mA g^{-1}. Inset, charge and discharge cycles. (c) An Al/graphitic-foam pouch cell charging at 5000 mA g^{-1} and discharging at current densities ranging from 100 to 5000 mA g^{-1}. Reproduced from ref. 170 with permission from Springer Nature. (d) Stable cycling of the GF-HC cathode at 80 °C (red, 12 000 cycles) and −30 °C (blue, 1000 cycles). Inset: Al-GB soft pack cells successfully igniting LED lights in an ice-salt bath and a 100 °C oven. (e) Summary of specific capacities and rate capability of the GF-HC cathode at different temperatures below 0 °C. Reproduced from ref. 169 with permission from AAAS.

$AlCl_3$–NaCl–KCl[191] and $AlCl_3$–LiCl–KCl[426]) are explored. The AIB based on the $AlCl_3$–urea electrolyte[190] displays a V_m of 1.73 V (*vs.* 2 V in $AlCl_3$/EMImCl) and a specific capacity of 73 mA h g^{-1} at 100 mA g^{-1}. Correspondingly, a stage-II $AlCl_4^-$-GIC was achieved when fully charged. Al deposition proceeded through two pathways, one involving $Al_2Cl_7^-$ and the other involving $[AlCl_2{\cdot}(urea)_n]^+$. The ionic conductivity remained to be further promoted due to high viscosity. In the $AlCl_3$–urea electrolyte at 120 °C, it is found that the capacity of the AIB was enhanced to 93 mA h g^{-1} with improved rate capability.[422] Another room temperature $AlCl_3$/Et_3NHCl electrolyte led to a high upper cut-off voltage of 2.62 V. The Al//rGO AIB exhibited a high capacity of 112 mA h g^{-1}, a V_m of 1.9 V and a long lifespan (30 000 cycles).[424] In the inorganic molten electrolytes, the graphite-derived AIBs operated at 95–120 °C delivered capacities of 100–128 mA h g^{-1} and a V_m of 1.35–1.75 V.

Similar to DIBs, all the active charge carriers ($Al_2Cl_7^-$ and $AlCl_4^-$) of AIBs are initially stored in the IL electrolyte. So the energy density of AIBs strongly depends on the electrolyte. Taking the $AlCl_3$/EMImCl electrolyte as an example, the ratio of $AlCl_3$/EMImCl predetermines the content of $Al_2Cl_7^-$ in the electrolyte. Assuming a V_m of 2 V and a graphitic capacity of 140 mA h g^{-1}, the energy density of the Al//C AIB based on the mass of the electrolyte and graphite cathode was maximized (72 W h kg^{-1}) at the ratio of 2 : 1 and was around 33 W h kg^{-1} at 1.3 : 1. Note that most AIBs run at the ratio of 1.3 : 1, and the low energy density is currently the key challenge for AIBs.

4.2.5 Ca^{2+}-based DIBs. As the third most abundant metallic element (3.63%) in the earth's crust, Ca is a very attractive alternative to Li because of its stable valence states, small ionic size (1.00 Å) and low redox potentials (−2.89 V *vs.* SHE).[427] The

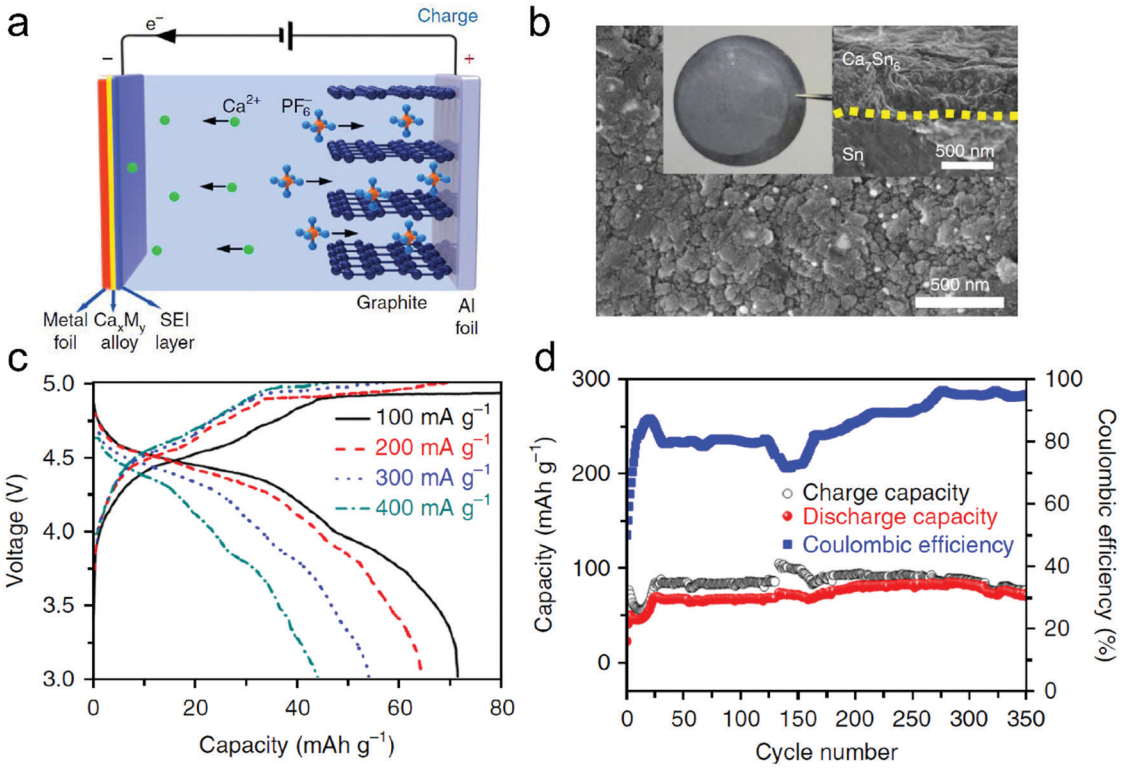

Fig. 30 (a) Work schematics of the proposed Sn//C cell. Graphite was used as the cathode material for PF_6^- intercalation/deintercalation, and a metal foil that could form an alloy with Ca was used as both current collector and anode. The green, blue and orange balls represent Ca, F and P atoms, respectively. (b) SEM images of the Sn foil anode after 300 cycles. The dashed yellow line shows the interface between Sn and Ca_7Sn_6. (c) Charge–discharge performance at different current densities ranging from 100 to 400 mA g^{-1} and (d) cycling stability of the Sn//C cell at 100 mA g^{-1}. Reproduced from ref. 202 with permission from Springer Nature.

first Ca^{2+}-based DIB was reported by Tang's group in 2018 (Fig. 30a),[202] where Sn foil functions as an alloy-type anode and graphite as the cathode (eqn (32) and (33)) in a Ca^{2+}-containing carbonate electrolyte (0.8 M $Ca(PF_6)_2$ in EC–PC–DMC–EMC). As confirmed by XRD, the Ca_7Sn_6 alloy was formed in the charged DIB. A SEI consisting of CaF_2 and other organic compounds was also detected on the Sn anode (Fig. 30b). The reversible alloying process of Sn offers a theoretical capacity of 526 mA h g^{-1} with a volume expansion of 137%. Correspondingly, compressive stress up to −48.13 MPa builds during the charging process. At room temperature, the full Sn//C cell delivers a reversible capacity of 70–85 mA h g^{-1} in a voltage window of 3.0–5.0 V and outputs a high V_m of 4.08–4.45 V as well as a cycling life of 300 cycles (Fig. 30c and d). To enhance the electrochemical kinetics, a hybrid electrolyte ($LiPF_6$ and $Ca(PF_6)_2$) was used.[428] The full cell works efficiently even at 15C and delivers a long cycle life of 1500 cycles.

$$\text{Cathode: } PF_6^- + C_n \rightleftharpoons C_n^+PF_6^- + e^- \quad (32)$$

$$\text{Anode: } 7Ca^{2+} + 6Sn + 14e^- \rightleftharpoons Ca_7^{2+}Sn_6^{2.33-} \quad (33)$$

Further, a Ca^{2+}-based DIB with a dual-graphite configuration[429] was constructed. Conventional MCMB was applied as the anode to host Ca^{2+} in the carbonate electrolyte (0.7 M $Ca(PF_6)_2$ in EC–DMC–EMC). During charging, the (002) peak of pristine graphite shifted from 26.3° to 25.9°, and a profound Ca signal was noticed in the charged MCMB anode. Based on these results, the authors concluded that Ca^{2+} was intercalated into MCMB. Thoroughgoing characterization of the Ca^{2+}-GIC is highly recommended due to the fact that no electrochemical intercalation of pure Ca^{2+} into the graphite host has been reported so far and Ca^{2+}/solvent co-intercalation[430] has been just revealed in a 0.5 M $Ca(BH_4)_2$ dimethylacetamide electrolyte very recently.

4.2.6 Zn^{2+}-based DIBs. Zn has been regarded as a promising anode material for next-generation batteries due to its high volumetric capacity (5800 mA h cm^{-3}), high safety against water/moisture and low cost, propelling the recent prosperity of Zn batteries.[432–436] Pairing Zn with the graphite cathode holds great potential to construct Zn//graphite batteries for stationary applications on account of their natural abundance, sustainability and cost-efficiency. The Zn//graphite cell was first tried in an IL electrolyte [0.2 M zinc trifluoromethanesulfonate ($Zn(TfO)_2$) in 1-ethyl-3-methylimidazolium trifluoromethanesulfonate (EMImTfO)].[437] Although IL solvent was used, the anodic oxidation occurs at >2.5 V (*vs.* Zn^{2+}/Zn), leading to a fast fading cycling performance of Zn//C batteries. After only 100 cycles, the capacity decayed to 20 mA h g^{-1}. Another IL electrolyte comprising of 1 M $Zn(TFSI)_2$ in $Pyr_{14}TFSI$ and 2 wt% ES was tried again for Zn//C cells.[438] The onset potential of anodic oxidation was estimated to be 2.6 V (*vs.* Zn^{2+}/Zn), restricting the working voltage of Zn//C cells. The resultant Zn//C cell delivered a limited capacity of 57 mA h g^{-1}, which is around half of the maximum

value of the graphite cathode. It suggests that the graphite cathode is not fully utilized due to the low upper voltage.

To get rid of anodic oxidation and make full use of the graphite cathode, our group recently developed a hybrid carbonate electrolyte (EMC) containing $Zn(TFSI)_2$ and $LiPF_6$.[431] The presence of $LiPF_6$ efficiently suppresses the anodic oxidation of $Zn(TFSI)_2$ and leads to a super-wide electrochemical stability window of 4 V (*vs.* Zn^{2+}/Zn), which is much higher than those of the above two IL electrolytes. Nuclear magnetic resonance (NMR) spectroscopy measurements indicates that PF_6^- diffuses faster than $TFSI^-$ in the hybrid electrolyte, thus protecting the current collector from anodic oxidation by the formation of a PF_6^--derived passivation film. Both dendrite-free Zn plating/stripping and reversible dual-anion ($TFSI^-$ and PF_6^-) intercalation are realized in the hybrid electrolyte. And the formation of stage-I $TFSI^-/PF_6^-$-GIC was confirmed by XRD, NMR and XPS results. The electrode reactions can be summarized as eqn (34) and (35).

$$\text{Cathode: } PF_6^- + TFSI^- + C_n \rightleftharpoons C_n^{2+}(PF_6^-)(TFSI^-) + 2e^- \quad (34)$$

$$\text{Anode: } Zn^{2+} + 2e^- \rightleftharpoons Zn \quad (35)$$

Regarding the electrochemical performance, the Zn//C cell performs in a wide voltage range of 0.7–2.8 V and outputs a record V_m of 2.2 V among all the Zn batteries (Fig. 31a and b). The reversible capacity reaches 105 mA h g^{-1} at 100 mA g^{-1} and retains 97.5% even after 2000 cycles at 1 A g^{-1} (Fig. 31c and d). The CE of the Zn//C cell approaches 100%, indicating high reversibility and no side reactions (anodic oxidation). In addition, the areal capacity of the Zn//C cell can be readily increased to 2 mA h cm^{-2} by enhancing the loading of the graphite cathode. Our hybrid electrolyte strategy provides a solid yet practical solution to the frequently encountered anodic oxidation problems in DIBs, which may inspire future development of novel metal-graphite batteries and other high-energy rechargeable batteries.

4.2.7 Non-metal cation-based DIBs. Besides metal cation systems mentioned above, non-metal cations can also be used to construct DIBs.

(1) Intercalation-type anode//C batteries. As early as 1994, Carlin *et al.*[440] proposed dual-intercalating IL batteries with room-temperature or low-temperature ILs as the only electrolytes. ILs consist of active charge carriers (cations and anions), and no additional salt or solvent is needed. They investigated various ILs including $EMIm^+$, 1,2-dimethyl-3-propylimidazolium cations ($DMPI^+$), $AlCl_4^-$, PF_6^-, $CF_3SO_3^-$ and $C_6H_5CO_2^-$. Reversible $DMPI^+$ intercalation into graphite was evidenced by CV and charge–discharge curves. The dual-graphite cell employing the $DMPI^+AlCl_4^-$ electrolyte showed a V_m of 2.9 V and a cycling

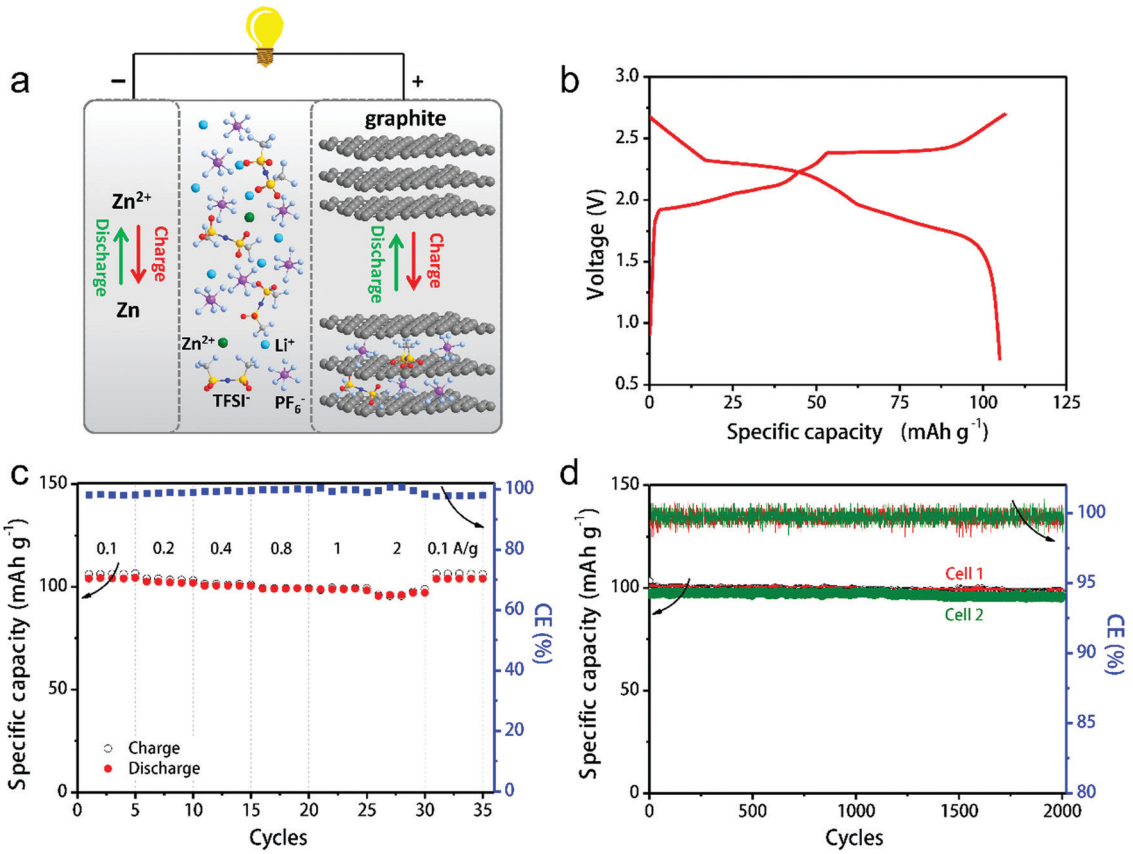

Fig. 31 (a) Schematic illustration of the Zn-graphite battery configuration and electrode reactions. (b) Typical charge–discharge curve at 100 mA g^{-1}, (c) rate capability and (d) cycling performance of the Zn-graphite battery at 1000 mA g^{-1}. Reproduced from ref. 431 with permission from Wiley-VCH.

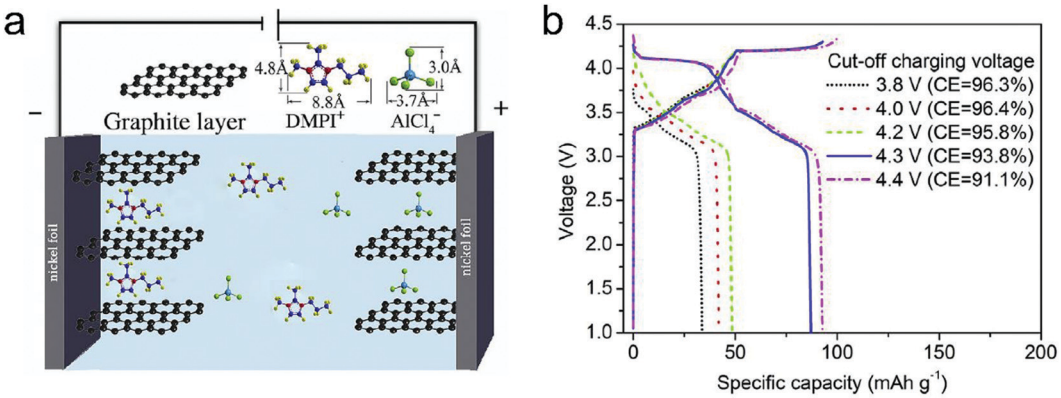

Fig. 32 (a) Operation principle of the DIB containing ($DMPI^+$)($AlCl_4^-$) as an IL electrolyte. (b) Charge/discharge curves of the DIB cell at cut-off charging voltages of 3.8–4.4 V. Reproduced from ref. 439 with permission from Elsevier.

efficiency of 85% at 1.5–3.8 V. The detailed electrode reactions are shown as eqn (36) and (37).

$$\text{Cathode: } AlCl_4^- + C_n \rightleftharpoons C_n^+AlCl_4^- + e^- \quad (36)$$

$$\text{Anode: } DMPI^+ + C_m + e^- \rightleftharpoons DMPI^+C_m^- \quad (37)$$

Revisiting this electrolyte system, Lin *et al.*[439] doubled the specific capacity of the C//C cells by replacing the graphite rod with natural graphite flakes. Further, they realized that the voltage window can be further expanded to achieve higher capacity (Fig. 32). At the optimal window of 1–4.3 V, a reversible capacity of 87 mA h g^{-1} was obtained with a V_m of 3.7 V. Moreover, the non-flammable IL electrolyte endows the C//C cell with high safety properties, allowing the full cells to function even under burning. The self-discharge rate of the C//C full cells was estimated as 4.2% per h, which is much higher than that of conventional LIBs and needs further optimization. Another issue is about $DMPI^+$ intercalated graphite ($DMPI^+$-GIC), which is not well characterized. Its structure information (stage number, intercalation structure, stoichiometry and so on) and intercalation kinetics remain to be explored.

The C//C batteries appear to work in other ILs, such as 1-butyl-1-methylpiperidinium bis(trifluoromethylsulfonyl)imide ($PP_{14}TFSI$) and $Pyr_{14}TFSI$.[441,442] There are multiple plateaus on the charge–discharge curves, which, however, were not well explained and characterized. IL decomposition was noticed in the disassembled cells, especially for the $PP_{14}TFSI$ system, while capacity fading is quite fast in $Pyr_{14}TFSI$-derived cells. MoS_2 can also serve as the anode to host $EMIm^+$ cations. The as-formed MoS_2//C cell in the $EMIm^+TFSI^-$ electrolyte delivered a maximum capacity of 77 mA h g^{-1} and a moderate cycle life of 300 cycles. Fundamentally, it is important to reveal in the future how $EMIm^+$ is intercalated into MoS_2, which may work for other complex cations and inspire further investigation over other layered compounds.

(2) Insertion-type or adsorption-type anode//C batteries. Besides inorganic layered materials, an organic compound, 5,7,12,14-pentacenetetrone (PCT), was applied as the complex cation host.[443] During charging, the Pyr_{14}^+ will be inserted into the PCT anode while $TFSI^-$ will intercalate into the graphite cathode (eqn (38) and (39)). The PCT//C cell shows a relatively stable overall performance of 100 cycles with a V_m of 2.2 V. The maximum capacity of the PCT//C cell was 165 mA h g^{-1} (on anode mass), around half value of its theoretical capacity (317 mA h g^{-1}). Similar to the C//C cell in $DMPI^+AlCl_4^-$, the PCT//C cell in $Pyr_{14}^+TFSI^-$ suffers from a quick self-discharge rate (4.7% h^{-1}).

$$\text{Cathode: } TFSI^- + C_n \rightleftharpoons C_n^+TFSI^- + e^- \quad (38)$$

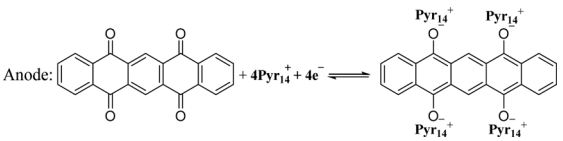

(39)

AC, as a typical adsorption-type anode, was explored by Wang *et al.* to establish AC//C cells.[396,444–447] The cation effect (diethyldimethyl ammonium, triethylmethyl ammonium, tetraethyl ammonium and tetrabutyl ammonium), anion effect (PF_6^-, BF_4^-, ClO_4^-) and solvent effect (EC, PC, γ-butyrolactone, butylene carbonate) on the electrochemical performance of AC//C cells were systematically investigated. The AC//C cells generally perform at 0–3.5 V with a V_m of <2.6 V and show a capacity of <40 mA h g^{-1}. In addition, an adsorption-type graphene anode was selected to pair with the graphite cathode in $EMIm^+PF_6^-$.[448] The device with linear shape charge–discharge curves operates at 0–4 V and outputs an energy density of 70 W h kg^{-1} (on active mass in both electrodes) with an average CE of 90%.

5. Conclusions

Overall, carbon materials hold great opportunities in the applications of numerous rechargeable energy storage technologies owing to the large abundance, low-cost raw materials, structural tailorability as well as the diverse redox electrochemistry (cation intercalation and anion intercalation). Currently, LIBs are dominating the rechargeable battery market, and post-LIBs (including NIBs, KIBs, DIBs, and AIBs) also show great potential in particular application fields. The energy density of post-LIBs remains to be enhanced to compete with LIBs, but the cost can be largely

reduced, which is especially desirable for grid-scale applications. In this respect, the utilization of carbon electrodes would strengthen the low-cost advantage of post-LIBs, facilitating their fast penetration into commercialization. In the case of donor-type intercalation, carbon materials serve as superior anode hosts for alkali metal cations (Li^+, Na^+, and K^+). Following a similar development roadmap, research on various cation-storage carbon materials all started with graphite, with the motivation to obtain a fundamental understanding of the cation-storage mechanism. Subsequently, extensive efforts have been devoted to exploring novel carbon nanostructures and their hybrids/superstructures for hosting alkali metal cations, which covers nanosized carbon, nanoporous carbon, disordered carbon, heteroatom-doped carbon, *etc.* It should be pointed out that disordered carbon with partial graphitization properties has dominated the research trend of cation-intercalation carbon, as these disordered carbon materials can offer plentiful active sites and a shortened diffusion path. The state-of-the-art disordered carbon anodes have demonstrated record-high reversible capacity (>1000 mA h g^{-1}) and ultralong cycling stability (>1000 cycles).

In the case of acceptor-type intercalation, the main focus has been put on the mechanism investigation and the corresponding energy storage devices (DIBs and AIBs). Compared to conventional Li-rich transition metal oxide cathodes in LIBs, the main advantages of graphitic carbon cathodes lie in high working potential (≥ 5 V *vs.* Li^+/Li), excellent electrical conductivity, high structure/chemical stability and excellent compatibility. Various anions have been electrochemically intercalated into graphitic carbon cathodes. By pairing graphitic carbon with appropriate anode materials and specific electrolyte systems, various DIBs/AIBs can be constructed to achieve particular performance such as non-flammability, polarity-switchability, fast-charging ability, flexibility, and operation under extreme temperatures. Nanostructured carbons with well-designed porous channels, crystallinity and chemical composition have shown impressive cycling and rate performance for anion storage due to their facilitated volume accommodation and ion diffusion. It is noteworthy that the volumetric capacity of nanostructured carbons remains to be further enhanced because of their low density. The heteroatom-doping effect on graphitic carbon, which was comprehensively investigated in carbon anodes, is not well understood for the carbon cathode. At the contemporary infancy stage of DIBs and AIBs, more efforts on designing novel carbon materials, understanding the ion-intercalation process/ion packing states and elevating the electrochemical performance of energy storage devices are crucially needed.

Cation-intercalation carbon materials

(a) The cation-storage chemistry of carbon materials is a complex integration of intercalation, adsorption, coordination, and clustering, which necessitates further in-depth investigations to guide and promote the development of high-performance carbon anodes. Although it has been well accepted that micropores, interlayer distance, disorder degree, and heteroatom doping play important roles in affecting the cation-storage behavior of carbon materials (*e.g.* ion diffusion pathways, electrode/electrolyte interface chemistry, and cation storage modes), the individual contribution and the optimal parameters of these influencing factors have not been well defined. Clearly, the identification of the optimal parameters for the best cation-storage behavior requires carbon materials with well-controlled atom-level and morphology-level properties and advanced (*in situ*) characterization techniques. Moreover, computational simulation/calculation is also critically important to offer a quantitative prospect for the further optimization of carbon materials. The acquired mechanism understanding will, in turn, provide a great guidance for the innovative design of carbon structures for cation storage.

(b) A fast increase in the number of reports has been witnessed on developing novel carbon anodes for LIBs, NIBs and KIBs in the last few years. In most cases, large specific surface area, rich carbon defects, high porosity, and heteroatom doping were pursued. However, the main drawback for these carbon materials cannot be overlooked, which is the low first-cycle CE (ranging from 40% to 80%) due to the large irreversible capacity. In practical full-cell applications, the large irreversible capacity of the anode must be compensated by using cathode materials in excess. After the first cycle, the presence of a dead mass of cathode material would result in the low overall capacity of the full cell. Meanwhile, disordered carbon anodes also suffer from the hysteresis between charge and discharge potential, which causes the constructed full cell to have a sloping voltage profile and low energy efficiency. Moreover, nanoporous carbon materials have a rich interparticle space and low tap density, which increases the interparticle electron-transport resistance and electrode thickness. These factors would hinder the development of battery electrodes with high loading mass and high volumetric capacity. Priority should be put on the understanding and investigation of these issues associated with carbon anodes. A precise control of carbon microstructures is clearly needed for improving the capacity of carbon structures without the sacrifice of the first-cycle CE, potential platform, and volumetric performance.

(c) Searching for next-generation intercalation form is also of great interest in the near future, which aims to develop carbon anodes with high intercalation capacity, low intercalation potential, fast charge-transfer kinetics, and superior chemical stability. It imposes a high demand for the innovation of topological carbon structures, guest ions, and electrolyte solvents. Some initial theoretical studies have been carried out to predict the cation-storage behavior of novel carbon nanostructures like nodal-line carbon[449] and 5-8-5 carbon rings,[299] which depict a superior cation-storage behavior than graphite. These studies would inspire the experimental efforts on the synthesis and investigations of novel carbon materials. It remains unexplored how the intercalation proceeds for carbon materials in a multi guest-ion environment, which may provide promising directions for the performance optimization of carbon anodes. Moreover, the electrolyte also has a significant influence on ionic conductivity, ion solvation, SEI formation, *etc.* Developing novel electrolyte concepts (*e.g.* organic solvents, novel additives, IL, concentrated electrolytes, liquid-state, solid-state) can also potentially change the cation-intercalation form of carbon anodes.

Anion-intercalation carbon materials

(a) The reported diffusion coefficient of different anions in graphitic carbon varies in a very broad range from 10^{-4} (for $AlCl_4^-$) to 10^{-15} cm^2 s^{-1} (for $TFSI^-$). However, the fundamental reason remains to be revealed. A detailed diffusion investigation or simulation on a model graphitic carbon material like HOPG will be helpful to understand the kinetic difference between different anions. Further, anion intercalation will bring about high-volume change (100–140%) of the graphitic carbon cathode, which is much higher than that due to alkaline cation intercalation. Engineering on the porous structure of graphitic carbon and electrode porosity is demanded to solve the disintegration issue, especially at high mass loadings. Freestanding yet robust graphitic carbon with 3D interconnected porous channels and fair density is highly desirable to alleviate structural degradation during large volume variation and achieve high volumetric capacity, if inactive conductive additive, binder and metallic current collector can be removed. Currently, graphite remains the best carbon material for the anion host due to its extremely low cost, balanced performance and excellent compatibility to nowadays infrastructures of LIBs. Further chemical modification of graphite by heteroatom doping like B and graphitic N may introduce more active sites for anion storage.

(b) Due to the strong electrostatic repulsion between anions, the specific capacity of the graphitic carbon cathode currently is less than 150 mA h g^{-1}, which cannot meet the demand for high-energy cathode materials. Replacing redox-inactive anions with redox-active halogen atoms is an efficient solution. Further exploring redox-active anions remains a feasible way to enhance the capacity of graphitic carbon cathodes. An unavoidable problem associated with anion-intercalation carbon materials is the low CE, which can be attributed to the self-discharge issue of carbon cathodes and/or side reactions (*e.g.*, electrolyte decomposition or current collector etching) at high potentials. The self-discharge issue of anion-intercalation carbon cathodes refers to the self-deintercalation of anions from carbon hosts, which is accompanied by a continuous voltage drop of batteries. Theoretical simulation may help predict the most stable anion-intercalated structure, which can be readily implemented by voltage control of energy devices. More investigations are also suggested to optimize the chemical composition of carbon, charge protocol, and battery operation/storage condition. Regarding the electrolyte decomposition and anodic etching, screening current collectors, adopting highly stable electrolytes (*e.g.*, F-containing solvents or additives), and engineering interphase are encouraged in the future to suppress side reactions during anion intercalation into carbon cathodes.

(c) The charge–discharge profiles and CV curves of the graphite cathode during PF_6^- and $AlCl_4^-$ intercalation/deintercalation are quite similar, except different potential ranges.[163,189,221] The stable capacity of graphite in both cases is very close ($\sim$100 mA h g^{-1}). However, the stage number of PF_6^--GIC is stage-I while it is stage-II/III/IV for $AlCl_4^-$-GIC when fully charged. Considering the larger size of $AlCl_4^-$ over PF_6^-, additional efforts may be needed to analyze the packing state of $AlCl_4^-$ between graphite interlayers and to re-evaluate the volume expansion of the $AlCl_4^-$-GIC.

Ion-intercalation carbon-based rechargeable batteries

(a) Most of the studies on cation-intercalation carbon are limited in material-level evaluation with half-cell tests; only few research studies on full-cell exploration have been performed to demonstrate the availability of the carbon anode for practical energy storage devices. Partial reason could be the low first-cycle CE of the obtained carbon anode. Anyhow, we hope that this review could draw more research attention to the full cell exploration, rather than only material side. Particular emphasis should be focused on the configuration optimization, cell-level performance metrics, and degradation mechanism. The acquired knowledge at the cell level will speed up the transition of new proof-of-concept carbon anode design and device design to scalable applications.

(b) Energy density has been the driving force that motivates battery development in the last 200 years. Calculating the energy density of DIBs and AIBs based only on the mass of electrodes will lead to overrated values because the electrolyte as an active material contributes notable weight, especially in dilute electrolyte systems. Therefore, a concentrated electrolyte or even a solid-state electrolyte is preferable for high-energy DIBs and AIBs. One remarkable strategy to boost the energy densities of carbon electrode-based batteries was recently demonstrated by hybridizing the Li^+-containing cathode ($LiFePO_4$) with the graphite cathode. The integration of Li^+-deintercalation and PF_6^--intercalation in the hybrid cathode favours the enhanced capacity and broadened voltage window, thus increasing the energy density of full cells by 35%.[450] To push forward the energy density of carbon-based full cells, innovation on carbon materials merely is insufficient. Multi-disciplinary efforts on materials, chemistry, and engineering are necessary to exploit novel ion hosts, electrolytes, electrochemistry, and battery configurations. Constructing hybrid cathodes to introduce conversion/intercalation chemistry is a successful example. Another potential option lies in rocking-chair carbon-based anion batteries, which perform under lean electrolytes with anions as charge carriers. The selection of anion charge carriers, host materials, and electrolyte systems needs to be rationally considered.

(c) Currently, the CE of DIBs and AIBs is not satisfactory, which is mainly inherited from carbon cathodes. The low CE leads to the low energy efficiency and limited span life of full devices with lean electrolytes. C//C batteries are the most promising systems for commercial application, as they offer the lowest cost and the highest operation voltage. The expense on electrolytes should be counted as well when assessing the device-level cost and Na and K-based salts are preferred over Li salts for such purpose. The present AIBs are based on a redox couple of $Al_2Cl_7^-$/Al (−0.7 V *vs.* SHE), rather than Al^{3+}/Al (−1.66 V *vs.* SHE).[451] The potential gap is nearly 1 V. Under theoretical conditions, the Al^{3+}-based DIBs are anticipated to possess a higher V_m than the current $Al_2Cl_7^-$-based AIBs (3 V *vs.* 2 V). The requisite is reversible Al plating and stripping in the Al^{3+}-based electrolyte with negligible polarization.

(d) The cycling performance of most demonstrated devices is evaluated under a flooded electrolyte. The mass of the electrolyte at least needs to match with the capacity of charge carrier hosts. The impact of electrolyte amount on overall electrochemical

performance (cycling and energy density) should be evaluated, which is important to offer a balance point for practical devices.

List of abbreviations

1D	One-dimensional
2D	Two-dimensional
3D	Three-dimensional
AC	Activated carbon
AIBs	Al-ion batteries
BET	Brunauer–Emmett–Teller
$BETI^-$	Bis(pentafluoroethanesulfonyl)imide
B	Boron
C//C	Dual-carbon
CE	Coulombic efficiency
CNTs	Carbon nanotubes
CV	Cyclic voltammetry
CVD	Chemical vapor deposition
DEC	Diethyl carbonate
DFT	Density functional theory
DIBs	Dual-ion batteries
DMC	Dimethyl carbonate
DME	Dimethyl ether
$DMPI^+$	1,2-Dimethyl-3-propylimidazolium cations
DOL	1,3-Dioxolane
EC	Ethyl carbonate
EG	Electrochemically exfoliated graphene
EIS	Electrochemical impedance spectroscopy
EMC	Ethyl methyl carbonate
EMImCl	1-Ethyl-3-methylimidazolium chloride
EMImTfO	1-Ethyl-3-methylimidazolium trifluoromethanesulfonate
EQCM	Electrochemical quartz crystal microbalance
FEC	Monofluoroethylene carbonate
FSI^-	Bis(fluorosulfonyl)imide
$FTFSI^-$	Fluorosulfonyl-(trifluoromethanesulfonyl)imide
GD	Graphitization degree
GIC	Graphite intercalation compound
GITT	Galvanostatic intermittent titration technique
GO	Graphite oxide
HOMO	Highest occupied molecular orbital
HOPG	Highly oriented pyrolytic graphite
IL	Ionic liquid
IUPAC	International Union of Pure and Applied Chemistry
KIBs	K-ion batteries
LIBs	Li-ion batteries
LICs	Li-ion capacitors
LiTfO	Lithium trifluoromethanesulfonate
MCMB	Mesocarbon microbeads
MWCNTs	Multi-walled CNTs
NIB	Na-ion battery
NMR	Nuclear magnetic resonance spectroscopy
PAN	Polyacrylonitrile
PC	Propylene carbonate
PC	Propylene carbonate
PCT	5,7,12,14-Pentacenetetrone
PG	Pyrolytic graphite
$PP_{14}TFSI$	1-Butyl-1-methylpiperidinium bis(trifluoromethylsulfonyl)imide
$Pyr_{14}TFSI$	*N*-Butyl-*N*-methylpyrrolidinium bis(trifluoromethanesulfonyl)imide
rGO	Reduced graphene oxide
SEI	Solid electrolyte interphase
SEM	Scanning electron microscope
SWCNTs	Single-walled CNTs
TEM	Transmission electron microscope
$TFSI^-$	Bis(trifluoromethanesulfonyl)imide
TMP	Trimethyl phosphate
VC	Vinylene carbonate
XRD	X-ray diffraction
XPS	X-ray photoelectron spectroscopy
XAS	X-ray adsorption spectroscopy

Conflicts of interest

There are no conflicts to declare.

Acknowledgements

This work was financially supported by European Union's Horizon 2020 research and innovation programme (GrapheneCore3 881603), ERC Consolidator grant (T2DCP 819698), M-ERA.NET and Sächsisches Staatsministerium für Wissenschaft und Kunst (HYSUCAP 100478697), and German Research Foundation (DFG) within the Cluster of Excellence, CRC 1415 (grant no. 417590517), and Polymer-based Batteries (SPP 2248, RACOF-MMIS).

Notes and references

1 B. Obama, *Science*, 2017, **355**, 126–129.
2 M. Yu, R. Dong and X. Feng, *J. Am. Chem. Soc.*, 2020, **142**, 12903–12915.
3 W. Liu, L. Yu, R. Yin, X. Xu, J. Feng, X. Jiang, D. Zheng, X. Gao, X. Gao, W. Que, P. Ruan, F. Wu, W. Shi and X. Cao, *Small*, 2020, **16**, e1906775.
4 M. Yu and X. Feng, *Joule*, 2019, **3**, 338–360.
5 M. Yu, H. Shao, G. Wang, F. Yang, C. Liang, P. Rozier, C. Z. Wang, X. Lu, P. Simon and X. Feng, *Nat. Commun.*, 2020, **11**, 1348.
6 M. Yu, N. Chandrasekhar, R. K. M. Raghupathy, K. H. Ly, H. Zhang, E. Dmitrieva, C. Liang, X. Lu, T. D. Kuhne, H. Mirhosseini, I. M. Weidinger and X. Feng, *J. Am. Chem. Soc.*, 2020, **142**(46), 19570–19578.
7 E. Pomerantseva, F. Bonaccorso, X. Feng, Y. Cui and Y. Gogotsi, *Science*, 2019, 366, DOI: 10.1126/science.aan8285.
8 H. Zhang, W. Wu, Q. Liu, F. Yang, X. Shi, X. Liu, M. Yu and X. Lu, *Angew. Chem., Int. Ed.*, 2020, DOI: 10.1002/anie.202010073.

9 W. Shi, X. Liu, T. Deng, S. Huang, M. Ding, X. Miao, C. Zhu, Y. Zhu, W. Liu, F. Wu, C. Gao, S. W. Yang, H. Y. Yang, J. Shen and X. Cao, *Adv. Mater.*, 2020, **32**, e1907404.
10 J. Liu, Z. Bao, Y. Cui, E. J. Dufek, J. B. Goodenough, P. Khalifah, Q. Li, B. Y. Liaw, P. Liu, A. Manthiram, Y. S. Meng, V. R. Subramanian, M. F. Toney, V. V. Viswanathan, M. S. Whittingham, J. Xiao, W. Xu, J. Yang, X.-Q. Yang and J.-G. Zhang, *Nat. Energy*, 2019, **4**, 180–186.
11 Y. Liu, Y. Zhu and Y. Cui, *Nat. Energy*, 2019, **4**, 540–550.
12 Z. Yang, J. Zhang, M. C. Kintner-Meyer, X. Lu, D. Choi, J. P. Lemmon and J. Liu, *Chem. Rev.*, 2011, **111**, 3577–3613.
13 S. Kalaiselvam and R. Parameshwaran, *Thermal Energy Storage Technologies for Sustainability*, 2014, pp. 21–56, DOI: 10.1016/b978-0-12-417291-3.00002-5.
14 C. P. Grey and J. M. Tarascon, *Nat. Mater.*, 2016, **16**, 45–56.
15 Z. Yang, J. Ren, Z. Zhang, X. Chen, G. Guan, L. Qiu, Y. Zhang and H. Peng, *Chem. Rev.*, 2015, **115**, 5159–5223.
16 Y. Han, Z. Lai, Z. Wang, M. Yu, Y. Tong and X. Lu, *Chem. – Eur. J.*, 2018, **24**, 7312–7329.
17 J. Ni and Y. Li, *Adv. Energy Mater.*, 2016, **6**, 1600278.
18 Y. Li, K. Yan, H.-W. Lee, Z. Lu, N. Liu and Y. Cui, *Nat. Energy*, 2016, **1**, 15029.
19 H. Jin, S. Xin, C. Chuang, W. Li, H. Wang, J. Zhu, H. Xie, T. Zhang, Y. Wan, Z. Qi, W. Yan, Y.-R. Lu, T.-S. Chan, X. Wu, J. B. Goodenough, H. Ji and X. Duan, *Science*, 2020, **370**, 192–197.
20 H. Li, T. Yamaguchi, S. Matsumoto, H. Hoshikawa, T. Kumagai, N. L. Okamoto and T. Ichitsubo, *Nat. Commun.*, 2020, **11**, 1584.
21 W. Wei, G. Wang, S. Yang, X. Feng and K. Mullen, *J. Am. Chem. Soc.*, 2015, **137**, 5576–5581.
22 R. Xu, G. Wang, T. Zhou, Q. Zhang, H.-P. Cong, X. Sen, J. Rao, C. Zhang, Y. Liu, Z. Guo and S.-H. Yu, *Nano Energy*, 2017, **39**, 253–261.
23 P. Poizot, S. Laruelle, S. Grugeon, L. Dupont and J. M. Tarascon, *Nature*, 2000, **407**, 496–499.
24 Y. M. Chen, X. Y. Yu, Z. Li, U. Paik and X. W. Lou, *Sci. Adv.*, 2016, **2**, e1600021.
25 G. Wang, J. Zhang, S. Yang, F. Wang, X. Zhuang, K. Müllen and X. Feng, *Adv. Energy Mater.*, 2018, **8**, 1702254.
26 G. Wang, Y. Sun, D. Li, W. Wei, X. Feng and K. Müllen, *Small*, 2016, **12**, 3914–3919.
27 W. Rüdorff and U. Hofmann, *Z. Anorg. Allg. Chem.*, 1938, **238**, 1–50.
28 I. A. Rodríguez-Pérez and X. Ji, *ACS Energy Lett.*, 2017, **2**, 1762–1770.
29 M. Wang and Y. Tang, *Adv. Energy Mater.*, 2018, **8**, 1703320.
30 F. P. McCullough Jr and A. F. Beale Jr, US 4865931A, 1989.
31 P. Jiménez, E. Levillain, O. Alévêque, D. Guyomard, B. Lestriez and J. Gaubicher, *Angew. Chem., Int. Ed.*, 2017, **56**, 1553–1556.
32 H. Gao, L. Xue, S. Xin and J. B. Goodenough, *Angew. Chem., Int. Ed.*, 2018, **57**, 5449–5453.
33 M. Walter, K. V. Kravchyk, C. Böfer, R. Widmer and M. V. Kovalenko, *Adv. Mater.*, 2018, **30**, 1705644.
34 S. Muench, A. Wild, C. Friebe, B. Häupler, T. Janoschka and U. S. Schubert, *Chem. Rev.*, 2016, **116**, 9438–9484.
35 P. Poizot, J. Gaubicher, S. Renault, L. Dubois, Y. Liang and Y. Yao, *Chem. Rev.*, 2020, **120**, 6490–6557.
36 H. Liu, X. Liu, W. Li, X. Guo, Y. Wang, G. Wang and D. Zhao, *Adv. Energy Mater.*, 2017, **7**, 1700283.
37 N. A. Kaskhedikar and J. Maier, *Adv. Mater.*, 2009, **21**, 2664–2680.
38 J. Kim, M. S. Choi, K. H. Shin, M. Kota, Y. Kang, S. Lee, J. Y. Lee and H. S. Park, *Adv. Mater.*, 2019, **31**, e1803444.
39 H. Hou, X. Qiu, W. Wei, Y. Zhang and X. Ji, *Adv. Energy Mater.*, 2017, **7**, 1602898.
40 D. Saurel, B. Orayech, B. Xiao, D. Carriazo, X. Li and T. Rojo, *Adv. Energy Mater.*, 2018, **8**, 1703268.
41 J. C. Pramudita, D. Sehrawat, D. Goonetilleke and N. Sharma, *Adv. Energy Mater.*, 2017, **7**, 1602911.
42 X. Wu, Y. Chen, Z. Xing, C. W. K. Lam, S. S. Pang, W. Zhang and Z. Ju, *Adv. Energy Mater.*, 2019, **9**, 1900343.
43 Y. Li, Y. Lu, P. Adelhelm, M. M. Titirici and Y. S. Hu, *Chem. Soc. Rev.*, 2019, **48**, 4655–4687.
44 A. Yacoby, *Nat. Phys.*, 2011, **7**, 925–926.
45 R. C. Dante, *Handbook of Friction Materials and their Applications*, 2016, pp. 93–103, DOI: 10.1016/b978-0-08-100619-1.00007-9.
46 K. S. Novoselov, A. K. Geim, S. V. Morozov, D. Jiang, Y. Zhang, S. V. Dubonos, I. V. Grigorieva and A. A. Firsov, *Science*, 2004, **306**, 666–669.
47 C. Lee, X. Wei, J. W. Kysar and J. Hone, *Science*, 2008, **321**, 385–388.
48 K. I. Bolotin, K. J. Sikes, Z. Jiang, M. Klima, G. Fudenberg, J. Hone, P. Kim and H. L. Stormer, *Solid State Commun.*, 2008, **146**, 351–355.
49 M. D. Stoller, S. Park, Y. Zhu, J. An and R. S. Ruoff, *Nano Lett.*, 2008, **8**, 3498–3502.
50 K. Ji, J. Han, A. Hirata, T. Fujita, Y. Shen, S. Ning, P. Liu, H. Kashani, Y. Tian, Y. Ito, J. I. Fujita and Y. Oyama, *Nat. Commun.*, 2019, **10**, 275.
51 F. Yao, F. Gunes, H. Q. Ta, S. M. Lee, S. J. Chae, K. Y. Sheem, C. S. Cojocaru, S. S. Xie and Y. H. Lee, *J. Am. Chem. Soc.*, 2012, **134**, 8646–8654.
52 A. L. Reddy, A. Srivastava, S. R. Gowda, H. Gullapalli, M. Dubey and P. M. Ajayan, *ACS Nano*, 2010, **4**, 6337–6342.
53 W. S. Hummers and R. E. Offeman, *J. Am. Chem. Soc.*, 1958, **80**, 1339.
54 D. R. Dreyer, S. Park, C. W. Bielawski and R. S. Ruoff, *Chem. Soc. Rev.*, 2010, **39**, 228–240.
55 J. N. Coleman, *Acc. Chem. Res.*, 2013, **46**, 14–22.
56 K. R. Paton, E. Varrla, C. Backes, R. J. Smith, U. Khan, A. O'Neill, C. Boland, M. Lotya, O. M. Istrate, P. King, T. Higgins, S. Barwich, P. May, P. Puczkarski, I. Ahmed, M. Moebius, H. Pettersson, E. Long, J. Coelho, S. E. O'Brien, E. K. McGuire, B. M. Sanchez, G. S. Duesberg, N. McEvoy, T. J. Pennycook, C. Downing, A. Crossley, V. Nicolosi and J. N. Coleman, *Nat. Mater.*, 2014, **13**, 624–630.
57 S. Yang, A. G. Ricciardulli, S. Liu, R. Dong, M. R. Lohe, A. Becker, M. A. Squillaci, P. Samori, K. Mullen and X. Feng, *Angew. Chem., Int. Ed.*, 2017, **56**, 6669–6675.
58 S. Iijima, *Nature*, 1991, **354**, 56–58.

59 A. P. Graham, G. S. Duesberg, W. Hoenlein, F. Kreupl, M. Liebau, R. Martin, B. Rajasekharan, W. Pamler, R. Seidel, W. Steinhoegl and E. Unger, *Appl. Phys. A: Mater. Sci. Process.*, 2005, **80**, 1141–1151.
60 R. Zhang, Y. Zhang, Q. Zhang, H. Xie, W. Qian and F. Wei, *ACS Nano*, 2013, **7**, 6156–6161.
61 T. W. Odom, J.-L. Huang, P. Kim and C. M. Lieber, *Nature*, 1998, **391**, 62–64.
62 M. Xu, D. N. Futaba, M. Yumura and K. Hata, *Adv. Mater.*, 2011, **23**, 3686–3691.
63 K. Uetani, S. Ata, S. Tomonoh, T. Yamada, M. Yumura and K. Hata, *Adv. Mater.*, 2014, **26**, 5857–5862.
64 J.-C. Charlier, X. Blase and S. Roche, *Rev. Mod. Phys.*, 2007, **79**, 677–732.
65 T. Guo, P. Nikolaev, A. Thess, D. T. Colbert and R. E. Smalley, *Chem. Phys. Lett.*, 1995, **243**, 49–54.
66 S. Fan, M. G. Chapline, N. R. Franklin, T. W. Tombler, A. M. Cassell and H. Dai, *Science*, 1999, **283**, 512–514.
67 H. Dai, A. G. Rinzler, P. Nikolaev, A. Thess, D. T. Colbert and R. E. Smalley, *Chem. Phys. Lett.*, 1996, **260**, 471–475.
68 K. Hata, D. N. Futaba, K. Mizuno, T. Namai, M. Yumura and S. Iijima, *Science*, 2004, **306**, 1362–1364.
69 C.-M. Seah, S.-P. Chai and A. R. Mohamed, *Carbon*, 2011, **49**, 4613–4635.
70 G. D. Nessim, *Nanoscale*, 2010, **2**, 1306–1323.
71 E. Irisarri, A. Ponrouch and M. R. Palacin, *J. Electrochem. Soc.*, 2015, **162**, A2476–A2482.
72 M. Yu, Y. Huang, C. Li, Y. Zeng, W. Wang, Y. Li, P. Fang, X. Lu and Y. Tong, *Adv. Funct. Mater.*, 2015, **25**, 324–330.
73 J. Gilbert, J. Kipling, B. McEnaney and J. Sherwood, *Polymer*, 1962, **3**, 1–10.
74 J. J. Kipling, J. N. Sherwood, P. V. Shooter and N. R. Thompson, *Carbon*, 1964, **1**, 315–320.
75 F. G. Emmerich, *Carbon*, 1995, **33**, 1709–1715.
76 L. Chen, S. Yang, J. Huang, W. Xie, B. Ding, Y. Liu, F. Xu and Y. Liang, *Mater. Lett.*, 2018, **232**, 187–190.
77 M. Yu, Y. Lu, H. Zheng and X. Lu, *Chem. – Eur. J.*, 2018, **24**, 3639–3649.
78 F. Xu, B. Ding, Y. Qiu, J. Wu, Z. Cheng, G. Jiang, H. Li, X. Liu, B. Wei and H. Wang, *Langmuir*, 2019, **35**, 12889–12897.
79 K. Sing, D. Everett, R. Haul, L. Moscou, R. Pierotti, J. Rouquerol and T. Siemieniewska, *Pure Appl. Chem.*, 1985, **57**, 603.
80 W. Wang, J. Zhou, Z. Wang, L. Zhao, P. Li, Y. Yang, C. Yang, H. Huang and S. Guo, *Adv. Energy Mater.*, 2018, **8**, 1701648.
81 G. Wang, Y. Sun, D. Li, H. W. Liang, R. Dong, X. Feng and K. Mullen, *Angew. Chem., Int. Ed.*, 2015, **54**, 15191–15196.
82 Y. Meng, D. Gu, F. Zhang, Y. Shi, H. Yang, Z. Li, C. Yu, B. Tu and D. Zhao, *Angew. Chem., Int. Ed.*, 2005, **44**, 7053–7059.
83 A. Stein, B. E. Wilson and S. G. Rudisill, *Chem. Soc. Rev.*, 2013, **42**, 2763–2803.
84 Y. Zhu, S. Murali, M. D. Stoller, K. J. Ganesh, W. Cai, P. J. Ferreira, A. Pirkle, R. M. Wallace, K. A. Cychosz, M. Thommes, D. Su, E. A. Stach and R. S. Ruoff, *Science*, 2011, **332**, 1537–1541.
85 F. Xu, Z. Tang, S. Huang, L. Chen, Y. Liang, W. Mai, H. Zhong, R. Fu and D. Wu, *Nat. Commun.*, 2015, **6**, 7221.
86 S. Román, J. F. González, C. M. González-García and F. Zamora, *Fuel Process. Technol.*, 2008, **89**, 715–720.
87 N. Sun, Z. Guan, Y. Liu, Y. Cao, Q. Zhu, H. Liu, Z. Wang, P. Zhang and B. Xu, *Adv. Energy Mater.*, 2019, **9**, 1901351.
88 R. E. Franklin, *Nature*, 1956, **177**, 239.
89 M. Audier, A. Oberlin, M. Oberlin, M. Coulon and L. Bonnetain, *Carbon*, 1981, **19**, 217–224.
90 F. J. Maldonado-Hódar, C. Moreno-Castilla, J. Rivera-Utrilla, Y. Hanzawa and Y. Yamada, *Langmuir*, 2000, **16**, 4367–4373.
91 M. Sevilla and A. B. Fuertes, *Carbon*, 2006, **44**, 468–474.
92 T.-H. Kim, E. K. Jeon, Y. Ko, B. Y. Jang, B.-S. Kim and H.-K. Song, *J. Mater. Chem. A*, 2014, **2**, 7600–7605.
93 Y. Wen, K. He, Y. Zhu, F. Han, Y. Xu, I. Matsuda, Y. Ishii, J. Cumings and C. Wang, *Nat. Commun.*, 2014, **5**, 4033.
94 X. Qi, J. Qu, H.-B. Zhang, D. Yang, Y. Yu, C. Chi and Z.-Z. Yu, *J. Mater. Chem. A*, 2015, **3**, 15498–15504.
95 L. Wang, Y. Zhu, C. Guo, X. Zhu, J. Liang and Y. Qian, *ChemSusChem*, 2014, **7**, 87–91.
96 F. Wang, J. Yi, Y. Wang, C. Wang, J. Wang and Y. Xia, *Adv. Energy Mater.*, 2014, **4**, 1300600.
97 Y. Wu, M. Gong, M. C. Lin, C. Yuan, M. Angell, L. Huang, D. Y. Wang, X. Zhang, J. Yang, B. J. Hwang and H. Dai, *Adv. Mater.*, 2016, **28**, 9218–9222.
98 T. Nakajima and Y. Matsuo, *Carbon*, 1994, **32**, 469–475.
99 B. M. Way and J. R. Dahn, *J. Electrochem. Soc.*, 1994, **141**, 907–912.
100 U. Tanaka, T. Sogabe, H. Sakagoshi, M. Ito and T. Tojo, *Carbon*, 2001, **39**, 931–936.
101 J. V. Rani, V. Kanakaiah, T. Dadmal, M. S. Rao and S. Bhavanarushi, *J. Electrochem. Soc.*, 2013, **160**, A1781–A1784.
102 E. Peled, C. Menachem, D. Bar-Tow and A. Melman, *J. Electrochem. Soc.*, 1996, **143**, L4–L7.
103 T. H. N. G. Amaraweera, N. W. B. Balasooriya, H. W. M. A. C. Wijayasinghe, A. N. B. Attanayake, B.-E. Mellander and M. A. K. L. Dissanayake, *Ionics*, 2018, **24**, 3423–3429.
104 B. Dyatkin, J. Halim and J. A. Read, *J. Carbon Resour.*, 2017, **3**, 11.
105 Y. Cao, L. Xiao, X. Ai and H. Yang, *Electrochem. Solid-State Lett.*, 2003, **6**, A30–A33.
106 Q. Pan, H. Wang and Y. Jiang, *J. Mater. Chem.*, 2007, **17**, 329–334.
107 F. Ding, W. Xu, D. Choi, W. Wang, X. Li, M. H. Engelhard, X. Chen, Z. Yang and J.-G. Zhang, *J. Mater. Chem.*, 2012, **22**, 12745–12751.
108 G. Song, J. Ryu, S. Ko, B. M. Bang, S. Choi, M. Shin, S.-Y. Lee and S. Park, *Chem. – Asian J.*, 2016, **11**, 1711–1717.
109 Y. S. Kim, S. H. Kim, G. Kim, S. Heo, J. Mun, S. Han, H. Jung, Y. K. Kyoung, D. J. Yun, W. J. Baek and S. Doo, *ACS Appl. Mater. Interfaces*, 2016, **8**, 30980–30984.
110 D. C. Elias, R. R. Nair, T. M. G. Mohiuddin, S. V. Morozov, P. Blake, M. P. Halsall, A. C. Ferrari, D. W. Boukhvalov, M. I. Katsnelson, A. K. Geim and K. S. Novoselov, *Science*, 2009, **323**, 610–613.
111 H. Wang, Y. Zhou, D. Wu, L. Liao, S. Zhao, H. Peng and Z. Liu, *Small*, 2013, **9**, 1316–1320.

112 X. Wang, G. Sun, P. Routh, D.-H. Kim, W. Huang and P. Chen, *Chem. Soc. Rev.*, 2014, **43**, 7067–7098.
113 Y. Li, Y. Yuan, Y. Bai, Y. Liu, Z. Wang, L. Li, F. Wu, K. Amine, C. Wu and J. Lu, *Adv. Energy Mater.*, 2018, **8**, 1702781.
114 H. Hou, L. Shao, Y. Zhang, G. Zou, J. Chen and X. Ji, *Adv. Sci.*, 2017, **4**, 1600243.
115 Z. Li, L. Ma, T. W. Surta, C. Bommier, Z. Jian, Z. Xing, W. F. Stickle, M. Dolgos, K. Amine, J. Lu, T. Wu and X. Ji, *ACS Energy Lett.*, 2016, **1**, 395–401.
116 H. Liu, M. Jia, N. Sun, B. Cao, R. Chen, Q. Zhu, F. Wu, N. Qiao and B. Xu, *ACS Appl. Mater. Interfaces*, 2015, **7**, 27124–27130.
117 J. S. Sander, R. M. Erb, L. Li, A. Gurijala and Y. M. Chiang, *Nat. Energy*, 2016, **1**, 16099.
118 Y. Kuang, C. Chen, D. Kirsch and L. Hu, *Adv. Energy Mater.*, 2019, **9**, 1901457.
119 J. Billaud, F. Bouville, T. Magrini, C. Villevieille and A. R. Studart, *Nat. Energy*, 2016, **1**, 16097.
120 C. Schafhaeutl, *J. Prakt. Chem.*, 1840, **21**, 129–157.
121 Y. Matsuda, *J. Electrochem. Soc.*, 1981, **128**, 2552.
122 M. Winter, J. O. Besenhard, M. E. Spahr and P. J. A. m. Novak, *Adv. Mater.*, 1998, **10**, 725–763.
123 T. Ohzuku, *J. Electrochem. Soc.*, 1993, **140**, 2490.
124 H. Kim, J. Hong, G. Yoon, H. Kim, K.-Y. Park, M.-S. Park, W.-S. Yoon and K. Kang, *Energy Environ. Sci.*, 2015, **8**, 2963–2969.
125 Z. Jian, W. Luo and X. Ji, *J. Am. Chem. Soc.*, 2015, **137**, 11566–11569.
126 H. P. Boehm, R. Setton and E. Stumpp, *Pure Appl. Chem.*, 1994, **66**, 1893–1901.
127 N. Daumas and A. Herold, *C. R. Hebd. Seances Acad. Sci., Ser. C*, 1969, **268**, 373.
128 C. Sole, N. E. Drewett and L. J. Hardwick, *Faraday Discuss.*, 2014, **172**, 223–237.
129 J. A. Read, *J. Phys. Chem. C*, 2015, **119**, 8438–8446.
130 J. A. Seel and J. R. Dahn, *J. Electrochem. Soc.*, 2000, **147**, 892–898.
131 X. Y. Song, *J. Electrochem. Soc.*, 1996, **143**, L120.
132 M. Kuhne, F. Borrnert, S. Fecher, M. Ghorbani-Asl, J. Biskupek, D. Samuelis, A. V. Krasheninnikov, U. Kaiser and J. H. Smet, *Nature*, 2018, **564**, 234–239.
133 R. Raccichini, A. Varzi, S. Passerini and B. Scrosati, *Nat. Mater.*, 2015, **14**, 271–279.
134 J. R. Dahn, T. Zheng, Y. Liu and J. S. Xue, *Science*, 1995, **270**, 590–593.
135 K. Sato, M. Noguchi, A. Demachi, N. Oki and M. Endo, *Science*, 1994, **264**, 556–558.
136 T. Kar, J. Pattanayak and S. Scheiner, *J. Phys. Chem. A*, 2001, **105**, 10397–10403.
137 K. Nishidate and M. Hasegawa, *Phys. Rev. B: Condens. Matter Mater. Phys.*, 2005, **71**, 245418.
138 B. Song, J. Yang, J. Zhao and H. Fang, *Energy Environ. Sci.*, 2011, 4.
139 J. Zhao, A. Buldum, J. Han and J. Ping Lu, *Phys. Rev. Lett.*, 2000, **85**, 1706–1709.
140 C. Garau, A. Frontera, D. Quiñonero, A. Costa, P. Ballester and P. M. Deyà, *Chem. Phys. Lett.*, 2003, **374**, 548–555.
141 T. Zheng, J. N. Reimers and J. R. Dahn, *Phys. Rev. B: Condens. Matter Mater. Phys.*, 1995, **51**, 734–741.
142 T. Zheng, *J. Electrochem. Soc.*, 1995, **142**, 2581.
143 T. Zheng, W. Xing and J. R. Dahn, *Carbon*, 1996, **34**, 1501–1507.
144 E. Peled, *J. Electrochem. Soc.*, 1979, **126**, 2047.
145 Z. Wang, S. M. Selbach and T. Grande, *RSC Adv.*, 2014, **4**, 3973–3983.
146 Y. Liu, B. V. Merinov and W. A. Goddard 3rd, *Proc. Natl. Acad. Sci. U. S. A.*, 2016, **113**, 3735–3739.
147 D. A. Stevens and J. R. Dahn, *J. Electrochem. Soc.*, 2001, **148**, A803.
148 C. Bommier, T. W. Surta, M. Dolgos and X. Ji, *Nano Lett.*, 2015, **15**, 5888–5892.
149 Y. Sun, J. Tang, K. Zhang, J. Yuan, J. Li, D. M. Zhu, K. Ozawa and L. C. Qin, *Nanoscale*, 2017, **9**, 2585–2595.
150 Y. Cao, L. Xiao, M. L. Sushko, W. Wang, B. Schwenzer, J. Xiao, Z. Nie, L. V. Saraf, Z. Yang and J. Liu, *Nano Lett.*, 2012, **12**, 3783–3787.
151 Y.-X. Wang, S.-L. Chou, H.-K. Liu and S.-X. Dou, *Carbon*, 2013, **57**, 202–208.
152 A. P. Cohn, K. Share, R. Carter, L. Oakes and C. L. Pint, *Nano Lett.*, 2016, **16**, 543–548.
153 Z. Zhu, F. Cheng, Z. Hu, Z. Niu and J. Chen, *J. Power Sources*, 2015, **293**, 626–634.
154 B. Jache and P. Adelhelm, *Angew. Chem., Int. Ed.*, 2014, **53**, 10169–10173.
155 H. Kim, J. Hong, Y.-U. Park, J. Kim, I. Hwang and K. Kang, *Adv. Funct. Mater.*, 2015, **25**, 534–541.
156 G. Yoon, H. Kim, I. Park and K. Kang, *Adv. Energy Mater.*, 2017, **7**, 1601519.
157 D. A. Stevens and J. R. Dahn, *J. Electrochem. Soc.*, 2000, **147**, 1271.
158 Y. Xie, Y. Chen, L. Liu, P. Tao, M. Fan, N. Xu, X. Shen and C. Yan, *Adv. Mater.*, 2017, **29**, 1702268.
159 J. Yang, X. Zhou, D. Wu, X. Zhao and Z. Zhou, *Adv. Mater.*, 2017, **29**, 1604108.
160 W. Luo, J. Wan, B. Ozdemir, W. Bao, Y. Chen, J. Dai, H. Lin, Y. Xu, F. Gu, V. Barone and L. Hu, *Nano Lett.*, 2015, **15**, 7671–7677.
161 K. Share, A. P. Cohn, R. Carter, B. Rogers and C. L. Pint, *ACS Nano*, 2016, **10**, 9738–9744.
162 H. S. Kim, J. B. Cook, H. Lin, J. S. Ko, S. H. Tolbert, V. Ozolins and B. Dunn, *Nat. Mater.*, 2017, **16**, 454–460.
163 G. Wang, S. Oswald, M. Loffler, K. Mullen and X. Feng, *Adv. Mater.*, 2019, **31**, e1807712.
164 D. Zhu, L. Zhang, Y. Huang, J. Li, H. Fan and H. Wang, *ACS Appl. Energy Mater.*, 2019, **2**, 8031–8038.
165 S. Rothermel, P. Meister, G. Schmuelling, O. Fromm, H.-W. Meyer, S. Nowak, M. Winter and T. Placke, *Energy Environ. Sci.*, 2014, **7**, 3412–3423.
166 T. Placke, G. Schmuelling, R. Kloepsch, P. Meister, O. Fromm, P. Hilbig, H.-W. Meyer and M. Winter, *Z. Anorg. Allg. Chem.*, 2014, **640**, 1996–2006.
167 K. V. Kravchyk, P. Bhauriyal, L. Piveteau, C. P. Guntlin, B. Pathak and M. V. Kovalenko, *Nat. Commun.*, 2018, **9**, 4469.

168 C.-J. Pan, C. Yuan, G. Zhu, Q. Zhang, C.-J. Huang, M.-C. Lin, M. Angell, B.-J. Hwang, P. Kaghazchi and H. Dai, *Proc. Natl. Acad. Sci. U. S. A.*, 2018, **115**, 5670–5675.
169 H. Chen, H. Xu, S. Wang, T. Huang, J. Xi, S. Cai, F. Guo, Z. Xu, W. Gao and C. Gao, *Sci. Rep.*, 2017, **3**, 7233.
170 M.-C. Lin, M. Gong, B. Lu, Y. Wu, D.-Y. Wang, M. Guan, M. Angell, C. Chen, J. Yang, B.-J. Hwang and H. Dai, *Nature*, 2015, **520**, 324–328.
171 G. A. Elia, I. Hasa, G. Greco, T. Diemant, K. Marquardt, K. Hoeppner, R. J. Behm, A. Hoell, S. Passerini and R. Hahn, *J. Mater. Chem. A*, 2017, **5**, 9682–9690.
172 C. Yang, J. Chen, X. Ji, T. P. Pollard, X. Lü, C.-J. Sun, S. Hou, Q. Liu, C. Liu, T. Qing, Y. Wang, O. Borodin, Y. Ren, K. Xu and C. Wang, *Nature*, 2019, **569**, 245–250.
173 T. Placke, A. Heckmann, R. Schmuch, P. Meister, K. Beltrop and M. Winter, *Joule*, 2018, **2**, 2528–2550.
174 B. Ozmen Monkul, Dissertation, Oregon State University, 2010.
175 G. Schmuelling, T. Placke, R. Kloepsch, O. Fromm, H.-W. Meyer, S. Passerini and M. Winter, *J. Power Sources*, 2013, **239**, 563–571.
176 G. Furdin, B. Bach and A. Herold, *C. R. Acad. Sci. Paris C*, 1970, **271**, 683.
177 J. Zheng, M. H. Engelhard, D. Mei, S. Jiao, B. J. Polzin, J.-G. Zhang and W. Xu, *Nat. Energy*, 2017, **2**, 17012.
178 H.-J. Liao, Y.-M. Chen, Y.-T. Kao, J.-Y. An, Y.-H. Lai and D.-Y. Wang, *J. Phys. Chem. C*, 2017, **121**, 24463–24469.
179 T. Placke, O. Fromm, S. F. Lux, P. Bieker, S. Rothermel, H.-W. Meyer, S. Passerini and M. Winter, *J. Electrochem. Soc.*, 2012, **159**, A1755–A1765.
180 T. Placke, S. Rothermel, O. Fromm, P. Meister, S. F. Lux, J. Huesker, H.-W. Meyer and M. Winter, *J. Electrochem. Soc.*, 2013, **160**, A1979–A1991.
181 P. Meister, V. Siozios, J. Reiter, S. Klamor, S. Rothermel, O. Fromm, H.-W. Meyer, M. Winter and T. Placke, *Electrochim. Acta*, 2014, **130**, 625–633.
182 O. Fromm, P. Meister, X. Qi, S. Rothermel, J. Huesker, H. W. Meyer, M. Winter and T. Placke, *ECS Trans.*, 2014, **58**, 55–65.
183 K. Beltrop, P. Meister, S. Klein, A. Heckmann, M. Grünebaum, H.-D. Wiemhöfer, M. Winter and T. Placke, *Electrochim. Acta*, 2016, **209**, 44–55.
184 X. Wang, E. Yasukawa and S. Mori, *Electrochim. Acta*, 2000, **45**, 2677–2684.
185 L. PÉTer and J. Arai, *J. Appl. Electrochem.*, 1999, **29**, 1053–1061.
186 P. W. Ruch, M. Hahn, F. Rosciano, M. Holzapfel, H. Kaiser, W. Scheifele, B. Schmitt, P. Novák, R. Kötz and A. Wokaun, *Electrochim. Acta*, 2007, **53**, 1074–1082.
187 Y. Huang, H. Fan, H. Kamezaki, B. Kang, M. Yoshio and H. Wang, *ChemElectroChem*, 2019, **6**, 2931–2936.
188 L. Zhang, J. Li, Y. Huang, D. Zhu and H. Wang, *Langmuir*, 2019, **35**, 3972–3979.
189 D.-Y. Wang, C.-Y. Wei, M.-C. Lin, C.-J. Pan, H.-L. Chou, H.-A. Chen, M. Gong, Y. Wu, C. Yuan, M. Angell, Y.-J. Hsieh, Y.-H. Chen, C.-Y. Wen, C.-W. Chen, B.-J. Hwang, C.-C. Chen and H. Dai, *Nat. Commun.*, 2017, **8**, 14283.
190 M. Angell, C.-J. Pan, Y. Rong, C. Yuan, M.-C. Lin, B.-J. Hwang and H. Dai, *Proc. Natl. Acad. Sci. U. S. A.*, 2017, **114**, 834–839.
191 C.-Y. Chen, T. Tsuda, S. Kuwabata and C. L. Hussey, *Chem. Commun.*, 2018, **54**, 4164–4167.
192 K. Xu, *Chem. Rev.*, 2014, **114**, 11503–11618.
193 Z. Li, Y. Chen, Z. Jian, H. Jiang, J. J. Razink, W. F. Stickle, J. C. Neuefeind and X. Ji, *Chem. Mater.*, 2018, **30**, 4536–4542.
194 O. Borodin, X. Ren, J. Vatamanu, A. von Wald Cresce, J. Knap and K. Xu, *Acc. Chem. Res.*, 2017, **50**, 2886–2894.
195 S. Y. Hong, Y. Kim, Y. Park, A. Choi, N.-S. Choi and K. T. Lee, *Energy Environ. Sci.*, 2013, **6**, 2067–2081.
196 H. Wang and M. Yoshio, *Chem. Commun.*, 2010, **46**, 1544–1546.
197 M. Sheng, F. Zhang, B. Ji, X. Tong and Y. Tang, *Adv. Energy Mater.*, 2017, **7**, 1601963.
198 H. Zhu, F. Zhang, J. Li and Y. Tang, *Small*, 2018, **14**, e1703951.
199 S. Chen, J. Wang, L. Fan, R. Ma, E. Zhang, Q. Liu and B. Lu, *Adv. Energy Mater.*, 2018, **8**, 1800140.
200 B. Ji, F. Zhang, N. Wu and Y. Tang, *Adv. Energy Mater.*, 2017, **7**, 1700920.
201 B. Ji, F. Zhang, X. Song and Y. Tang, *Adv. Mater.*, 2017, **29**, 1700519.
202 M. Wang, C. Jiang, S. Zhang, X. Song, Y. Tang and H. M. Cheng, *Nat. Chem.*, 2018, **10**, 667–672.
203 M. Chen, W. Wang, X. Liang, S. Gong, J. Liu, Q. Wang, S. Guo and H. Yang, *Adv. Energy Mater.*, 2018, **8**, 1602778.
204 X. Fan, L. Chen, O. Borodin, X. Ji, J. Chen, S. Hou, T. Deng, J. Zheng, C. Yang, S. C. Liou, K. Amine, K. Xu and C. Wang, *Nat. Nanotechnol.*, 2018, **13**, 715–722.
205 S. Aladinli, F. Bordet, K. Ahlbrecht, J. Tübke and M. Holzapfel, *Electrochim. Acta*, 2017, **231**, 468–478.
206 J. A. Read, A. V. Cresce, M. H. Ervin and K. Xu, *Energy Environ. Sci.*, 2014, **7**, 617–620.
207 M. Winter, B. Barnett and K. Xu, *Chem. Rev.*, 2018, **118**, 11433–11456.
208 C. Peng, L. Yang, Z. Zhang, K. Tachibana, Y. Yang and S. Zhao, *Electrochim. Acta*, 2008, **53**, 4764–4772.
209 J. Mun, T. Yim, C. Y. Choi, J. H. Ryu, Y. G. Kim and S. M. Oh, *Electrochem. Solid-State Lett.*, 2010, **13**, A109–A111.
210 E. Cho, J. Mun, O. B. Chae, O. M. Kwon, H.-T. Kim, J. H. Ryu, Y. G. Kim and S. M. Oh, *Electrochem. Commun.*, 2012, **22**, 1–3.
211 C. Y. Chan, P.-K. Lee, Z. Xu and D. Y. W. Yu, *Electrochim. Acta*, 2018, **263**, 34–39.
212 A. Heckmann, J. Thienenkamp, K. Beltrop, M. Winter, G. Brunklaus and T. Placke, *Electrochim. Acta*, 2018, **260**, 514–525.
213 H. Fan, L. Qi and H. Wang, *Solid State Ionics*, 2017, **300**, 169–174.
214 K. V. Kravchyk, S. Wang, L. Piveteau and M. V. Kovalenko, *Chem. Mater.*, 2017, **29**, 4484–4492.
215 Y. Yamada, C. H. Chiang, K. Sodeyama, J. Wang, Y. Tateyama and A. Yamada, *ChemElectroChem*, 2015, **2**, 1687–1694.

216 L. Suo, O. Borodin, T. Gao, M. Olguin, J. Ho, X. Fan, C. Luo, C. Wang and K. Xu, *Science*, 2015, **350**, 938–943.
217 Y. Yamada, J. Wang, S. Ko, E. Watanabe and A. Yamada, *Nat. Energy*, 2019, **4**, 269–280.
218 S. Miyoshi, T. Akbay, T. Kurihara, T. Fukuda, A. T. Staykov, S. Ida and T. Ishihara, *J. Phys. Chem. C*, 2016, **120**, 22887–22894.
219 S. M. Zhang, J. X. Zhang, S. J. Xu, X. J. Yuan and B. C. He, *Electrochim. Acta*, 2013, **88**, 287–293.
220 H. Zheng, J. Li, X. Song, G. Liu and V. S. Battaglia, *Electrochim. Acta*, 2012, **71**, 258–265.
221 G. Wang, M. Yu, J. Wang, D. Li, D. Tan, M. Loffler, X. Zhuang, K. Mullen and X. Feng, *Adv. Mater.*, 2018, **30**, e1800533.
222 V. Augustyn, J. Come, M. A. Lowe, J. W. Kim, P.-L. Taberna, S. H. Tolbert, H. D. Abruña, P. Simon and B. Dunn, *Nat. Mater.*, 2013, **12**, 518–522.
223 A. Heckmann, P. Meister, L. Y. Kuo, M. Winter, P. Kaghazchi and T. Placke, *Electrochim. Acta*, 2018, **284**, 669–680.
224 M. L. Agiorgousis, Y.-Y. Sun and S. Zhang, *ACS Energy Lett.*, 2017, **2**, 689–693.
225 K. Persson, V. A. Sethuraman, L. J. Hardwick, Y. Hinuma, Y. S. Meng, A. van der Ven, V. Srinivasan, R. Kostecki and G. Ceder, *J. Phys. Chem. Lett.*, 2010, **1**, 1176–1180.
226 Y. Gao, C. Zhu, Z. Chen and G. Lu, *J. Phys. Chem. C*, 2017, **121**, 7131–7138.
227 J. Maire and J. Mering, *Chem. Phys. Carbon*, 1970, **6**, 125–129.
228 T. Ishihara, M. Koga, H. Matsumoto and M. Yoshio, *Electrochem. Solid-State Lett.*, 2007, **10**, A74–A76.
229 A. Heckmann, O. Fromm, U. Rodehorst, P. Münster, M. Winter and T. Placke, *Carbon*, 2018, **131**, 201–212.
230 A. Ejigu, L. W. Le Fevre, K. Fujisawa, M. Terrones, A. J. Forsyth and R. A. W. Dryfe, *ACS Appl. Mater. Interfaces*, 2019, **11**, 23261–23270.
231 J. Ortiz-Medina, Z. Wang, R. Cruz-Silva, A. Morelos-Gomez, F. Wang, X. Yao, M. Terrones and M. Endo, *Adv. Mater.*, 2019, **31**, 1805717.
232 A. Shah, A. Zahid, H. Subhan, A. Munir, F. J. Iftikhar and M. Akbar, *Sustainable Energy Fuels*, 2018, **2**, 1398–1429.
233 F. Lai, G. Zhou, F. Li, Z. He, D. Yong, W. Bai, Y. Huang, W. W. Tjiu, Y.-E. Miao, B. Pan and T. Liu, *ACS Sustainable Chem. Eng.*, 2018, **6**, 3143–3153.
234 H. Chen, F. Guo, Y. Liu, T. Huang, B. Zheng, N. Ananth, Z. Xu, W. Gao and C. Gao, *Adv. Mater.*, 2017, **29**, 1605958.
235 A. Ejigu, K. Fujisawa, B. F. Spencer, B. Wang, M. Terrones, I. A. Kinloch and R. A. W. Dryfe, *Adv. Funct. Mater.*, 2018, **28**, 1804357.
236 S. J. An, J. Li, C. Daniel, D. Mohanty, S. Nagpure and D. L. Wood, *Carbon*, 2016, **105**, 52–76.
237 T. Placke, O. Fromm, S. Rothermel, G. Schmuelling, P. Meister, H.-W. Meyer, S. Passerini and M. Winter, *ECS Trans.*, 2013, **50**, 59–68.
238 C. Nowak, L. Froboese, M. Winter, T. Placke, W. Haselrieder and A. Kwade, *Energy Technol.*, 2019, **7**, 1900528.
239 K. Zaghib, G. Nadeau and K. Kinoshita, *J. Electrochem. Soc.*, 2000, **147**, 2110–2115.
240 L. Zhang, L. Chen, H. Luo, X. Zhou and Z. Liu, *Adv. Energy Mater.*, 2017, **7**, 1700034.
241 S. Yang, X. Feng, L. Wang, K. Tang, J. Maier and K. Mullen, *Angew. Chem., Int. Ed.*, 2010, **49**, 4795–4799.
242 S. Han, D. Wu, S. Li, F. Zhang and X. Feng, *Small*, 2013, **9**, 1173–1187.
243 S. Han, D. Wu, S. Li, F. Zhang and X. Feng, *Adv. Mater.*, 2014, **26**, 849–864.
244 F. Yao, D. T. Pham and Y. H. Lee, *ChemSusChem*, 2015, **8**, 2284–2311.
245 I. Lahiri, S. W. Oh, J. Y. Hwang, S. Cho, Y. K. Sun, R. Banerjee and W. Choi, *ACS Nano*, 2010, **4**, 3440–3446.
246 S. Yin, Y. Zhang, J. Kong, C. Zou, C. M. Li, X. Lu, J. Ma, F. Y. Boey and X. Chen, *ACS Nano*, 2011, **5**, 3831–3838.
247 X. Zhao, C. M. Hayner, M. C. Kung and H. H. Kung, *ACS Nano*, 2011, **5**, 8739–8749.
248 C. Tang, Q. Zhang, M. Q. Zhao, J. Q. Huang, X. B. Cheng, G. L. Tian, H. J. Peng and F. Wei, *Adv. Mater.*, 2014, **26**, 6100–6105.
249 S. Li, Y. Luo, W. Lv, W. Yu, S. Wu, P. Hou, Q. Yang, Q. Meng, C. Liu and H.-M. Cheng, *Adv. Energy Mater.*, 2011, **1**, 486–490.
250 C. Masarapu, V. Subramanian, H. Zhu and B. Wei, *Adv. Funct. Mater.*, 2009, **19**, 1008–1014.
251 Y. Fang, Y. Lv, R. Che, H. Wu, X. Zhang, D. Gu, G. Zheng and D. Zhao, *J. Am. Chem. Soc.*, 2013, **135**, 1524–1530.
252 L. G. Bulusheva, V. E. Arkhipov, E. O. Fedorovskaya, S. Zhang, A. G. Kurenya, M. A. Kanygin, I. P. Asanov, A. R. Tsygankova, X. Chen, H. Song and A. V. Okotrub, *J. Power Sources*, 2016, **311**, 42–48.
253 E. Yoo, J. Kim, E. Hosono, H. S. Zhou, T. Kudo and I. Honma, *Nano Lett.*, 2008, **8**, 2277–2282.
254 W. Lu, A. Goering, L. Qu and L. Dai, *Phys. Chem. Chem. Phys.*, 2012, **14**, 12099–12104.
255 Y. Huang, D. Wu, J. Jiang, Y. Mai, F. Zhang, H. Pan and X. Feng, *Nano Energy*, 2015, **12**, 287–295.
256 H. Sun, A. E. Del Rio Castillo, S. Monaco, A. Capasso, A. Ansaldo, M. Prato, D. A. Dinh, V. Pellegrini, B. Scrosati, L. Manna and F. Bonaccorso, *J. Mater. Chem. A*, 2016, **4**, 6886–6895.
257 J. Hassoun, F. Bonaccorso, M. Agostini, M. Angelucci, M. G. Betti, R. Cingolani, M. Gemmi, C. Mariani, S. Panero, V. Pellegrini and B. Scrosati, *Nano Lett.*, 2014, **14**, 4901–4906.
258 R. Tian, M. Breshears, D. V. Horvath and J. N. Coleman, *ACS Nano*, 2020, **14**, 3129–3140.
259 Y. Chen, X. Li, X. Zhou, H. Yao, H. Huang, Y.-W. Mai and L. Zhou, *Energy Environ. Sci.*, 2014, **7**, 2689–2696.
260 F. Xu, D. Wu, R. Fu and B. Wei, *Mater. Today*, 2017, **20**, 629–656.
261 B. Li, F. Dai, Q. Xiao, L. Yang, J. Shen, C. Zhang and M. Cai, *Adv. Energy Mater.*, 2016, **6**, 1600802.
262 J. Niu, R. Shao, M. Liu, J. Liang, Z. Zhang, M. Dou, Y. Huang and F. Wang, *Energy Storage Mater.*, 2018, **12**, 145–152.
263 B. Campbell, R. Ionescu, Z. Favors, C. S. Ozkan and M. Ozkan, *Sci. Rep.*, 2015, **5**, 14575.

264 H. Tao, L. Xiong, S. Du, Y. Zhang, X. Yang and L. Zhang, *Carbon*, 2017, **122**, 54–63.
265 X. Liu, D. Chao, Y. Li, J. Hao, X. Liu, J. Zhao, J. Lin, H. J. Fan and Z. X. Shen, *Nano Energy*, 2015, **17**, 43–51.
266 Y. Yang, S. Jin, Z. Zhang, Z. Du, H. Liu, J. Yang, H. Xu and H. Ji, *ACS Appl. Mater. Interfaces*, 2017, **9**, 14180–14186.
267 W. Guo, X. Li, J. Xu, H. K. Liu, J. Ma and S. X. Dou, *Electrochim. Acta*, 2016, **188**, 414–420.
268 S. Zhang, F. Yao, L. Yang, F. Zhang and S. Xu, *Carbon*, 2015, **93**, 143–150.
269 W. Li, M. Li, M. Wang, L. Zeng and Y. Yu, *Nano Energy*, 2015, **13**, 693–701.
270 C. Kim, K. S. Yang, M. Kojima, K. Yoshida, Y. J. Kim, Y. A. Kim and M. Endo, *Adv. Funct. Mater.*, 2006, **16**, 2393–2397.
271 C. Kim, Y. I. Jeong, B. T. Ngoc, K. S. Yang, M. Kojima, Y. A. Kim, M. Endo and J. W. Lee, *Small*, 2007, **3**, 91–95.
272 L. Ji and X. Zhang, *Nanotechnology*, 2009, **20**, 155705.
273 W. Shi, Y. Zhang, Z. Q. Tian, Z. Pan, J. Key and P. K. Shen, *J. Power Sources*, 2018, **398**, 149–158.
274 Y. Xing, Y. Wang, C. Zhou, S. Zhang and B. Fang, *ACS Appl. Mater. Interfaces*, 2014, **6**, 2561–2567.
275 S. Yang, X. Feng, L. Zhi, Q. Cao, J. Maier and K. Mullen, *Adv. Mater.*, 2010, **22**, 838–842.
276 L. Ji and X. Zhang, *Electrochem. Commun.*, 2009, **11**, 684–687.
277 C. Kim, B. T. N. Ngoc, K. S. Yang, M. Kojima, Y. A. Kim, Y. J. Kim, M. Endo and S. C. Yang, *Adv. Mater.*, 2007, **19**, 2341–2346.
278 K. Huo, W. An, J. Fu, B. Gao, L. Wang, X. Peng, G. J. Cheng and P. K. Chu, *J. Power Sources*, 2016, **324**, 233–238.
279 L. Ji, Z. Lin, A. J. Medford and X. Zhang, *Carbon*, 2009, **47**, 3346–3354.
280 Z. Lyu, L. Yang, D. Xu, J. Zhao, H. Lai, Y. Jiang, Q. Wu, Y. Li, X. Wang and Z. Hu, *Nano Res.*, 2015, **8**, 3535–3543.
281 C. Ma, X. Shao and D. Cao, *J. Mater. Chem.*, 2012, 22.
282 D. Cai, S. Wang, P. Lian, X. Zhu, D. Li, W. Yang and H. Wang, *Electrochim. Acta*, 2013, **90**, 492–497.
283 T. Hu, X. Sun, H. Sun, G. Xin, D. Shao, C. Liu and J. Lian, *Phys. Chem. Chem. Phys.*, 2014, **16**, 1060–1066.
284 Z. J. Jiang and Z. Jiang, *ACS Appl. Mater. Interfaces*, 2014, **6**, 19082–19091.
285 Y. Liu, X. Wang, Y. Dong, Z. Wang, Z. Zhao and J. Qiu, *J. Mater. Chem. A*, 2014, **2**, 16832–16835.
286 L. G. Bulusheva, A. V. Okotrub, A. G. Kurenya, H. Zhang, H. Zhang, X. Chen and H. Song, *Carbon*, 2011, **49**, 4013–4023.
287 B. Zhang, Y. Yu, Z.-L. Xu, S. Abouali, M. Akbari, Y.-B. He, F. Kang and J.-K. Kim, *Adv. Energy Mater.*, 2014, **4**, 1301448.
288 Z. Wang, X. Xiong, L. Qie and Y. Huang, *Electrochim. Acta*, 2013, **106**, 320–326.
289 L. Qie, W. M. Chen, Z. H. Wang, Q. G. Shao, X. Li, L. X. Yuan, X. L. Hu, W. X. Zhang and Y. H. Huang, *Adv. Mater.*, 2012, **24**, 2047–2050.
290 X. Li, X. Zhu, Y. Zhu, Z. Yuan, L. Si and Y. Qian, *Carbon*, 2014, **69**, 515–524.
291 Y. Yang, F. Zheng, G. Xia, Z. Lun and Q. Chen, *J. Mater. Chem. A*, 2015, **3**, 18657–18666.
292 C. Zhang, N. Mahmood, H. Yin, F. Liu and Y. Hou, *Adv. Mater.*, 2013, **25**, 4932–4937.
293 X. Ma, G. Ning, C. Qi, C. Xu and J. Gao, *ACS Appl. Mater. Interfaces*, 2014, **6**, 14415–14422.
294 X. Ma, G. Ning, Y. Sun, Y. Pu and J. Gao, *Carbon*, 2014, **79**, 310–320.
295 Z. Qiu, Y. Lin, H. Xin, P. Han, D. Li, B. Yang, P. Li, S. Ullah, H. Fan, C. Zhu and J. Xu, *Carbon*, 2018, **126**, 85–92.
296 J. Ruan, T. Yuan, Y. Pang, S. Luo, C. Peng, J. Yang and S. Zheng, *Carbon*, 2018, **126**, 9–16.
297 J. T. Wang, H. Weng, S. Nie, Z. Fang, Y. Kawazoe and C. Chen, *Phys. Rev. Lett.*, 2016, **116**, 195501.
298 J. Liu, S. Wang and Q. Sun, *Proc. Natl. Acad. Sci. U. S. A.*, 2017, **114**, 651–656.
299 S. Wang, B. Yang, H. Chen and E. Ruckenstein, *J. Mater. Chem. A*, 2018, **6**, 6815–6821.
300 L. David and G. Singh, *J. Phys. Chem. C*, 2014, **118**, 28401–28408.
301 X.-F. Luo, C.-H. Yang and J.-K. Chang, *J. Mater. Chem. A*, 2015, **3**, 17282–17289.
302 J. C. Pramudita, D. Pontiroli, G. Magnani, M. Gaboardi, M. Riccò, C. Milanese, H. E. A. Brand and N. Sharma, *ChemElectroChem*, 2015, **2**, 600–610.
303 J. Wan, F. Shen, W. Luo, L. Zhou, J. Dai, X. Han, W. Bao, Y. Xu, J. Panagiotopoulos, X. Fan, D. Urban, A. Nie, R. Shahbazian-Yassar and L. Hu, *Chem. Mater.*, 2016, **28**, 6528–6535.
304 Y. S. Yun, Y.-U. Park, S.-J. Chang, B. H. Kim, J. Choi, J. Wang, D. Zhang, P. V. Braun, H.-J. Jin and K. Kang, *Carbon*, 2016, **99**, 658–664.
305 J. Xu, M. Wang, N. P. Wickramaratne, M. Jaroniec, S. Dou and L. Dai, *Adv. Mater.*, 2015, **27**, 2042–2048.
306 J. Ding, H. Wang, Z. Li, A. Kohandehghan, K. Cui, Z. Xu, B. Zahiri, X. Tan, E. M. Lotfabad, B. C. Olsen and D. Mitlin, *ACS Nano*, 2013, **7**, 11004–11015.
307 E. M. Lotfabad, J. Ding, K. Cui, A. Kohandehghan, W. P. Kalisvaart, M. Hazelton and D. Mitlin, *ACS Nano*, 2014, **8**, 7115–7129.
308 W. Lv, F. Wen, J. Xiang, J. Zhao, L. Li, L. Wang, Z. Liu and Y. Tian, *Electrochim. Acta*, 2015, **176**, 533–541.
309 R. R. Gaddam, D. Yang, R. Narayan, K. Raju, N. A. Kumar and X. S. Zhao, *Nano Energy*, 2016, **26**, 346–352.
310 Y. Li, Y.-S. Hu, M.-M. Titirici, L. Chen and X. Huang, *Adv. Energy Mater.*, 2016, **6**, 1600659.
311 V. Selvamani, R. Ravikumar, V. Suryanarayanan, D. Velayutham and S. Gopukumar, *Electrochim. Acta*, 2016, **190**, 337–345.
312 F. Shen, W. Luo, J. Dai, Y. Yao, M. Zhu, E. Hitz, Y. Tang, Y. Chen, V. L. Sprenkle, X. Li and L. Hu, *Adv. Energy Mater.*, 2016, **6**, 1600377.
313 L. Wu, D. Buchholz, C. Vaalma, G. A. Giffin and S. Passerini, *ChemElectroChem*, 2016, **3**, 292–298.
314 D. Xu, C. Chen, J. Xie, B. Zhang, L. Miao, J. Cai, Y. Huang and L. Zhang, *Adv. Energy Mater.*, 2016, **6**, 1501929.

315 S. Qiu, L. Xiao, M. L. Sushko, K. S. Han, Y. Shao, M. Yan, X. Liang, L. Mai, J. Feng, Y. Cao, X. Ai, H. Yang and J. Liu, *Adv. Energy Mater.*, 2017, **7**, 1700403.
316 T. Yang, T. Qian, M. Wang, X. Shen, N. Xu, Z. Sun and C. Yan, *Adv. Mater.*, 2016, **28**, 539–545.
317 P. Zheng, T. Liu, X. Yuan, L. Zhang, Y. Liu, J. Huang and S. Guo, *Sci. Rep.*, 2016, **6**, 26246.
318 M. Dahbi, M. Kiso, K. Kubota, T. Horiba, T. Chafik, K. Hida, T. Matsuyama and S. Komaba, *J. Mater. Chem. A*, 2017, **5**, 9917–9928.
319 K. Kim, D. G. Lim, C. W. Han, S. Osswald, V. Ortalan, J. P. Youngblood and V. G. Pol, *ACS Sustainable Chem. Eng.*, 2017, **5**, 8720–8728.
320 H. Liu, M. Jia, S. Yue, B. Cao, Q. Zhu, N. Sun and B. Xu, *J. Mater. Chem. A*, 2017, **5**, 9572–9579.
321 K. Wang, Y. Jin, S. Sun, Y. Huang, J. Peng, J. Luo, Q. Zhang, Y. Qiu, C. Fang and J. Han, *ACS Omega*, 2017, **2**, 1687–1695.
322 S. Huang, Z. Li, B. Wang, J. Zhang, Z. Peng, R. Qi, J. Wang and Y. Zhao, *Adv. Funct. Mater.*, 2018, **28**, 1706294.
323 Y. Zheng, Y. Wang, Y. Lu, Y.-S. Hu and J. Li, *Nano Energy*, 2017, **39**, 489–498.
324 M. Yu, D. Lin, H. Feng, Y. Zeng, Y. Tong and X. Lu, *Angew. Chem., Int. Ed.*, 2017, **56**, 5454–5459.
325 Y. Bai, Z. Wang, C. Wu, R. Xu, F. Wu, Y. Liu, H. Li, Y. Li, J. Lu and K. Amine, *ACS Appl. Mater. Interfaces*, 2015, **7**, 5598–5604.
326 H. Liu, M. Jia, B. Cao, R. Chen, X. Lv, R. Tang, F. Wu and B. Xu, *J. Power Sources*, 2016, **319**, 195–201.
327 L. Xiao, Y. Cao, W. A. Henderson, M. L. Sushko, Y. Shao, J. Xiao, W. Wang, M. H. Engelhard, Z. Nie and J. Liu, *Nano Energy*, 2016, **19**, 279–288.
328 F. Xu, Y. Qiu, H. Han, G. Jiang, R. Zhao, E. Zhang, H. Li, H. Wang and S. Kaskel, *Carbon*, 2020, **159**, 140–148.
329 S. Wang, L. Xia, L. Yu, L. Zhang, H. Wang and X. W. D. Lou, *Adv. Energy Mater.*, 2016, **6**, 1502217.
330 B. Zhang, C. M. Ghimbeu, C. Laberty, C. Vix-Guterl and J.-M. Tarascon, *Adv. Energy Mater.*, 2016, **6**, 1501588.
331 Y. Chen, X. Li, K. Park, W. Lu, C. Wang, W. Xue, F. Yang, J. Zhou, L. Suo, T. Lin, H. Huang, J. Li and J. B. Goodenough, *Chem*, 2017, **3**, 152–163.
332 B. Yang, J. Chen, S. Lei, R. Guo, H. Li, S. Shi and X. Yan, *Adv. Energy Mater.*, 2018, **8**, 1702409.
333 H. Hou, C. E. Banks, M. Jing, Y. Zhang and X. Ji, *Adv. Mater.*, 2015, **27**, 7861–7866.
334 W. Luo, Z. Jian, Z. Xing, W. Wang, C. Bommier, M. M. Lerner and X. Ji, *ACS Cent. Sci.*, 2015, **1**, 516–522.
335 J. Ding, Z. Li, K. Cui, S. Boyer, D. Karpuzov and D. Mitlin, *Nano Energy*, 2016, **23**, 129–137.
336 Y. Li, Z. Wang, L. Li, S. Peng, L. Zhang, M. Srinivasan and S. Ramakrishna, *Carbon*, 2016, **99**, 556–563.
337 Z. Luo, J. Zhou, X. Cao, S. Liu, Y. Cai, L. Wang, A. Pan and S. Liang, *Carbon*, 2017, **122**, 82–91.
338 M. Wang, Y. Yang, Z. Yang, L. Gu, Q. Chen and Y. Yu, *Adv. Sci.*, 2017, **4**, 1600468.
339 Z. Li, C. Bommier, Z. S. Chong, Z. Jian, T. W. Surta, X. Wang, Z. Xing, J. C. Neuefeind, W. F. Stickle, M. Dolgos, P. A. Greaney and X. Ji, *Adv. Energy Mater.*, 2017, **7**, 1602894.
340 L. Qie, W. Chen, X. Xiong, C. Hu, F. Zou, P. Hu and Y. Huang, *Adv. Sci.*, 2015, **2**, 1500195.
341 H. Yamamoto, S. Muratsubaki, K. Kubota, M. Fukunishi, H. Watanabe, J. Kim and S. Komaba, *J. Mater. Chem. A*, 2018, **6**, 16844–16848.
342 J. Zhao, X. Zou, Y. Zhu, Y. Xu and C. Wang, *Adv. Funct. Mater.*, 2016, **26**, 8103–8110.
343 A. P. Cohn, N. Muralidharan, R. Carter, K. Share, L. Oakes and C. L. Pint, *J. Mater. Chem. A*, 2016, **4**, 14954–14959.
344 Y. Wang, Z. Wang, Y. Chen, H. Zhang, M. Yousaf, H. Wu, M. Zou, A. Cao and R. P. S. Han, *Adv. Mater.*, 2018, **30**, e1802074.
345 B. Cao, Q. Zhang, H. Liu, B. Xu, S. Zhang, T. Zhou, J. Mao, W. K. Pang, Z. Guo, A. Li, J. Zhou, X. Chen and H. Song, *Adv. Energy Mater.*, 2018, **8**, 1801149.
346 J. Li, W. Qin, J. Xie, H. Lei, Y. Zhu, W. Huang, X. Xu, Z. Zhao and W. Mai, *Nano Energy*, 2018, **53**, 415–424.
347 X. Zhao, Y. Tang, C. Ni, J. Wang, A. Star and Y. Xu, *ACS Appl. Energy Interfaces*, 2018, **1**, 1703–1707.
348 S. Zeng, X. Zhou, B. Wang, Y. Feng, R. Xu, H. Zhang, S. Peng and Y. Yu, *J. Mater. Chem. A*, 2019, **7**, 15774–15781.
349 H. Li, Z. Cheng, Q. Zhang, A. Natan, Y. Yang, D. Cao and H. Zhu, *Nano Lett.*, 2018, **18**, 7407–7413.
350 M. Yu, Z. Wang, H. Zhang, P. Zhang, T. Zhang, X. Lu and X. Feng, *Nano Energy*, 2019, **65**, 103987.
351 C. Chen, Z. Wang, B. Zhang, L. Miao, J. Cai, L. Peng, Y. Huang, J. Jiang, Y. Huang, L. Zhang and J. Xie, *Energy Storage Mater.*, 2017, **8**, 161–168.
352 W. Cao, E. Zhang, J. Wang, Z. Liu, J. Ge, X. Yu, H. Yang and B. Lu, *Electrochim. Acta*, 2019, **293**, 364–370.
353 C. Chen, M. Wu, Y. Wang and K. Zaghib, *J. Power Sources*, 2019, **444**, 227310.
354 C. Gao, Q. Wang, S. Luo, Z. Wang, Y. Zhang, Y. Liu, A. Hao and R. Guo, *J. Power Sources*, 2019, **415**, 165–171.
355 Z. Zhang, B. Jia, L. Liu, Y. Zhao, H. Wu, M. Qin, K. Han, W. A. Wang, K. Xi, L. Zhang, G. Qi, X. Qu and R. V. Kumar, *ACS Nano*, 2019, **13**, 11363–11371.
356 D. S. Bin, X. J. Lin, Y. G. Sun, Y. S. Xu, K. Zhang, A. M. Cao and L. J. Wan, *J. Am. Chem. Soc.*, 2018, **140**, 7127–7134.
357 R. A. Adams, J. M. Syu, Y. Zhao, C. T. Lo, A. Varma and V. G. Pol, *ACS Appl. Mater. Interfaces*, 2017, **9**, 17872–17881.
358 W. Yang, J. Zhou, S. Wang, W. Zhang, Z. Wang, F. Lv, K. Wang, Q. Sun and S. Guo, *Energy Environ. Sci.*, 2019, **12**, 1605–1612.
359 Z. Jian, Z. Xing, C. Bommier, Z. Li and X. Ji, *Adv. Energy Mater.*, 2016, **6**, 1501874.
360 Y. Xu, C. Zhang, M. Zhou, Q. Fu, C. Zhao, M. Wu and Y. Lei, *Nat. Commun.*, 2018, **9**, 1720.
361 X. Qi, K. Huang, X. Wu, W. Zhao, H. Wang, Q. Zhuang and Z. Ju, *Carbon*, 2018, **131**, 79–85.
362 W. Zhang, X. Jiang, X. Wang, Y. V. Kaneti, Y. Chen, J. Liu, J. S. Jiang, Y. Yamauchi and M. Hu, *Angew. Chem., Int. Ed.*, 2017, **56**, 8435–8440.
363 P. Xiong, X. Zhao and Y. Xu, *ChemSusChem*, 2018, **11**, 202–208.
364 D. Li, X. Cheng, R. Xu, Y. Wu, X. Zhou, C. Ma and Y. Yu, *J. Mater. Chem. A*, 2019, **7**, 19929–19938.

365 X. Chang, X. Zhou, X. Ou, C. S. Lee, J. Zhou and Y. Tang, *Adv. Energy Mater.*, 2019, **9**, 1902672.
366 D. Li, X. Ren, Q. Ai, Q. Sun, L. Zhu, Y. Liu, Z. Liang, R. Peng, P. Si, J. Lou, J. Feng and L. Ci, *Adv. Energy Mater.*, 2018, **8**, 1802386.
367 G. Wang, X. Xiong, D. Xie, Z. Lin, J. Zheng, F. Zheng, Y. Li, Y. Liu, C. Yang and M. Liu, *J. Mater. Chem. A*, 2018, **6**, 24317–24323.
368 J. Yang, Z. Ju, Y. Jiang, Z. Xing, B. Xi, J. Feng and S. Xiong, *Adv. Mater.*, 2018, **30**, 1700104.
369 P. Li, J.-Y. Hwang and Y.-K. Sun, *J. Mater. Chem. A*, 2019, **7**, 20675–20682.
370 L. Liu, Y. Chen, Y. Xie, P. Tao, Q. Li and C. Yan, *Adv. Funct. Mater.*, 2018, 28.
371 Y. Liu, H. Dai, L. Wu, W. Zhou, L. He, W. Wang, W. Yan, Q. Huang, L. Fu and Y. Wu, *Adv. Energy Mater.*, 2019, **9**, 1901379.
372 M. Noel and R. Santhanam, *J. Power Sources*, 1998, **72**, 53–65.
373 R. Santhanam and M. Noel, *J. Power Sources*, 1998, **76**, 147–152.
374 J. R. Dahn and J. A. Seel, *J. Electrochem. Soc.*, 2000, **147**, 899–901.
375 S. Rothermel, P. Meister, O. Fromm, J. Huesker, H. W. Meyer, M. Winter and T. Placke, *ECS Trans.*, 2014, **58**, 15–25.
376 G. Wang, F. Wang, P. Zhang, J. Zhang, T. Zhang, K. Mullen and X. Feng, *Adv. Mater.*, 2018, **30**, e1802949.
377 S. Miyoshi, H. Nagano, T. Fukuda, T. Kurihara, M. Watanabe, S. Ida and T. Ishihara, *J. Electrochem. Soc.*, 2016, **163**, A1206–A1213.
378 P. Han, X. Han, J. Yao, L. Yue, J. Zhao, X. Zhou and G. Cui, *J. Power Sources*, 2018, **393**, 145–151.
379 L. Zhang, S. X. Dou, H. K. Liu, Y. Huang and X. Hu, *Adv. Sci.*, 2016, **3**, 1600115.
380 T. Placke, P. Bieker, S. F. Lux, O. Fromm, H.-W. Meyer, S. Passerini and M. Winter, *Z. Phys. Chem.*, 2012, **226**, 391–407.
381 A. K. Thapa, G. Park, H. Nakamura, T. Ishihara, N. Moriyama, T. Kawamura, H. Wang and M. Yoshio, *Electrochim. Acta*, 2010, **55**, 7305–7309.
382 N. Gunawardhana, G.-J. Park, N. Dimov, A. K. Thapa, H. Nakamura, H. Wang, T. Ishihara and M. Yoshio, *J. Power Sources*, 2011, **196**, 7886–7890.
383 X. Zhang, Y. Tang, F. Zhang and C.-S. Lee, *Adv. Energy Mater.*, 2016, **6**, 1502588.
384 S. Li, J. Niu, Y. C. Zhao, K. P. So, C. Wang, C. A. Wang and J. Li, *Nat. Commun.*, 2015, **6**, 7872.
385 E. C. Gay, D. R. Vissers, F. J. Martino and K. E. Anderson, *J. Electrochem. Soc.*, 1976, **123**, 1591–1596.
386 C. J. Wen, B. A. Boukamp, R. A. Huggins and W. Weppner, *J. Electrochem. Soc.*, 1979, **126**, 2258–2266.
387 M. N. Obrovac and L. Christensen, *Electrochem. Solid-State Lett.*, 2004, **7**, A93–A96.
388 X. Tong, F. Zhang, B. Ji, M. Sheng and Y. Tang, *Adv. Mater.*, 2016, **28**, 9979–9985.
389 P. Qin, M. Wang, N. Li, H. Zhu, X. Ding and Y. Tang, *Adv. Mater.*, 2017, **29**, 1606805.
390 C. Jiang, Y. Fang, J. Lang and Y. Tang, *Adv. Energy Mater.*, 2017, **7**, 1700913.
391 S. Zhang, M. Wang, Z. Zhou and Y. Tang, *Adv. Funct. Mater.*, 2017, **27**, 1703035.
392 X. Tong, F. Zhang, G. Chen, X. Liu, L. Gu and Y. Tang, *Adv. Energy Mater.*, 2018, **8**, 1701967.
393 S. Wang, X. Xiao, Y. Zhou, C. Fu and S. Jiao, *Electrochim. Acta*, 2018, **282**, 946–954.
394 S. Bellani, F. Wang, G. Longoni, L. Najafi, R. Oropesa-Nuñez, A. E. Del Rio Castillo, M. Prato, X. Zhuang, V. Pellegrini, X. Feng and F. Bonaccorso, *Nano Lett.*, 2018, **18**, 7155–7164.
395 S.-M. Hao, J. Qu, W. Chang, Y.-J. Zhang, Y. Tang and Z.-Z. Yu, *ChemElectroChem*, 2019, **6**, 1040–1046.
396 H. Wang and M. Yoshio, *Electrochem. Commun.*, 2008, **10**, 382–386.
397 X. Y. Jiang, X. W. Liu, Z. Q. Zeng, L. F. Xiao, X. P. Ai, H. X. Yang and Y. L. Cao, *Adv. Energy Mater.*, 2018, **8**, 1802176.
398 M. Wakihara, *Mater. Sci. Eng., R*, 2001, **33**, 109–134.
399 L. Fan, Q. Liu, S. H. Chen, Z. Xu and B. G. Lu, *Adv. Energy Mater.*, 2017, **7**, 1602778.
400 X. Wang, C. Zheng, L. Qi and H. Wang, *Global Challenges*, 2017, **1**, 1700055.
401 Z. Hu, Q. Liu, K. Zhang, L. Zhou, L. Li, M. Chen, Z. Tao, Y.-M. Kang, L. Mai, S.-L. Chou, J. Chen and S.-X. Dou, *ACS Appl. Mater. Interfaces*, 2018, **10**, 35978–35983.
402 F. Wang, Z. Liu, P. Zhang, H. Li, W. Sheng, T. Zhang, R. Jordan, Y. Wu, X. Zhuang and X. Feng, *Small*, 2017, **13**, 1702449.
403 L. Zhao, L. Qi and H. Wang, *J. Power Sources*, 2013, **242**, 597–603.
404 C. Li, X. Wang, J. Li and H. Wang, *Chem. Commun.*, 2018, **54**, 4349–4352.
405 J. Fan, Y. Fang, Q. Xiao, R. Huang, L. Li and W. Yuan, *Energy Technol.*, 2019, **7**, 1800978.
406 L. D. Ellis, T. D. Hatchard and M. N. Obrovac, *J. Electrochem. Soc.*, 2012, **159**, A1801–A1805.
407 C. Jiang, Y. Fang, W. Zhang, X. Song, J. Lang, L. Shi and Y. Tang, *Angew. Chem., Int. Ed.*, 2018, **57**, 16370–16374.
408 C. Cui, Z. Wei, J. Xu, Y. Zhang, S. Liu, H. Liu, M. Mao, S. Wang, J. Ma and S. Dou, *Energy Storage Mater.*, 2018, **15**, 22–30.
409 K. Beltrop, S. Beuker, A. Heckmann, M. Winter and T. Placke, *Energy Environ. Sci.*, 2017, **10**, 2090–2094.
410 L. Fan, Q. Liu, S. Chen, K. Lin, Z. Xu and B. Lu, *Small*, 2017, **13**, 1701011.
411 J. Zhu, Y. Li, B. Yang, L. Liu, J. Li, X. Yan and D. He, *Small*, 2018, **14**, e1801836.
412 X. Ding, F. Zhang, B. Ji, Y. Liu, J. Li, C.-S. Lee and Y. Tang, *ACS Appl. Mater. Interfaces*, 2018, **10**, 42294–42300.
413 N. S. Hudak, *J. Phys. Chem. C*, 2014, **118**, 5203–5215.
414 N. Jayaprakash, S. K. Das and L. A. Archer, *Chem. Commun.*, 2011, **47**, 12610–12612.
415 P. R. Gifford and J. B. Palmisano, *J. Electrochem. Soc.*, 1988, **135**, 650–654.
416 H. Sun, W. Wang, Z. Yu, Y. Yuan, S. Wang and S. Jiao, *Chem. Commun.*, 2015, **51**, 11892–11895.

417 M. Han, Z. Lv, L. Hou, S. Zhou, H. Cao, H. Chen, Y. Zhou, C. Meng, H. Du, M. Cai, Y. Bian and M.-C. Lin, *J. Power Sources*, 2020, **451**, 227769.
418 H. Chen, C. Chen, Y. Liu, X. Zhao, N. Ananth, B. Zheng, L. Peng, T. Huang, W. Gao and C. Gao, *Adv. Energy Mater.*, 2017, **7**, 1700051.
419 X. Yu, B. Wang, D. Gong, Z. Xu and B. Lu, *Adv. Mater.*, 2017, **29**, 1604118.
420 C. Matei Ghimbeu, J. Górka, V. Simone, L. Simonin, S. Martinet and C. Vix-Guterl, *Nano Energy*, 2018, **44**, 327–335.
421 S. Jiao, H. Lei, J. Tu, J. Zhu, J. Wang and X. Mao, *Carbon*, 2016, **109**, 276–281.
422 H. Jiao, C. Wang, J. Tu, D. Tian and S. Jiao, *Chem. Commun.*, 2017, **53**, 2331–2334.
423 J. Li, J. Tu, H. Jiao, C. Wang and S. Jiao, *J. Electrochem. Soc.*, 2017, **164**, A3093–A3100.
424 H. Xu, T. Bai, H. Chen, F. Guo, J. Xi, T. Huang, S. Cai, X. Chu, J. Ling, W. Gao, Z. Xu and C. Gao, *Energy Storage Mater.*, 2019, **17**, 38–45.
425 Y. Song, S. Jiao, J. Tu, J. Wang, Y. Liu, H. Jiao, X. Mao, Z. Guo and D. J. Fray, *J. Mater. Chem. A*, 2017, **5**, 1282–1291.
426 J. Wang, X. Zhang, W. Chu, S. Liu and H. Yu, *Chem. Commun.*, 2019, **55**, 2138–2141.
427 R. J. Gummow, G. Vamvounis, M. B. Kannan and Y. He, *Adv. Mater.*, 2018, **30**, 1801702.
428 J. Lang, C. Jiang, Y. Fang, L. Shi, S. Miao and Y. Tang, *Adv. Energy Mater.*, 2019, **9**, 1901099.
429 G.-F. Wang, H. Qin, X. Gao, Y. Cao, W. Wang, F.-C. Wang, H.-A. Wu, H.-P. Cong and S.-H. Yu, *Chem*, 2018, **4**, 896–910.
430 J. Park, Z. L. Xu, G. Yoon, S. K. Park, J. Wang, H. Hyun, H. Park, J. Lim, Y. J. Ko, Y. S. Yun and K. Kang, *Adv. Mater.*, 2020, **32**, e1904411.
431 G. Wang, B. Kohn, U. Scheler, F. Wang, S. Oswald, M. Loffler, D. Tan, P. Zhang, J. Zhang and X. Feng, *Adv. Mater.*, 2020, **32**, e1905681.
432 F. Wang, O. Borodin, T. Gao, X. Fan, W. Sun, F. Han, A. Faraone, J. A. Dura, K. Xu and C. Wang, *Nat. Mater.*, 2018, **17**, 543–549.
433 D. Kundu, B. D. Adams, V. Duffort, S. H. Vajargah and L. F. Nazar, *Nat. Energy*, 2016, **1**, 16119.
434 H. Pan, Y. Shao, P. Yan, Y. Cheng, K. S. Han, Z. Nie, C. Wang, J. Yang, X. Li, P. Bhattacharya, K. T. Mueller and J. Liu, *Nat. Energy*, 2016, **1**, 16039.
435 J. F. Parker, C. N. Chervin, I. R. Pala, M. Machler, M. F. Burz, J. W. Long and D. R. Rolison, *Science*, 2017, **356**, 415–418.
436 J. Zheng, Q. Zhao, T. Tang, J. Yin, C. D. Quilty, G. D. Renderos, X. Liu, Y. Deng, L. Wang, D. C. Bock, C. Jaye, D. Zhang, E. S. Takeuchi, K. J. Takeuchi, A. C. Marschilok and L. A. Archer, *Science*, 2019, **366**, 645–648.
437 J. Fan, Q. Xiao, Y. Fang, L. Li and W. Yuan, *Ionics*, 2018, **25**, 1303–1313.
438 B. Ji, W. Yao and Y. Tang, *Sustainable Energy Fuels*, 2020, **4**, 101–107.
439 Z. Lv, M. Han, J. Sun, L. Hou, H. Chen, Y. Li and M.-C. Lin, *J. Power Sources*, 2019, **418**, 233–240.
440 R. T. Carlin, H. C. De Long, J. Fuller and P. C. Trulove, *J. Electrochem. Soc.*, 1994, **141**, L73–L76.
441 J. Fan, Z. Zhang, Y. Liu, A. Wang, L. Li and W. Yuan, *Chem. Commun.*, 2017, **53**, 6891–6894.
442 A. Wang, W. Yuan, J. Fan and L. Li, *Energy Technol.*, 2018, **6**, 2172–2178.
443 Y. Fang, C. Chen, J. Fan, M. Zhang, W. Yuan and L. Li, *Chem. Commun.*, 2019, **55**, 8333–8336.
444 H. Wang and M. Yoshio, *Electrochem. Commun.*, 2006, **8**, 1481–1486.
445 J. Gao, S. Tian, L. Qi and H. Wang, *Electrochim. Acta*, 2015, **176**, 22–27.
446 J. Gao, M. Yoshio, L. Qi and H. Wang, *J. Power Sources*, 2015, **278**, 452–457.
447 Y. Huang, L. Qi and H. Wang, *Electrochim. Acta*, 2017, **258**, 380–387.
448 X. Shi, W. Zhang, J. Wang, W. Zheng, K. Huang, H. Zhang, S. Feng and H. Chen, *Adv. Energy Mater.*, 2016, **6**, 1601378.
449 X. Li, J. Liu, F. Q. Wang, Q. Wang and P. Jena, *J. Phys. Chem. Lett.*, 2019, **10**, 6360–6367.
450 J. Hao, F. Yang, S. Zhang, H. He, G. Xia, Y. Liu, C. Didier, T. Liu, W. K. Pang, V. K. Peterson, J. Lu and Z. Guo, *Proc. Natl. Acad. Sci. U. S. A.*, 2020, **117**, 2815–2823.
451 S. Wang, K. V. Kravchyk, A. N. Filippin, U. Müller, A. N. Tiwari, S. Buecheler, M. I. Bodnarchuk and M. V. Kovalenko, *Adv. Sci.*, 2018, **5**, 1700712.